

AD-755 535

Test Results Report and Technology Development Report HLH/ATC Compliant Roller Bearing Development Program

Boeing Co.

prepared for

**Army Air Mobility Research and Development
Laboratory**

Army Aviation Systems Command

NOVEMBER 1972

Distributed By:

NTIS

**National Technical Information Service
U. S. DEPARTMENT OF COMMERCE**

AD

USAAMRDL TECHNICAL REPORT 72-62

TEST RESULTS REPORT AND TECHNOLOGY DEVELOPMENT REPORT HLH/ATC COMPLIANT ROLLER BEARING DEVELOPMENT PROGRAM

AD 755535

By

J. W. Lenski, Jr.

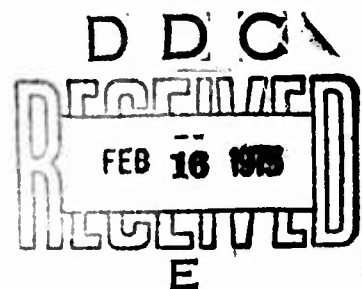
November 1972

**U. S. ARMY AVIATION SYSTEMS COMMAND
ST. LOUIS, MISSOURI**

**CONTRACT DAAJ01-71-C-0840 (P40)
THE BOEING COMPANY, VERTOL DIVISION
PHILADELPHIA, PENNSYLVANIA**

Approved for public release;
distribution unlimited.

Reproduced by
**NATIONAL TECHNICAL
INFORMATION SERVICE**
U S Department of Commerce
Springfield VA 22151



DISCLAIMERS

The findings in this report are not to be construed as an official Department of the Army position unless so designated by other authorized documents.

When Government drawings, specifications, or other data are used for any purpose other than in connection with a definitely related Government procurement operation, the United States Government thereby incurs no responsibility nor any obligation whatsoever; and the fact that the Government may have formulated, furnished, or in any way supplied the said drawings, specifications, or other data is not to be regarded by implication or otherwise as in any manner licensing the holder or any other person or corporation, or conveying any rights or permission, to manufacture, use, or sell any patented invention that may in any way be related thereto.

Trade names cited in this report do not constitute an official endorsement or approval of the use of such commercial hardware or software.

DISPOSITION INSTRUCTIONS

Destroy this report when no longer needed. Do not return it to the originator.

ADDITIONAL INFORMATION

NTIS _____
DPC _____
DTI _____

White Section ☒
Ext. Section ☐
☐

BY _____

TECH AVAILABILITY CODES

GENERAL AND SPECIAL

A

Unclassified

Security Classification

DOCUMENT CONTROL DATA - R & D

(Security classification of title, body of abstract and indexing annotation must be entered when the overall report is classified)

1. ORIGINATING ACTIVITY (Corporate author) The Boeing Company, Vertol Division P. O. Box 16858 - Boeing Center Philadelphia, Pennsylvania		2a. REPORT SECURITY CLASSIFICATION Unclassified	
		2b. GROUP	
3. REPORT TITLE TEST RESULTS REPORT AND TECHNOLOGY DEVELOPMENT REPORT HLH/ATC COMPLIANT ROLLER BEARING DEVELOPMENT PROGRAM			
4. DESCRIPTIVE NOTES (Type of report and inclusive dates) Final			
5. AUTHOR(S) (First name, middle initial, last name) Joseph W. Lenski, Jr.			
6. REPORT DATE November 1972		7a. TOTAL NO. OF PAGES 134	7b. NO. OF REFS 4
8a. CONTRACT OR GRANT NO. DAAJ01-71-C-0840 (P40)		8b. ORIGINATOR'S REPORT NUMBER(S) USAAMRDL Technical Report 72-62	
9. PROJECT NO. 1X16303D156		9b. OTHER REPORT NO(S) (Any other numbers that may be assigned this report)	
10. DISTRIBUTION STATEMENT Approved for public release; distribution unlimited.			
11. SUPPLEMENTARY NOTES		12. SPONSORING MILITARY ACTIVITY U. S. Army Aviation Systems Command St. Louis, Missouri	
13. ABSTRACT The report presents the results of effort conducted between August 1971 and March 1972 to define criteria and to design, fabricate, and test compliant rollers to obtain the optimum detail roller profile for use in the HLH rotor transmission second-stage planetary system. Tests were performed between flat plates under HLH loading and misalignment conditions. Technical inspection and evaluation of the test results will be used for selecting the optimum compliant roller configuration for the HLH rotor transmission second-stage planetary system.			

DD FORM 1473

REPLACES DD FORM 1473, 1 JAN 64, WHICH IS OBSOLETE FOR ARMY USE.

Unclassified

Security Classification

Unclassified
Security Classification

14. KEY WORDS	LINK A		LINK B		LINK C	
	ROLE	WT	ROLE	WT	ROLE	WT
Heavy Lift Helicopter (HLH) Bearing, Compliant Roller Bearing, Planetary Bearing, Transmission Roller, Hollow-Ended						

11a

Unclassified
Security Classification

11714-72



**DEPARTMENT OF THE ARMY
U. S. ARMY AIR MOBILITY RESEARCH & DEVELOPMENT LABORATORY
EUSTIS DIRECTORATE
FORT EUSTIS, VIRGINIA 23604**

This report was prepared by The Boeing Company, Vertol Division, under the terms of USAAVSCOM Contract DAAJ01-71-C-0840 (P40). The contract was monitored and is being published by the Eustis Directorate, U. S. Army Air Mobility Research and Development Laboratory.

The objective of this specific effort was to define design criteria and to design, fabricate, and test compliant rollers to obtain the optimum detail roller profile for use in the HLH rotor transmission planetary system. Tests were performed between flat plates under HLH loading and misalignment conditions.

The results show that the hollow-ended cylindrical roller bearing configuration provides the best life performance under the expected HLH operating conditions.

This Directorate concurs with the conclusions presented herein.

The technical monitor for this effort was Mr. Wayne A. Hudgins, Heavy Lift Helicopter Project Office.

Project 1X16303D156
Contract DAAJ01-71-C-0840 (P40)
USAAMRDL Technical Report 72-62
November 1972

**TEST RESULTS REPORT AND TECHNOLOGY DEVELOPMENT
REPORT HLH/ATC COMPLIANT ROLLER BEARING DEVELOPMENT PROGRAM**

Final Report

By

J.W. Lenski, Jr.

Prepared by

**The Boeing Company, Vertol Division
Philadelphia, Pennsylvania**

for

**U. S. ARMY AVIATION SYSTEMS COMMAND
ST. LOUIS, MISSOURI**

**Approved for public release;
distribution unlimited.**

ABSTRACT

This report presents the results of effort conducted between August 1971 and March 1972 to define criteria and to design, fabricate, and test compliant rollers to obtain the optimum detail roller profile for use in the HLH rotor transmission 2nd-stage planetary system. Tests were performed between flat plates under HLH loading and misalignment conditions. Technical inspection and evaluation of the test results will be used for selecting the optimum compliant roller configuration for the HLH rotor transmission second-stage planetary system.

Planet bearing applications have generally required the use of self-aligning spherical roller bearings to accommodate planet post misalignments. A double-row cylindrical roller bearing containing a unique hollow-ended roller design has been found to be feasible for this type of application in tests under anticipated operating conditions. This bearing will accommodate a higher degree of misalignment and will provide higher capacity than a bearing containing conventional cylindrical-crowned, solid rollers. The advantages of hollow-ended roller bearing enable designs to replace the spherical roller bearing and obtain substantial weight savings and improve life and reliability in the helicopter planetary system.

Testing shows that the most severely stressed roller in a tandem set of hollow-ended rollers carries a smaller percentage of applied load than that of a corresponding roller in a set of solid rollers in an asymmetrical loading situation. This has demonstrated a favorable gain in load sharing due to the increased flexibility of hollow-ended rollers. This improvement in load sharing has reduced the maximum stress level substantially. Under the specified operating conditions used in this program, a reduction in the significant subsurface shear stress level from 120,000 to 102,000 psi was realized. The maximum bore stress of 40,000 psi indicated that the failure mode in the hollow-ended roller will be conventional outside-diameter (OD) fatigue spalling rather than rim structural failure.

FOREWORD

The roller bearing development work presented in this report has been completed in partial fulfillment of Contract DAAJ01-71-C-0840(P40). This effort was primarily a feasibility study to determine whether a proposed two-row cylindrical roller bearing design could be successfully employed in the HLH rotor transmission planetary system under specified operating conditions. The scope of work included designing, manufacturing and experimentally testing prototype compliant rollers to obtain the optimum detail roller profile for use in the HLH second-stage planetary bearing assembly operating at 18,000 pound per heaviest loaded roller set and .003 inch/inch misalignment.

This program was conducted at Rollway Bearing Company, Syracuse, New York, under the technical direction of R.B. Dalton, Chief Engineer, with R.A. Goodelle, Senior Analytical Design Engineer, as the principal investigator. Close contact with regard to program status and test results was maintained with J.W. Lenski, Senior Design Engineer, of Boeing-Vertol. Technical direction was provided by Mr. W. Hudgins, Project Engineer, Eustis Directorate, U.S. Army Air Mobility Research and Development Laboratory, Fort Eustis, Virginia.

TABLE OF CONTENTS

	<u>Page</u>
ABSTRACT.....	iii
FOREWORD.....	v
LIST OF ILLUSTRATIONS.....	ix
LIST OF TABLES.....	xvi
LIST OF SYMBOLS.....	xvii
INTRODUCTION.....	1
TECHNICAL APPROACH.....	3
Background.....	3
Statement of Problem.....	6
TEST METHOD.....	8
Test Specimen Design.....	8
Fabrication.....	8
Material.....	8
Test Specimen Preparation and Nital Etch Procedure.....	8
Etch Thickness Determination.....	9
Metallurgical Evaluation.....	9
Test Apparatus.....	9
Testing Technique.....	10
Stress Calculations.....	10
TEST DATA AND RESULTS.....	15
Roller Dimensions and Characteristics.....	15
Nital Etch Calibration Curves.....	15
Solid Roller Crown Establishment.....	15
Hollow-Ended Roller Bore Shape Selection.....	17
Hollow-Ended Roller Load Distribution Determination.....	18
Finite Element Stress Analysis Results (σ_H * Stress State).....	19
Auxiliary Finite Element Stress Analysis (σ_S * Stress State).....	20
Hertzian Subsurface Stress State in Hollow-Ended Roller (σ_S).....	20
Combined Stress State (σ_H).....	20

TABLE OF CONTENTS (Continued)

	<u>PAGE</u>
Solid Roller Comparative Stress Data.....	21
Crown Verification.....	22
CONCLUSIONS.....	23
RECOMMENDATIONS.....	25
LITERATURE CITED.....	26
DISTRIBUTION.....	118

LIST OF ILLUSTRATIONS

<u>Figure</u>		<u>Page</u>
1	Contact Area Shapes (Footprints) Created by Various Loading Conditions on a Partially Crowned Cylindrical Roller.....	27
2a	Hollow-Ended Roller Design.....	28
2b	HLH Design Study Planetary Bearing (2nd Stage Planet).....	29
3	Elastic Contact Between Loaded Roller and Flat Plate Showing Influence of Etch Film Thickness on Observed Contact Width.....	30
4	Influence of Film Thickness on Observed Contact Width (2bogs) for Various Loads and Roller Diameters.....	31
5	Etch Correction Factor as a Function of Observed Contact Width and Roller Diameter for a Constant Film Thickness.....	32
6	Example Graphical Layout and Resultant Stress Analysis of a Typical "Footprint".....	33
7	Finite Element Idealization for Rim Section of Hollow-Ended Roller (Example Grid).....	34
8	Solid Roller Design.....	35
9	Hollow-Ended Roller Design - Bore No. 1.....	36
10	Hollow-Ended Roller Design - Bore No. 2.....	37
11	Hollow-Ended Roller Design - Bore No. 3.....	38
12	Hollow-Ended Roller Design - Bore No. 4.....	39
13	Hollow-Ended Roller Design - Bore No. 5.....	40
14	Hollow-Ended Roller Design - Bore No. 6.....	41
15	Test Plate.....	42
16	Tandem Roller Fixture.....	43

LIST OF ILLUSTRATIONS (Continued)

<u>Figure</u>		<u>Page</u>
17	Test Plant Showing Areas Used in Determination of Etch Film Thickness Adjacent to Footprints.....	44
18	Baldwin-Southwark Hydraulic Loading Device...	45
19	Test Rollers Held in Tandem Position by Fixture.....	46
20	Inducing Misalignment in Test Rig by Shimming.....	47
21	Method of Applying Load to Test Rollers.....	48
22	Example of Recorded Contact Area on Actual Test Plate.....	49
23	Roller Coordinate System.....	50
24	Stress Planes (J and I) with Stresses (σ_H^*) Computed at Intersections.....	51
25	Bore Stress Orientation.....	52
26	J Stress Planes for Stress Distribution of Hertzian Contact Stresses (σ_s).....	53
27	Etch Correction Factors for a Film Thickness of 57μ inch.....	54
28	Etch Correction Factors for a Film Thickness of 86μ inch.....	55
29	Etch Correction Factors for a Film Thickness of 99μ inch.....	56
30	Footprints Created Using Solid Rollers With Various Crown Geometries.....	57
31	Footprints Created Using Solid Rollers With Various Crown Geometries.....	58
32	Footprints Created Using Solid Rollers With Various Crown Geometries.....	59

LIST OF ILLUSTRATIONS (Continued)

<u>Figure</u>		<u>Page</u>
33	Prototype Hollow-Ended Roller Bore Shape Comparison.....	60
34	Footprints Created Using Hollow-Ended Rollers With Various Bore Configurations.....	61
35	Footprints Created Using Hollow-Ended Rollers With Various Bore Configurations.....	62
36	Footprints Created Using Hollow-Ended Rollers With Various Bore Configurations.....	63
37	Graphical Layout and Resultant Load Analysis for the Most Heavily Loaded Hollow-Ended Roller Footprint (Major) in the Best Comparative Tandem Footprint Set.....	64
38	Load Required for Creating Contact Areas of Various Widths and .0394 Inch Length for Various Roller Diameters.....	65
39	Graphical Layout and Resultant Load Analysis for the Least Loaded Hollow-Ended Roller Footprint (Minor) in the Best Comparative Tandem Footprint Set.....	66
40	Stress Distribution (σ_H^* Stress State) in Hollow-Ended Roller Along Stress Plane J4 in Plane of Load ($\theta = 0^\circ$) from Bore to OD.....	67
41	Stress Distribution (σ_H^* Stress State) in Hollow-Ended Roller Along Stress Plane J5 in Plane of Load ($\theta = 0^\circ$) from Bore to OD.....	68
42	Stress Distribution (σ_H^* Stress State) in Hollow-Ended Roller Along Stress Plane J6 in Plane of Load ($\theta = 0^\circ$) from Bore to OD.....	69
43	Stress Distribution (σ_H^* Stress State) in Hollow-Ended Roller Along Stress Plane J7 in Plane of Load ($\theta = 0^\circ$) from Bore to OD.....	70
44	Stress Distribution (σ_H^* Stress State) in Hollow-Ended Roller Along Stress Plane J8 in Plane of Load ($\theta = 0^\circ$) from Bore to OD.....	71

LIST OF ILLUSTRATIONS (Continued)

<u>Figure</u>		<u>Page</u>
45	Stress Distribution (σ_H^* Stress State) in Hollow-Ended Roller Along Stress Plane J9 in Plane of Load ($\theta = 0^\circ$) from Bore to OD.....	72
46	Stress Distribution (σ_H^* Stress State) in Hollow-Ended Roller Along Stress Plane J10 in Plane of Load ($\theta = 0^\circ$) from Bore to OD.....	73
47	Stress Distribution (σ_H^* Stress State) in Hollow-Ended Roller Along Stress Plane J11 in Plane of Load ($\theta = 0^\circ$) from Bore to OD.....	74
48	Stress Distribution (σ_H^* Stress State) in Hollow-Ended Roller Along Stress Plane J12 in Plane of Load ($\theta = 0^\circ$) from Bore to OD.....	75
49	Stress Distribution (σ_H^* Stress State) in Hollow-Ended Roller Along Stress Plane J13 in Plane of Load ($\theta = 0^\circ$) from Bore to OD.....	76
50	Stress Distribution (σ_H^* Stress State) in Hollow-Ended Roller Along Stress Plane J14 in Plane of Load ($\theta = 0^\circ$) from Bore to OD.....	77
51	Stress Distribution (Principal and Shear) Along the Roller Bore at $I = 1$ in Plane of the Load ($\theta = 0^\circ$)	78
52	Elastic Radial Displacement of Hollow-Ended Roller Rim at Contact Surface.....	79
53	Principal Stress Distribution (σ_s^* Stress State) Existing in Solid Roller per 1,000 Pound/Inch Unit Load.....	80
54	Principal Stress Distribution (σ_s^* Stress State) Existing in Solid Roller for a 14,630 Pound/Inch Unit Load - Plane J7.....	81
55	Subsurface Principal Stress Disribution (σ_s Stress State) in a Hollow-Ended Roller Due to Hertzian Contact in Plane of Load ($\theta = 0^\circ$) Along J4 Stress Plane	82

LIST OF ILLUSTRATIONS (Continued)

<u>Figure</u>		<u>Page</u>
56	Subsurface Principal Stress Distribution ($\hat{\sigma}_s$ Stress State) in a Hollow-Ended Roller Due to Hertzian Contact in Plane of Load ($\theta = 0^\circ$) Along J5 Stress Plane.....	83
57	Subsurface Principal Stress Distribution ($\hat{\sigma}_s$ Stress State) in a Hollow-Ended Roller Due to Hertzian Contact in Plane of Load ($\theta = 0^\circ$) Along J6 Stress Plane.....	84
58	Subsurface Principal Stress Distribution ($\hat{\sigma}_s$ Stress State) in a Hollow-Ended Roller Due to Hertzian Contact in Plane of Load ($\theta = 0^\circ$) Along J7 Stress Plane.....	85
59	Subsurface Principal Stress Distribution ($\hat{\sigma}_s$ Stress State) in a Hollow-Ended Roller Due to Hertzian Contact in Plane of Load ($\theta = 0^\circ$) Along J8 Stress Plane.....	86
60	Subsurface Principal Stress Distribution ($\hat{\sigma}_s$ Stress State) in a Hollow-Ended Roller Due to Hertzian Contact in Plane of Load ($\theta = 0^\circ$) Along J9 Stress Plane.....	87
61	Subsurface Principal Stress Distribution ($\hat{\sigma}_s$ Stress State) in a Hollow-Ended Roller Due to Hertzian Contact in Plane of Load ($\theta = 0^\circ$) Along J10 Stress Plane.....	88
62	Subsurface Principal Stress Distribution ($\hat{\sigma}_s$ Stress State) in a Hollow-Ended Roller Due to Hertzian Contact in Plane of Load ($\theta = 0^\circ$) Along J11-J14 Stress Planes.....	89
63	Combined Principal Stress Distribution (σ_R) of $\hat{\sigma}_H$ Stress State Across Rim at Various Radii of Plane of Load ($\theta = 0^\circ$).....	90
64	Combined Principal Stress Distribution (σ_R) of $\hat{\sigma}_H$ Stress State Across Rim at Various Radii in Plane of Load ($\theta = 0^\circ$).....	91
65	Combined Principal Stress Distribution (σ_R) of $\hat{\sigma}_H$ Stress State Across Rim at Various Radii in Plane of Load ($\theta = 0^\circ$).....	92

LIST OF ILLUSTRATIONS (Continued)

<u>Figure</u>		<u>Page</u>
66	Significant Combined Shear Stress Distribution (σ_H Stress State) in Hollow-Ended Roller Along J8 Stress Plane in Plane of Load.....	93
67	Significant Combined Shear Stress Distribution (σ_H Stress State) in Hollow-Ended Roller Along J9 Stress Plane in Plane of Load.....	94
68	Significant Combined Shear Stress Distribution (σ_H Stress State) in Hollow-Ended Roller Along J10 Stress Plane in Plane of Load.....	95
69	Significant Combined Shear Stress Distribution (σ_H Stress State) in Hollow-Ended Roller Along J11 Stress Plane in Plane of Load.....	96
70	Significant Combined Shear Stress Distribution (σ_H Stress State) in Hollow-Ended Roller Along J12 Stress Plane in Plane of Load.....	97
71	Significant Combined Shear Stress Distribution (σ_H Stress State) in Hollow-Ended Roller Along J13 Stress Plane in Plane of Load.....	98
72	Significant Combined Shear Stress Distribution (σ_H Stress State) in Hollow-Ended Roller Along J14 Stress Plane in Plane of Load.....	99
73	Respective Graphical Layout and Resultant Load Analysis for the Most Heavily Loaded Solid Roller Footprint (Major) in the Tandem Footprint Set.....	100
74	Respective Graphical Layout and Resultant Load Analysis for the Least Loaded Solid Roller Footprint (Minor) in the Tandem Roller Footprint Set.....	101

LIST OF ILLUSTRATIONS (Continued)

<u>Figure</u>		<u>Page</u>
75	Hertzian Subsurface Principal Stress Distribution in Solid Roller Along J7 Stress Plane (Example) in Plane of Load.....	102
76	Hertzian Subsurface Shear Stress Distribution in Solid Roller Along J7 Stress Plane (Example) in Plane of Load.....	103
77	Comparison of Maximum Subsurface Shear Stress Distribution Existing in Solid and Hollow-Ended Rollers.....	104
78	Footprint Shapes at Various Loads and Alignments Confirming Final Hollow-Ended Roller Design.....	105
79	Etch Correction Factors for Various Film Thicknesses Using 1.25 Diameter Roller.....	106
80	Life Comparison - HLH Planet Bearing Candidates.....	107

LIST OF TABLES

<u>Table</u>		<u>Page</u>
I	Test Roller Crown Geometries.....	108
II	Chemical Composition of Test Plates and Rollers.....	109
III	Test Roller Data.....	110
IV	Footprint Test Data.....	111
V	Critical Footprint Dimensions Data Averaging.....	112
VI	Observed Footprint Measurement and Corrections.....	113
VII	Hollow-Ended Roller Footprint Load Analysis.....	114
VIII	Solid Roller Footprint Load Analysis.....	116

LIST OF SYMBOLS

b	contact area half-width, inch
b_n	incremental contact area half-width, inch
$2b_{OBS}$	observed contact area width, inch
$2b_{REAL}$	apparent (actual) contact area width, inch
B/D	roller bore ID to OD ratio
d	roller diameter, inch
ECF	etch correction factor, $\frac{2b_{REAL}}{2b_{OBS}}$
l_n	incremental contact length, inch
P_n	incremental load, pound
P_n/l_n	incremental unit load, pound/inch
P_o	normal maximum Hertzian pressure, psi
R	crown radius, inch
t	film thickness, inch
x	any depth below surface, inch
σ	principal stress, psi
$\sigma_R = P_o$	maximum principal radial contact stress, psi
σ_H^*	approximate stresses from finite element analysis for hollow-ended roller, psi
σ_S^*	approximate stresses from finite element analysis for solid roller, psi
$\hat{\sigma}_H$	combined stresses in hollow-ended roller, psi

LIST OF SYMBOLS (Continued)

$\hat{\sigma}_s$	Hertzian subsurface contact stresses, psi
τ	shear stress, psi
α	crown length, inch
δ'	crown drop, inch
I	denotes stress plane
J	denotes stress plane

Subscripts

H	denotes hollow-ended roller
R	denotes radial direction
S	denotes solid roller
Z	denotes axial direction
θ	denotes circumferential direction

INTRODUCTION

In order to meet the ever-increasing endurance and power demands on helicopter bearing systems, optimization of bearing materials and design is required. Misalignment has been found to drastically shorten bearing life in applications where the bearings are subjected to significant deflections. Tailored crowning of rollers may alleviate this problem somewhat; however, such modifications must be supplemented if bearing life is to be improved.

Significant breakthroughs in two areas of bearing technology have permitted the use of cylindrical roller bearings where spherical roller bearings were formally specified. An improved method has been developed by Rollway Bearing Company for permanently recording the elastic contact area or "Footprint" created from roller/race contact on a chemically etched plate or race (Figure 1). In the past, the forecasting of stress levels and associated life of a rolling element under misalignment required the accurate determination of the shape of the mutual contact. The "Footprint" technique also provides the means of analyzing this area to determine the load and stress distributions. Visual inspection of the shape alone qualitatively displays a wealth of information about loading conditions, contact area aberrations and existing conditions of misalignment. This information is useful in the solution of specific application problems which, at present, may only be grossly estimated by other methods. Of great experimental benefit is the advantage of being able to visually inspect the influence of roller crowning on the contact area and in particular, end of contact effects for specific loading and misalignment conditions. This means that for a special application the proper crown may be easily and accurately determined.

The second Rollway advancement in the state of the art involves a modification of structural roller design in which both ends of the roller are recessed (Figure 2a). Development of this hollow-ended roller was initiated with the objective of increasing the range of misalignment which a cylindrical roller bearing could endure while also increasing reliability and life. This is best achieved by improving the load distribution on the roller. The optimum load distribution may be obtained by tailoring both the shape of the recessed end and the roller crown. The net result will be a contact area without end of contact effects (blunt end - high stress) and a maximum width substantially less than that found from a contact created by a solid roller with an

identical crown under the same loading and misalignment conditions. The life of elements in rolling contact may be determined by the maximum contact stress level (resolved into a subsurface shear stress distribution) which is directly related to the dimensions and shape of contact - i.e., stress increases in proportion to increasing width, and life is inversely proportional to some high power of stress.

This unique roller structural design configuration permits improved load distribution over the conventional solid roller type. This roller development, which is dependent on an accurate assessment of the influence of bore shape and crown geometry on contact area, is made possible by the "Footprint" technique. Applying this type of roller design to a cylindrical roller bearing extends the range of misalignment which the bearing may tolerate and ensures a reliable life prediction in excess of that estimated for other bearing types.

TECHNICAL APPROACH

BACKGROUND

Planet bearing sizing for B-10 fatigue life requirements has a direct influence on the pitch diameter size of the planetary ring gear. To minimize the size and weight of the ring gear, the capacity of the planet bearings must be improved. Boeing-Vertol's current design practice is to use self-aligning spherical roller bearings to accommodate planet bearing post misalignments. For the HLH 2nd-stage planetary system, trade studies were conducted to determine methods of providing improved bearing capacity at reduced weight and size. The design study was conducted using the following ground rules:

1. Ring gear pitch diameter will be 32.95 inches with a planetary ratio of 3.674.
2. The bearing cubic mean load to the rotor transmission of 7,200 HP at 156 rpm will be used for life sizing.
3. The bearing maximum load to the rotor transmission will be 10,400 HP at 156 rpm.
4. Allowable equivalent alternating stress of the backup ring will be $\pm 29,000$ psi on the OD and $\pm 42,000$ psi on the ID.
5. Roller L/D ratio will be 1.2 to 1.5.
6. Cage web spacing will be 20% of roller diameter.

The results of the above study showed that a cylindrical roller bearing design (Figure 2b) using a 1.25-inch-diameter roller and a length of 1.50 inches provided a minimum B-10 life of 2000 hours while meeting all of the above design objectives. The only problem associated with this type of bearing design is to provide a capability for accommodating the planet post deflections expected in the HLH planetary system without degrading the calculated B-10 life.

To reduce the influence on fatigue life of an asymmetrically loaded cylindrical roller bearing, the use of compliant (hollow-ended) cylindrical rollers to supplement the standard crown modification was implemented to provide the desired misalignment capability for the HLH planetary bearing design. The unique hollow-ended roller design has been developed by

the Rollway Bearing Company, Syracuse, New York. Rollway was subcontracted to investigate the use of such a design in the HLH rotor transmission planetary system.

The "Footprint" technique¹ is the key to accurately determining the static contact areas from which comparisons may be made to select a bore/crown relationship yielding the best load distribution for the specified operating conditions. Permanent recording of contact area is made possible by using chemically etched steel plates. When steel is subjected to the action of a nitric acid solution, a thin layer composed mainly of carbon remains as a result of the reaction. The thickness of this film is directly proportional to reaction time, surface cleanliness, material carbon content and etch media strength. A rolling element may be placed on this etched plate and loaded to the desired degree. Upon load removal the contact area or "Footprint" is clearly visible on the etched surface. This area is significantly modified by the apparent load-carrying ability of the inelastic carbon coating, the degree being directly proportional to its thickness as illustrated in Figure 3. Calibration curves must be determined, for the diameter roller being studied, that account for this influence of film thickness on observed contact dimension to yield the contact area that in reality exists before the load is withdrawn. Contact area data obtained from symmetrically and statically loading selected sizes of steel cylindrical rollers (no crown, square ends) on dry (unlubricated) test plates having etched surfaces of various film thicknesses are presented in the form of curves (Figure 4). The curve intersection with the ordinate axis indirectly yields the real contact width (no etch) for any particular roller diameter, length and applied load. Having now established the differences between observed and real contact width dimensions ($2b_{OBS}$, $2b_{REAL}$) due to a thin film on one of the two approaching surfaces, an etch correction factor (ECF) may be defined as

$$ECF = \frac{2b_{REAL}}{2b_{OBS}}$$

Data from curves in Figure 4 may be used to establish etch calibration curves for the three roller diameters investigated for any film thickness (162 μ inch, for example) as illustrated in Figure 5. Extrapolation of three curves (such as these) at the desired film thickness will yield a calibration curve for a roller of any diameter. Having a method now to correct the error associated with recorded contact width dimensions ($2b_{OBS}$), a straightforward approach may be employed to determine the load distribution prescribed

by the contact area ("Footprint") created by a partially crowned cylindrical roller under asymmetrical loading. The desired "Footprint" selected for study is measured and constructed graphically to an enlarged scale as shown in Figure 6 and called the observed area. The proper calibration curve is developed and used to correct all observed dimensions. After this correction, the new area is called the apparent contact area which truly represents the bulk elastic deformation that has taken place. This area may be divided into numerous segments, l_n , each individual length being dependent upon the "Footprint" outline. An equivalent contact half-width (b_n) is found for each segment by drawing the horizontal line through the corrected outline that makes it a rectangular segment equal in area to that of the original section. This equivalent area is now assumed to be the classical rectangular contact area created by an uncrowned roller against a flat plate yielding a contact half-width, b_n , predicted by the Hertz equation (plane stress conditions assumed along the entire contact length). Applying the Hertz equation in the following form

$$P_n = \frac{b_n^2 l_n}{(1.4 \times 10^{-4})^2 dC}$$

the incremental loads necessary to create each segment of the apparent "Footprint" may be calculated. Unit load values (P_n/l_n) may be determined next and plotted (example, Figure 6).

This accurate description of loading on the rolling element is of great importance, as it serves as the basis for the determination of the stress distribution in the body. The contact stresses in a solid roller due to the deformation of a local area from the applied load contact are determined in a straightforward manner using classical equations. However, analyzing the stress distribution in a hollow-ended roller is not a routine problem; additional stresses are involved due to rim deflection which must be combined with the contact stress state to yield an accurate stress determination. A three-dimensional finite element elasticity study was employed to determine the stress state in the flexible rim section due to deflection². This computer program provides a numerical solution for the stresses induced in a conical shell elastically supported at one end and under the influence of an asymmetrical self-equilibrating line load. The finite element method involves dividing the rim section up into a finite number of quadrilateral elements as displayed, for example, in Figure 7 with the stress results read out at their centroids. The load distribution data obtained from

the "Footprint" may be expressed as any function of R & Z and the Fourier series in θ and is used as input data for the computer analysis. The results of the finite element analysis when properly combined with the local Hertzian contact stress yield an accurate description of the subsurface shear stress state in the hollow-ended roller which may be compared to the subsurface shear stress state existing in a solid type roller subjected to identical operating conditions. Knowledge of the peak bore stress and maximum subsurface shear stress allows a decision on roller feasibility to be made. The stress results in the plane of the load ($\theta = 0^\circ$) need only be obtained, as the stresses at $\theta = 90^\circ$ are much less.

STATEMENT OF PROBLEM

The main gearboxes of current Vertol helicopter power transfer systems use spherical roller bearings in their planetary gear system. With ever increasing power requirements, the use of this type of bearing severely restricts the use of optimum gear sizes and the potential weight reduction in this area. Spherical roller bearings have been mainly used for their ability to accommodate post deflections and misalignments which are experienced in the planetary gear system.

Trade studies have shown that cylindrical roller bearings could provide greater capacity in the same size bearing and thus provide higher fatigue life. The only objection to cylindrical roller bearings is their inability to accommodate severe misalignments. Field experience and testing of cylindrical roller bearings, even with special crowned rollers, under misalign condition show a drastic reduction in fatigue life. Therefore, to take advantage of the higher capacity ratio, a significant improvement in misalignment capability must be incorporated into the cylindrical roller bearing.

The primary concern with this program is to determine the feasibility of using a tandem cylindrical roller bearing with modified hollow-ended rollers to function under severe operating conditions in the HLH rotor transmission 2nd stage planetary system. Static roller tests were performed to establish the optimum roller crown and hollow-end configuration which is capable of supporting high loads and misalignments. The test loads were established by bearing computer analysis of the HLH rotor transmission 2nd stage planet bearing which accounted for internal load distribution, internal clearance and flexibility of the planet gear. Testing was conducted between tandem hollow-ended rollers

and flat plates to determine the load distribution on the most heavily loaded rollers under the following specified load and deflection conditions:

1. Load Condition - 18,000 Pounds (Equivalent to 10,400 HP to rotor transmissions)

12,000 Pounds (Equivalent to cubic mean load of 7200 HP to rotor transmissions)

8,000 Pounds (Lower power rating)

2. Misalignment - .003 inch/inch

The results of these tests determined the feasibility of using a bearing with tandem hollow-ended cylindrical rollers operating at high loads and misalignment.

TEST METHOD

TEST SPECIMEN DESIGN

The first phase of this program included a solid roller design on which ten crown variations were generated. The basic 1.25 diameter x 1.50 length roller is shown in Figure 8; the various crown geometries are listed in Table I. In conjunction with the crown study, six configurations of hollow-ended rollers were designed as shown in Figures 9 thru 14. One of the ten solid roller crowns was selected (after a "Footprint" study) for use on the six hollow-ended roller variations.

FABRICATION

All rollers, both solid and hollow-ended, test plates and a fixture to hold two rollers in tandem were fabricated by Rollway. The finished rollers are shown in Figures 8 thru 14. The test plate and fixture hardware are shown in Figures 15 and 16, respectively.

MATERIAL

As this program was basically a feasibility study which did not include dynamic testing, and the nature of the experimental test work was not material oriented, it is sufficient to describe the test parts materials as follows.

All rollers were constructed from grade 8620 (ASTMA534) carburizing steel which is used primarily in the manufacture of ball and roller bearings.

The test plates are chrome #1 (ASTMA485-grade 1) which is a high hardenability modification of 52100 steel used in the manufacture of ball and roller bearings.

TEST SPECIMEN PREPARATION AND NITAL ETCH PROCEDURE

As discussed earlier, the etched test plate and "Footprint" recording is the basic technique necessary to carry out this development program. All contact areas were recorded on etched, thru hardened, highly finished, good bearing quality steel plates. A good texture (3 to 5 μ inch) is required to assist in judging the "Footprint" boundaries on the etched surface. Each test segment (all same size and thickness) was

immersed in light oil immediately after surface finishing to limit the formation of an oxide film which could affect the chemical etching operation. Prior to etching, the segments were thoroughly degreased in trichloroethylene to remove the oil. After immediate forced air drying, each segment was allowed to sit in ambient air for not more than 2 minutes before immersion into the nitric acid solution. A 10% laboratory grade solution by volume mixed with water at tap outlet temperature was used throughout. Each segment was individually immersed in the etch solution and agitated for 20 seconds, followed immediately by bathing in clear 120°F water for 10 seconds, then quickly forced air dried, resulting in a uniform, water mark free carbon film on each plate.

ETCH THICKNESS DETERMINATION

Film thickness was measured immediately adjacent to each "Footprint" selected for study by using a sensitive electronic indicator pickup which indicated the difference in height between an area from which the etch had been removed and that of a neighboring undisturbed etched surface. Each such thickness determination was the result of averaging six passes of the indicator pickup over the subject area. The final etch thickness value selected for a plate was obtained by averaging the values from local areas. Examples of such areas may be seen in Figure 17. Calibration curves were then developed for these final average values by using extrapolation of data published in earlier work.¹

METALLURGICAL EVALUATION

No formal metallurgical examinations were conducted on existing test parts due to reasons described in the Materials section. The general condition of the two subject steels is presented in Table II.

TEST APPARATUS

All "Footprint" recording (loading rollers onto etched flat plates) was performed using a 200,000 pound capacity Baldwin-Southwark universal hydraulic tester as a loading device (Figure 18). To compensate for misalignment created in the Baldwin due to compression loading, a die set was positioned on the loading table which in effect transferred the applied load to the test plate and roller in a plane parallel to the loading head. The test plate sat on top of a 4 inch x 4 inch x 6 inch steel column which rested on the base of the die set. To obtain desired misalignments, the steel column was shimmed on one side. The height of this column

prevented any undesirable bending effects when shimming was employed. The accuracy of load was verified to within 1%.

TESTING TECHNIQUE

Sets of two rollers selected for "Footprinting" were cleaned free of oil and dried prior to placing them and the roller test fixture onto the test plane (Figure 19). With the steel column subjected to the desired misalignment by shimming (Figure 20), the test plate was positioned on top of the column. The die set top plate was lowered until soft contact with the rollers was made. Once the Baldwin-Southwark head (stationary) engaged the die set plate (Figure 21), the desired load was hydraulically applied to the roller set thru the moving table. Upon load removal, the Baldwin head was withdrawn and the test plate, rollers and fixture were carefully removed.

The permanently recorded elastic contact area (Figure 22) was now ready for measurement. A microscope and stage with a .001 inch increment scale in the transverse direction (2b) and .04 inch increment scale in the longitudinal direction (length) was used to measure the contact dimensions. The (2b) dimension, which is the critical value when considering load and stress distributions, is accurate within .0005 inch. All contact measurements were made with the same instrument in a temperature-controlled room. The plates, rollers and "Footprints" were all identified according to an established numbering system.

STRESS CALCULATIONS

In order to properly forecast rolling element life, a measure of stress becomes the basic guide as to whether a particular bearing is feasible for a specific application. Determination of an absolute value for the operating stress requires refined knowledge of the contact area as modified by the lubricant film, the addition of traction shear stresses as created by the dynamic contact, consideration of residual stresses in the roller body and race, and the resultant stress. Fatigue testing is generally employed to determine life under actual operating conditions. However, in design applications where no corresponding parts yet exist, a measure of the static stresses may serve as the basis for a practical stress evaluation, particularly in studies where stress distributions are to be compared relative to one another. A judgment may be made as to feasibility of design if the significant (maximum) subsurface shear stress is known. In the case of a hollow-ended roller, the shear stresses in

the bore are also of equal importance. Knowledge of these two stress values, in addition to experience gained previously through numerous fatigue tests and field test results, allows a realistic assessment of a proposed bearing design to be made. The Hertzian contact stresses at the surface created in a dry, static, elastic contact area may be determined using classical equations. The maximum Hertz pressure or maximum radial stress, σ_R , is calculated from

$$\sigma_R = \frac{2 P_n}{\pi b_n l_n}$$

where P_n , b_n , and l_n are values obtained from the "Footprint" analysis of the subject contact area. The roller coordinate system showing principal directions at and near the roller surface may be seen in Figure 23.

The subsurface principal and shear stress distributions may be determined in a manner suggested by Thomas and Hoersch.³ The principal stresses at any depth (σ_s stress state) may be calculated from

$$\hat{\sigma}_s \Big|_z = \sigma_R \left[0.6 \left[\sqrt{1 + \left[\frac{x}{b_n} \right]^2} - \left[\frac{x}{b_n} \right] \right] \right]$$

$$\hat{\sigma}_s \Big|_\theta = \sigma_R \left[\frac{\left[\sqrt{1 + \left[\frac{x}{b_n} \right]^2} - \left[\frac{x}{b_n} \right] \right]}{\sqrt{1 + \left[\frac{x}{b_n} \right]^2}} \right]^2$$

$$\hat{\sigma}_s \Big|_R = \sigma_R \left[\frac{1}{\sqrt{1 + \left[\frac{x}{b_n} \right]^2}} \right]$$

where $\hat{\sigma}$ means an accurate assessment of stress and X = any depth below surface. Examples of subsurface principal and shear stress distributions may be seen in Figures 75 and 76, respectively. These curves define the stress state due to the effects of elastic deformation at the roller surface and describe fully the static stress distribution that exists in the solid roller. For the hollow-ended roller case, however, this stress state is modified by the bending effect of the flexible rim. A computer program, based upon a finite element, direct stiffness method is used to determine the three-dimensional stress state existing in the hollow-ended roller rim due to rim deflection. The unit loading data, resulting from "Footprint" analysis, is used as input data for this program. This method involves dividing the rim structure into a number of finite, quadrilateral elements with stresses computed at their centroids. All such midpoints in this grid may be connected to form stress planes I and J (Figure 24). These planes become an important graphic aid in understanding the data evaluation. To describe the principal and shear stress orientation at a location just inside the bore surface, consider an infinitesimal cube with one face in the plane of the bore surface (Figure 25). Since there can be no shear on the free surface, then the normal to this surface is a principal direction with the respective stress, σ_n . Next, due to symmetry, there is no shear on the plane defined by $\theta = 0^\circ$ (see Figure 23). This, then, is a principal direction and σ_θ a principal stress. Finally, since the three principal directions must be mutually orthogonal, the third principal direction is tangent to the bore surface and in the plane $\theta = 0^\circ$ with the principal stress denoted, σ_t . As is conventional, the maximum shears occur on four faces of the cube which is rotated about one of the normals, 45° from the principal directions. The largest of these shears is determined (considering use of the maximum shear theory) by taking the absolute value of the maximum algebraic difference between two stresses. These stresses calculated along the bore surface are relatively accurate due to the mathematical handling of the loading as represented by the higher terms of the Fourier series. For increasing radial distances from the bore, the computed stresses due to rim deflection tend to become less accurate as, in order to implement the finite element technique, the Hertzian parabolic distribution of load is replaced by a concentrated line load. In other words, for the moment, the local contact stress state has not been considered. An example stress distribution due to rim deflection is shown in Figure 45 and is denoted by σ_H^* , or the approximate results for the hollow-ended roller.

In order to accurately describe the stress state existing in the roller rim under the plane of the actual load, $\theta = 0^\circ$ (stresses will be at a maximum in this region while decreasing for increasing values for " θ "), which now includes the Hertzian contact stresses combined with the stress distribution found from the finite element analysis, an auxiliary finite element analysis of an infinite solid roller is required to properly combine the two stress states. The results of such an auxiliary analysis are shown in Figure 54 with the stresses designated, $\bar{\sigma}_S^*$, or the approximate results for the solid roller. The finite element grid and J stress planes are the same as employed in the hollow-ended roller analysis. The actual stress distribution in the hollow-ended roller can now be computed by assuming that the difference between the exact stress ($\bar{\sigma}$) in the solid (S) roller and the exact stress in the hollow (H) roller is the same as the difference between the approximate ($\bar{\sigma}^*$) analyses:

$$\bar{\sigma}_H - \bar{\sigma}_S = \bar{\sigma}_H^* - \bar{\sigma}_S^* \quad 1$$

This is reasonable since the approximate analyses include the basic behavior and do not include the self-equilibrating local effects at the contact area.

In summary, the desired stress state, $\bar{\sigma}_H = \bar{\sigma}_S + \bar{\sigma}_H^* - \bar{\sigma}_S^*$, can now be calculated where $\bar{\sigma}_H$ is an accurate determination of the principal stress distribution in the hollow-ended roller, $\bar{\sigma}_S$ is the exact or classical subsurface principal stress due to Hertzian contact alone, $\bar{\sigma}_H$ denotes the finite element stress analysis results (principal stresses) for a hollow-ended roller, and $\bar{\sigma}_S^*$ denotes the results of an auxiliary finite element analysis on a corresponding solid roller. The stress planes employed for displaying the $\bar{\sigma}_S$ stress distribution below the roller surface are shown in Figure 26. For practical reasons, this grid is different from that employed in the finite element stress analyses. Inspection reveals, however, that respective J planes have the same surface starting point. As the stresses due to Hertzian contact decay rapidly below the OD surface with small differences existing in respective J plane coordinates for small depths below the surface, little error is involved in the calculation of combined stress $\bar{\sigma}_H$, due to non-parallelism of respective J planes. Once the principal stresses $\bar{\sigma}_R$, $\bar{\sigma}_Z$, $\bar{\sigma}_\theta$ for the $\bar{\sigma}_H$ stress state are calculated using formula 1, the significant subsurface shear stress, which may be used as a failure criterion, is determined by applying the maximum shear stress theory

$$\tau_{RZ} = \frac{\bar{\sigma}_R - \bar{\sigma}_Z}{2}$$

As the maximum shear stress occurs near the roller OD and is in general much greater than that found along the hollow-ended roller bore surface, it is correct to assume a sub-surface failure mode (this is fully supported by previous fatigue test results).

TEST DATA AND RESULTS

ROLLER DIMENSIONS AND CHARACTERISTICS

Critical test roller dimensions and material properties were measured and recorded in Table III. These specific values were considered in the test program and not the design dimensions shown in Table I and Figures 9 thru 14 (see Test Specimen Design section).

NITAL ETCH CALIBRATION CURVES

In order to accurately determine the elastic contact area dimensions from footprint measurements on etched plates, calibration curves are necessary to correct the observed measurements for the influence that the etch thickness has on these dimensions. Using data published in earlier work¹ (Figure 5), etch calibration curves may be constructed for film thickness of 57, 86, and 99 μ inch (Figures 27, 28, and 29, respectively). These thicknesses were determined to exist on the three test plates using the procedure described in the Etch Thickness Determination section. Any measured dimension may now be corrected to yield the real dimension allowing construction of the entire true "Footprint".

SOLID ROLLER CROWN ESTABLISHMENT

The first phase of the experimental test program was to establish the optimum solid roller crown geometry for the specific operating conditions of 18,000 pounds applied load per roller set and .0005 inch/inch misalignment. This was accomplished by applying numerous crown variations to solid rollers; recording the contact areas or "Footprints" generated at these conditions on a dry, flat plate; and qualitatively evaluating the areas with respect to end of contact effects (blunt ends).

Initially, eight crown variations, 1-8 (Table I), were investigated resulting in "Footprint" sets (Figures 30 and 31). These crowns were selected to qualitatively determine the influence of crown geometry on load distribution for this particular diameter roller. Similar development work performed at Rollway in recent years has shown that the cylindrical flat length should be as long as possible (short crown length) with the end of contact shape controlled by crown drop adjustment. Considering these results in the Boeing-Vertol program permits a reduction in the number of variables that have to be evaluated with respect to

determining their influence on the shape of the contact area. In summary, the general approach used in this part of the program was to specify as short a crown length as practical and control the crown drop by varying the crown radii.

Looking at specific crown geometries (Table III) actual measurements, and the associated "Footprints" (Figures 30 and 31) leads to the following evaluation and discussion. The "Footprints" created with crown #1 rollers (.0005 inch crown drop) exhibit blunt ends under no misalignment as well as .0005 inch/inch - obviously unacceptable. The next four crown variations (2-5) feature approximately the same crown drop (.0006-.0008 inch) but with various crown lengths. Inspection of their respective contact areas shows only slight, if any, improvement at the end of contact - still undesirable. Applying crown #6, which has a greater drop, improves the load distribution for the case of no misalignment but does not substantially modify the contact area created at .0005 inch/inch misalignment. Increasing the crown drop to (.0010) crown #7, and increasing the flat length slightly, shows very favorable contact areas for no misalignment with improved ones at .0005 inch/inch. The "Footprint" associated with crown #8 reflects a very large crown drop and short flat length. The shape at the ends of contact is superior, but at the expense of drastically shortening the contact length which is associated with substantial increase in the contact width (2b). The 2B dimension may be used as a measure of stress. Remembering that roller life is inversely proportional to some high power of the significant stress, the case for a short flat length is highly undesirable.

The above evaluation of the eight crown variations has shown that only crown #7 offers a reasonable load distribution as exhibited by the "Footprints". However, this may be improved. Two additional crown variations (9 and 10) were selected for evaluation in order to further improve the end of contact shape. The actual crown geometries are shown in Table III with the resulting "Footprints" displayed in Figure 32. Visual inspection shows that the "Footprints" resulting from crown #10 variation roller display a satisfactory contact shape for the operating conditions of 18,000 pounds and .0005 inch/inch misalignment. This crown geometry becomes even more desirable when considering that the above load condition is for maximum load. In reality, the loading will, for a high percentage of the time, be lower than 18,000 pounds. Hence, the contact area created using a solid roller with #10 crown will exhibit a more pointed end of contact (which is desirable as opposed to blunt).

Summarizing, crown #10 (Table I) has been selected for the operating conditions specified.

HOLLOW-ENDED ROLLER BORE SHAPE SELECTION

The second phase of the experimental test program involved (1) generating the solid roller crown selected from the first phase on the same sized hollow-ended rollers constructed with six different bore configurations (bore shape comparison illustrated in Figure 33), and (2) establishing the best bore design by evaluation of the respective load distributions on the roller considering end of contact shape and maximum contact width dimension, resulting from applying the specified applied load of 18,000 pounds per roller set and .003 inch/inch misalignment. The resulting "Footprint" sets are displayed in Figures 34 thru 36. Because of the critical nature of these tests, "Footprints" were duplicated on three different test plates. The entry numbers identifying the "Footprint" sets in these figures may be related to dimensions "Footprint" recorded in Table IV. These contact areas were measured, etch thickness determined, calibration curves developed, and observed measurements corrected in the manner described in previous sections. The corrected dimensions for each specific "Footprint" are also found in Table VI. The maximum width and end of contact width dimensions may be used to evaluate the "Footprints" with respect to obtaining the best load distribution. The calibration areas referred to in this table may be seen in Figure 17, as one example. The etch thickness assigned to a "Footprint" represents an average value for that particular plate. Entries one thru twenty include applications of "Footprints" on different test plates. For each bore shape, at least two "Footprints" were recorded and in some cases four. Once the observed dimensions were corrected for a particular bore design, they were averaged to yield the results found in Table V. Solid roller "Footprint" test data is also included for comparison purposes. Inspection of the values in the 2b (MAX) and 2b (END) columns clearly shows that bore configuration #3 distributes the load in the most favorable manner for the specified operating conditions of 18,000 pounds load and .003 inch/inch misalignment. The "Footprint" created using this design exhibits the least width and end of contact dimensions which is a measure of stress. Comparing these dimensions to those displayed by a solid roller "Footprint" shows great improvement by using this particular hollow-ended roller. In addition, any hollow-ended roller "Footprint" shape is superior to that created by the conventional solid roller type of similar size.

HOLLOW-ENDED ROLLER LOAD DISTRIBUTION DETERMINATION

Having previously established the best contact area, considering shape and maximum width dimension, to be entry 3, Table V (illustrated in Figure 34), it may be measured (Table VI) and constructed graphically in enlarged fashion (Figure 37). This observed area, as it is called, may be corrected to yield the true shape or apparent contact area by employing the appropriate etch correction curve (Figure 27). To determine that portion of the 18,000 pound applied load which has been used to create the heaviest loaded roller "Footprint" in the set, the apparent area has been divided into 24 segments, whose equivalent half-widths (b_n) are found by drawing the horizontal line through the corrected outline that makes them rectangular segments equal in area to that of the original sections. Applying the following Hertzian equation

$$P_n = \frac{b_n^2 l_n}{(1.4 \times 10^{-4})^2 dC}$$

allows the determination of the incremental loads necessary to create each segment (Table VII). Curves aiding in the determination of P_n are found in Figure 38. Summation of these loads yields 16,026 pounds. The second "Footprint", in the tandem set, Figure 39 (shows corrected contact area only), is constructed and analyzed in the same manner, yielding 3324 pounds. Addition of these resultant loads supported by each roller (Table VII) shows the total to be in excess of the known applied load by 7½% or 1350 pounds. Even though the source of this error is not clear, the corrected contact area outline may be adjusted in both "Footprints" to yield areas that precisely account for the 18,000 pound load (denoted by "Refined Corrected Area or Apparent Contact Area"). All dimensions simply have been multiplied by a factor of .925. This is a valid procedure as the etch correction factors initially applied have already established the correct "Footprint" shape/outline. The 7½% error is assumed to be the same for each contact dimension resulting in a slightly reduced area, but retaining its shape. The refined results for each "Footprint" may be seen in Table VII (results for the most heavily loaded roller, major, are constructed in graphical form, Figure 37). The incremental unit loads simply calculated from P_n/l_n are plotted also in Figure 37 with a smooth continuous curve connecting the points. Inspection of this curve shows the peak value to be 15,200 pounds and located in the area of the crown/flat length

junction. Unit load values from the plot are used as coefficients in the Fourier series equation which forms input data for the finite element analysis computer program.

FINITE ELEMENT STRESS RESULTS (σ_H^* STRESS STATE)

The finite element analysis employed yields the stress distribution throughout the hollow-ended roller rim due to rim deflection created by a line load. The rim structure of the roller has been divided into a grid network of quadrilateral shaped elements with stresses computed at their centroids. Connecting such centroids in a vertical direction allows stress planes to be developed, denoted by the letter J, Figure 23. Formation of such planes permits graphical representations of the stress distributions along a particular plane clearly showing how the stresses vary according to location. The three principal stresses (σ_H^* stress state) may be displayed in this manner along planes J4 thru J14 in Figures 40 thru 50, respectively. All three, σ_R , σ_θ , and σ_z , are compressive at the surface due to the radial displacement of each "ring" section of the rim (considering rim to be divided into a series of rings) being unequal with respect to its neighbors.² As the roller bore area is approached, the stresses become positive (tension) except for σ_R which goes to zero (there can be no radial (n direction) stress at this surface, as there is no external loading applied there). Inspection of the computer results in the bore region shows a maximum shear stress ($\tau_{\theta\phi}$) of approximately 40,000 psi located just inside the bore surface in the vicinity of stress plane J25. The stress distribution along the entire bore surface is shown in Figure 51. This value of 40,000 psi is not considered to be at a critical level, because stress concentrations arising from bore finish are minimal. As noted earlier, the stresses near the bore are very accurate while decreasing in accuracy as the roller OD is approached. Stresses at and near the OD are only valid when used in proper formulation, which combines various stress states to yield an accurate description of the stresses existing in the actual application. This computer analysis also determines the elastic displacement of the hollow-ended roller OD, with the deflection curve (Figure 52) showing a maximum deflection (.00157) associated with the peak unit loading imposed on the roller OD. As expected, the subsurface principal stresses created from this deflection are highest in this load region (Figures 40 thru 50).

AUXILIARY FINITE ELEMENT STRESS ANALYSIS (σ_s^* STRESS STATE)

In order to determine the stress state in the hollow-ended roller due to both rim deflection and local contact stresses, an auxiliary finite element analysis of a solid roller subjected to the same load distribution as the hollow-ended roller is required. Stress results for 1000 pound/inch unit loading may be computed and plotted (Figure 53). From these curves, stress distributions along any J plane associated with a unit load may be calculated (Figure 54, for example). The finite element grid (and stress planes) employed in this analysis is identical to that developed for the hollow-ended roller (Figure 23). These stresses (σ_s^*) in themselves are of no value, but are necessary in the formulation (formula (1)) for determining the combined stress state.

HERTZIAN SUBSURFACE STRESS STATE IN HOLLOW-ENDED ROLLER ($\hat{\sigma}_s$)

The finite element analysis has yielded the stresses created due to rim deflections. Now, the stresses created by Hertzian contact at the surface must be determined and properly combined to the above stress state to yield the accurate existing stress state. The Hertzian subsurface principal stress distributions are determined using the classical approach of Thomas and Hoersch.³ The solutions are most easily obtained by a computer program which reads out the results in curve form (Figures 55 thru 62) along the J stress plane locations seen in Figure 26. As shown, all three orthogonal stresses are compressive at the surface and decay rapidly for increasing values of depth. The highest surface contact stress is 350,000 psi which is still within the elastic limit.

COMBINED STRESS STATE ($\hat{\sigma}_H$)

The actual stress distribution existing in the hollow-ended roller under the influence of the load distribution shown in Figure 37 may now be determined by algebraically combining the results reported in the previous sections using formula 1 or

$$\hat{\sigma}_H = \hat{\sigma}_s + \sigma_H^* - \sigma_s^*$$

The principal combined stresses (σ_R , σ_θ , σ_z) are calculated and plotted in Figures 63, 64 and 65 respectively. The highest surface contact stress is 380,000 psi which is still within the elastic range. The significant (maximum)

subsurface shear stress may be calculated by taking half the difference between any two principal stresses. This significant stress (τ_{Rz}) is plotted along planes J8 thru J14, Figures 66 thru 72 respectively. A maximum value of 102,000 psi is reached approximately .0125 to .0150 inch below the roller surface in plane J14. This value levels off and remains the same in planes 15 and 16, then gradually decreases for increasing J plane numbers. The shear stress, $\tau_{R\theta}$, distribution (not shown) reaches a peak value of 98,000 psi, .0225 inch below the surface in plane J14. The remaining combined shear stress, $\tau_{\theta z}$, is small and need not be discussed. The significant shear stress value of 102,000 psi in itself is high, but not critically so. It must also be remembered that the operating conditions, which dictate the load distribution on the roller, were specified rather severely and do not reflect, in all probability, a large percentage of the total bearing running time. As this stress is substantially higher than the maximum bore stress (40,000 psi), the expected mode of failure will be conventional subsurface (OD) fatigue as in the case of a solid roller.

SOLID ROLLER COMPARATIVE STRESS DATA

As in the case of the hollow-ended roller, a set of solid rollers with crown #10 optimum variation were subjected to 18,000 pounds load and .003 inch/inch misalignment. The resulting "Footprints", entry 7, Table IV, were constructed, Figures 73 and 74, and an incremental load evaluation was performed on them. The results (Table VIII) show that the resultant loads supported by each roller add up in excess of the known applied load by 5.4%, or 986 pounds. As before, the apparent area may be adjusted in both "Footprints" to yield areas that precisely account for the 18,000 pound load. It is interesting to note that the load supported by the heaviest loaded solid roller is 1091 pounds more than that carrier by the respective hollow-ended roller. This substantial difference is the result of hollow-rim flexibility. Not only does the OD elastically deform, but the rim deflects, allowing the second roller in the set to pick up a greater percentage of the total load. The added load, of course, increases the stresses in the case of the solid roller. A unit loading curve may be constructed (Figure 73) showing the maximum unit loading to be far greater than that found in the hollow-ended type (19,100 versus 15,200 psi). The subsurface shear stress distribution existing in the solid roller was determined using the classical approach of Thomas and Hoersch.³ The stress solutions determined by a computer program read out the results in curve form (Figures 75 and 76).

The stress gird is the same as employed in the hollow-ended roller analysis for Hertzian contact stress determination. Inspection of all such J plane stress distributions shows plane J7 to exhibit the maximum subsurface shear stress, or 120,000 psi. Comparing this stress value to that existing in the respective hollow-ended roller, or 102,000 psi (Figure 77), it is evident that the hollow-ended roller has a great advantage stress-wise over a solid roller in this particular application.

CROWN VERIFICATION

The previous investigation and subsequent finite element analysis have so far established the proper hollow-ended roller bore to be used in conjunction with the optimum solid roller crown selected for use under less severe misalignment conditions (.0005 inch/inch) than the hollow-ended roller is expected to endure. This solid roller crown (#10) is not most advantageous to use at .003 inch/inch misalignment when considering the hollow-ended roller and is even worse for a solid roller at this misalignment condition as the bluntness at the end of contact on the best hollow-ended roller "Footprint" testifies (Figure 34). A more liberal crown drop, while maintaining approximately the same flat length, is necessary. Crown #11 shows the required dimensions (Table I). Rollers with the desired bore configuration (#3) were crowned to this specification and subjected to the desired load and misalignment (18,000 pounds and .003 inch/inch) with the results displayed in Figure 78. Inspection of the "Footprints" shows that the shape of both contact areas is pointed at the ends, which is the anticipated effect. Measurement of the maximum 2b width and subsequent correction for etch thickness (etch correction curve, Figure 79) show the actual width to be less than that determined for crown #10 "Footprint" (Table IV). This means that the maximum stress level will be lower than the best established so far, or 102,000 psi. "Footprints" were also made at 12,000 and 8000 pounds load (Figure 78), showing contact for all rollers in both sets as well as pointed ends of contact at .003 inch/inch misalignment. In addition, a "Footprint" was created at 12,000 pounds load .0015 inch/inch misalignment, Figure 78, which could be representative of an actual operating condition.

CONCLUSIONS

The following sequential descriptions, with appropriate conclusions, logically include all conclusions reached as a result of the various investigations in this development program.

1. The conclusion resulting from a "Footprint" study to determine the influence of roller crowning on solid roller load distributions for 18,000 pounds applied load per roller set and .0005 inch/inch misalignment is as follows:

The solid roller with crown geometry #10, Table I, produces the best "Footprint" considering end of contact shape.

2. Crown #10 was applied to various hollow-ended roller configurations which were then subjected to an 18,000 pound load and .003 inch/inch misalignment. The following conclusion was made with respect to bore shape selection:

The roller with bore configuration 3 was responsible for the best "Footprint", considering both end of contact shape and maximum contact width.

3. A "Footprint" analysis was performed on this contact area yielding the load distribution on the roller. These results provided input data for a comprehensive stress analysis on the hollow-ended roller rim. Specific conclusions regarding the stress state existing in the rim of the most heavily loaded roller in the tandem set are as follows:

- a. The maximum shear stress located just inside the bore surface is 40,000 psi and is well within acceptable limits.
- b. The maximum subsurface shear stress (resulting from combining the Hertzian contact stresses with those induced from rim deflection) found near the surface of the roller, directly under the plane of the load, is 102,000 psi and is a reasonable static stress level.
- c. As the significant shear stress at the outside diameter is substantially greater than that found in the bore, and assuming a good bore finish, the failure

mode in the hollow-ended roller will be conventional outside diameter fatigue spalling, which is normal and predictable.

4. Tailored crowning was considered for the hollow-ended roller for operating conditions of 18,000 pounds load per roller set and .003 inch/inch misalignment. Conclusions from this investigation are:
 - a. The best bore/crown relationship for the above specific conditions is bore 3 (selected previously) with crown #11 (Table I).
 - b. A reduction in the previously established maximum shear stress level (102,000 psi) is possible employing the above bore/crown combination.
 - c. "Footprints" created at 12,000 pounds and 8000 pounds with .003 inch/inch misalignment also exhibit satisfactory contact shapes.
5. Comparing a hollow-ended roller "Footprint" set to a respective solid roller set for the same application (18,000 pounds and .003 inch/inch), the following conclusions apply:
 - a. The applied load is shared more favorably by the two hollow-ended rollers (heaviest loaded solid roller supports 16,029 pounds while the respective hollow-ended roller supports 14,938 pounds).
 - b. A 20% decrease in the subsurface maximum shear stress level found when comparing a hollow-ended roller to a conventional solid roller results in a significantly greater L_{10} fatigue life for the hollow-ended type.
 - c. The maximum Hertzian contact stress of the hollow-ended roller is 350,000 psi compared to a stress of approximately 400,000 psi for the solid roller configuration under identical load conditions.
 - d. Life comparison based upon these conclusions for various HLH planet bearing configurations is shown in Figure 80. These results show that the hollow-ended cylindrical roller bearing configuration provides the best life performance under the expected HLH operating conditions.

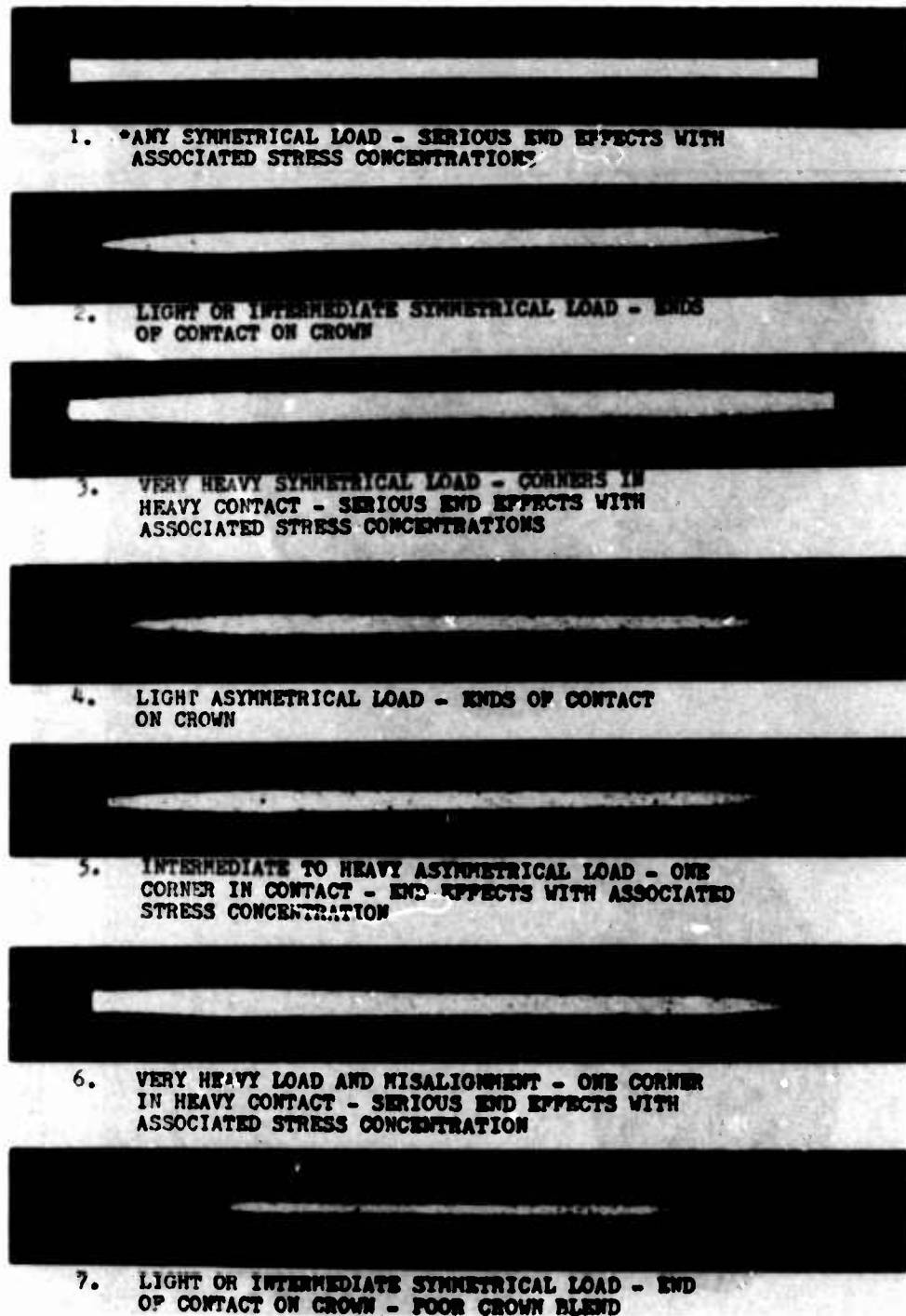
RECOMMENDATIONS

Although the data generated in this development program is of a conclusive nature as far as design feasibility is concerned with the assumed operating misalignment, it does not exhibit whether the proposed bearing which includes hollow-ended rollers will function with maximum benefit under the actual misalignment conditions which may be more or less severe than anticipated. In this application, because of the complicated nature of deflections involved in components other than bearings, it is very difficult to analytically determine the precise deflection expected to exist at the bearing locations. If the misalignments are found to be not as expected, the roller geometry may need further refinement to result in a more favorable load distribution, hence increasing reliability and life. The basic "Footprint" method may be extended to include evaluation of whole bearings.⁴

Prototype bearings with etched races could be carefully placed into position in the transmission with the expected peak load applied statically. The load distribution on the etched races and, in particular, the "Footprint" found at the most heavily loaded roller position, may be evaluated to reveal the maximum deflection existing at that bearing location. If different than specified initially (.003 inch/inch) the roller crown geometry should be changed to obtain the best static load distribution possible. Finally, to determine the effects of any extraneous dynamic effects a fatigue test evaluation employing the subject bearing will be performed. Such a dynamic test may indicate that minor refinements to the roller geometry may be advantageous.

LITERATURE CITED

1. Goodelle, R.A., Derner, W.J., and Root, L.E.; A PRACTICAL METHOD FOR DETERMINING CONTACT STRESSES IN ELASTICALLY LOADED LINE CONTACTS, ASLE Transactions, Vol. 13, 1970, pp. 269-277.
2. Derner, W.J., Goodelle, R.A., Root, L.E., and Rung, R.; THE HOLLOW-ENDED ROLLER - A SOLUTION FOR IMPROVING FATIGUE LIFE IN ASYMMETRICALLY LOADED CYLINDRICAL ROLLER BEARING, to be published in ASME Transactions, 1972.
3. Thomas, H.R., and Hoersch, V.A.; STRESSES DUE TO THE PRESSURE OF ONE ELASTIC SOLID UPON ANOTHER, University of Illinois, Engineering Experiment Station, Bulletin Number 212, July 1930, pp. 26-29.
4. Goodelle, R.A., Derner, W.J., and Root, L.E.; DETERMINATION OF STATIC LOAD DISTRIBUTIONS FROM ELASTIC CONTACTS IN ROLLING ELEMENT BEARINGS, ASLE Transactions, Vol. 14, 1971, pp. 275-291.



***Uncrowned Roller**

Figure 1. Contact Area Shapes (Footprints) Created by Various Loading Conditions on a Partially Crowned Cylindrical Roller.

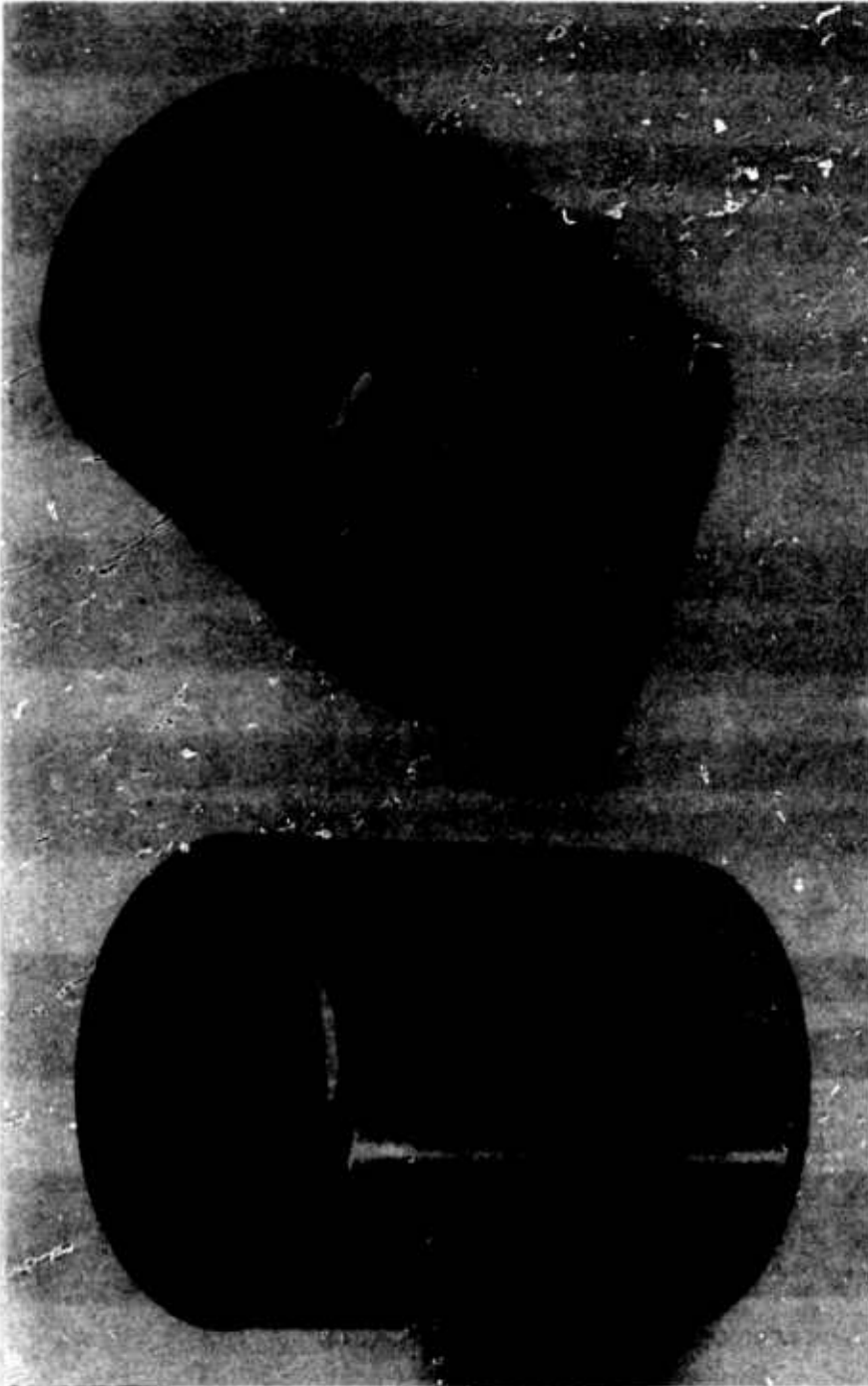
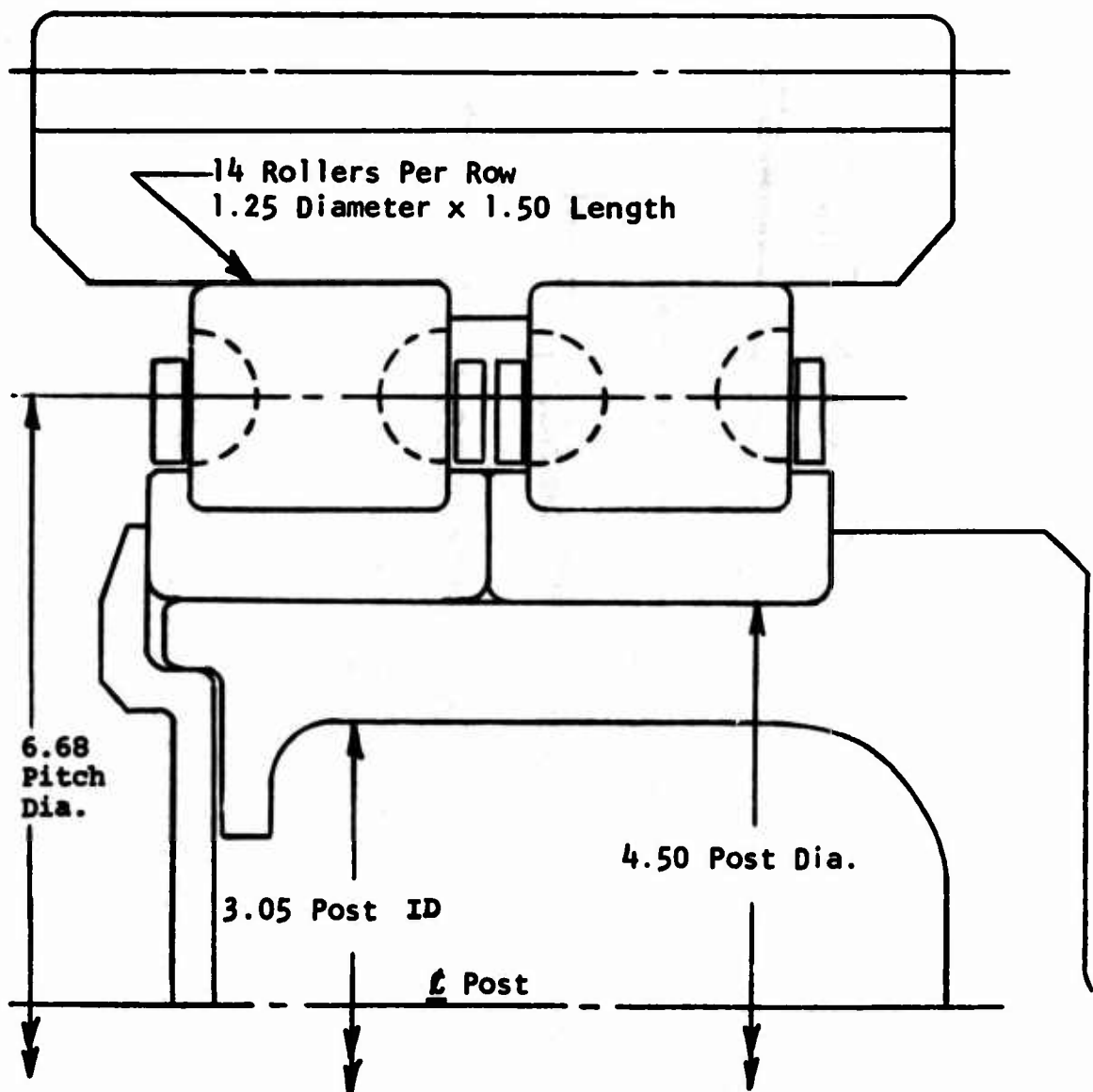


Figure 2a. Hollow-Ended Roller Design.



**Figure 2b. HLH Design Study - Planetary Bearing
(Second Stage Planet).**

ROLLER

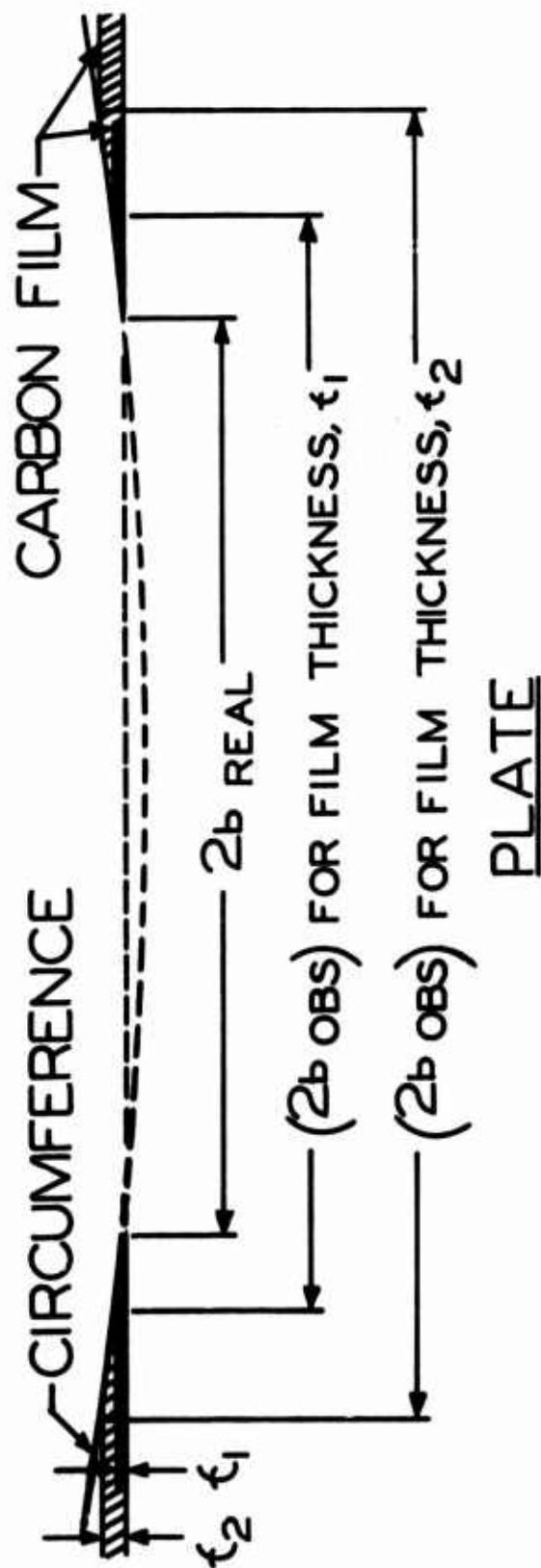


Figure 3. Elastic Contact Between Loaded Roller and Flat Plate Showing Influence of Etch Film Thickness on Observed Contact Width.

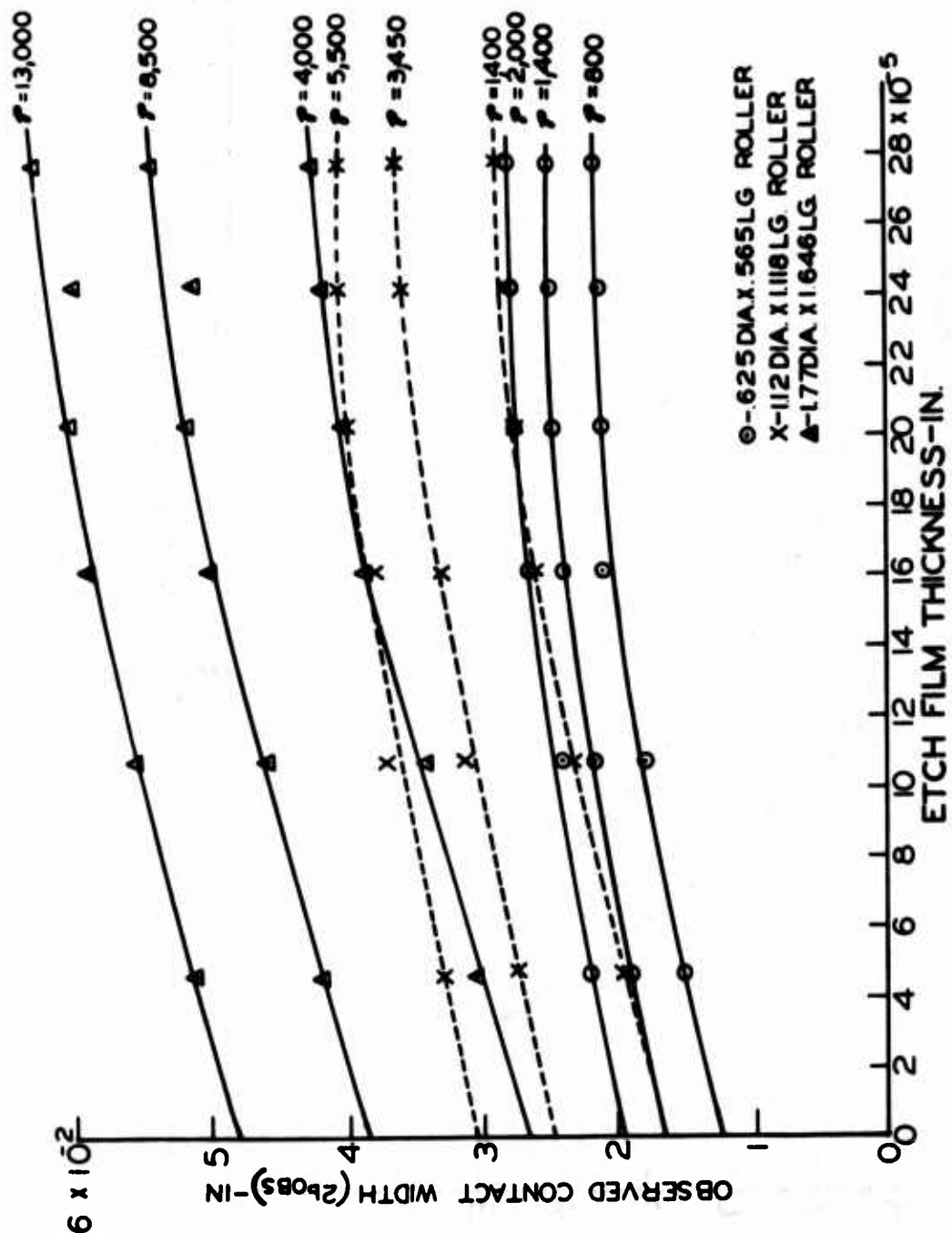


Figure 4. Influence of Film Thickness on Observed Contact Width (2b_{obs}) for Various Loads and Roller Diameters.

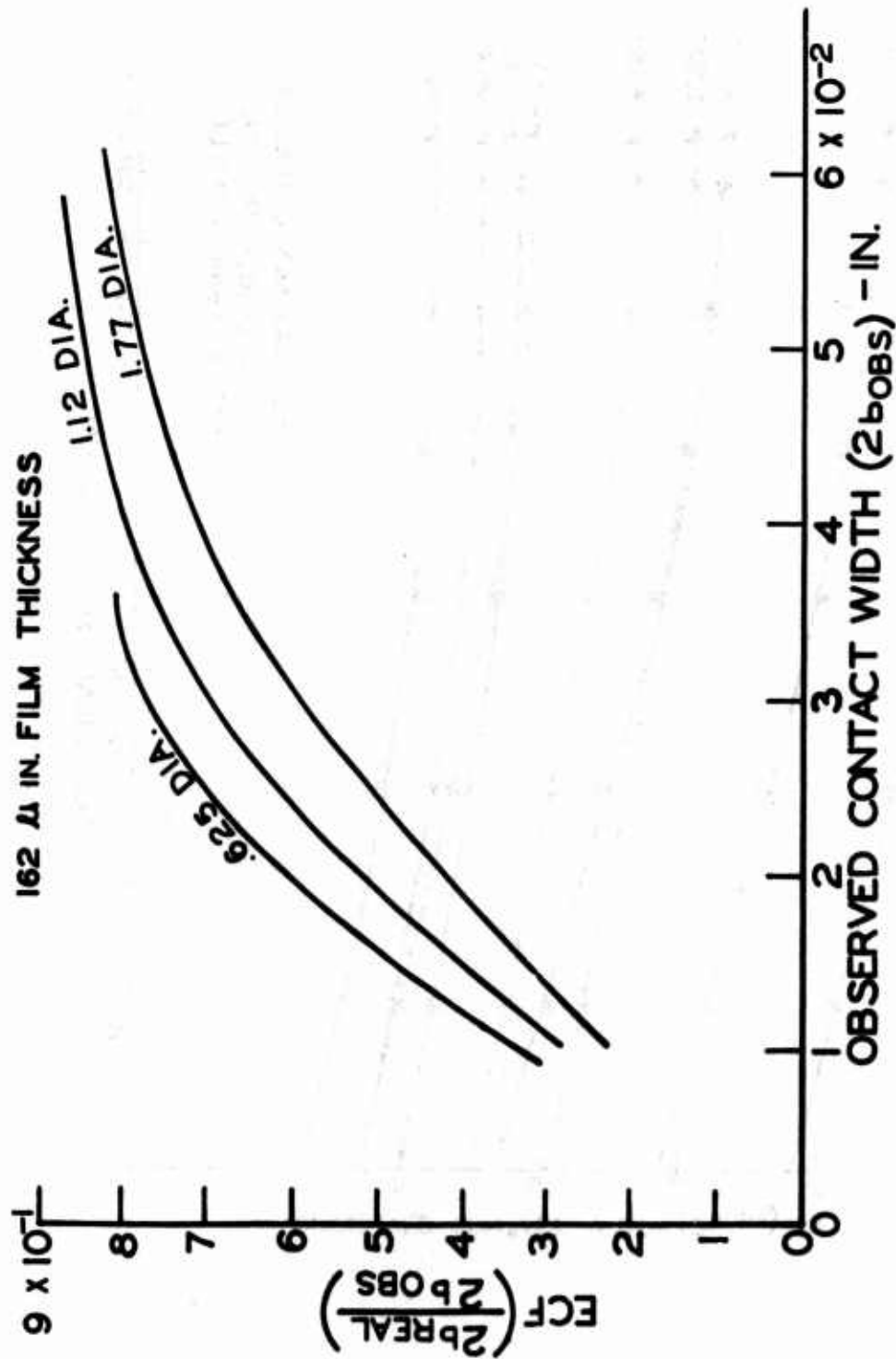


Figure 5. Etch Correction Factor as a Function of Observed Contact Width and Roller Diameter for a Constant Film Thickness.

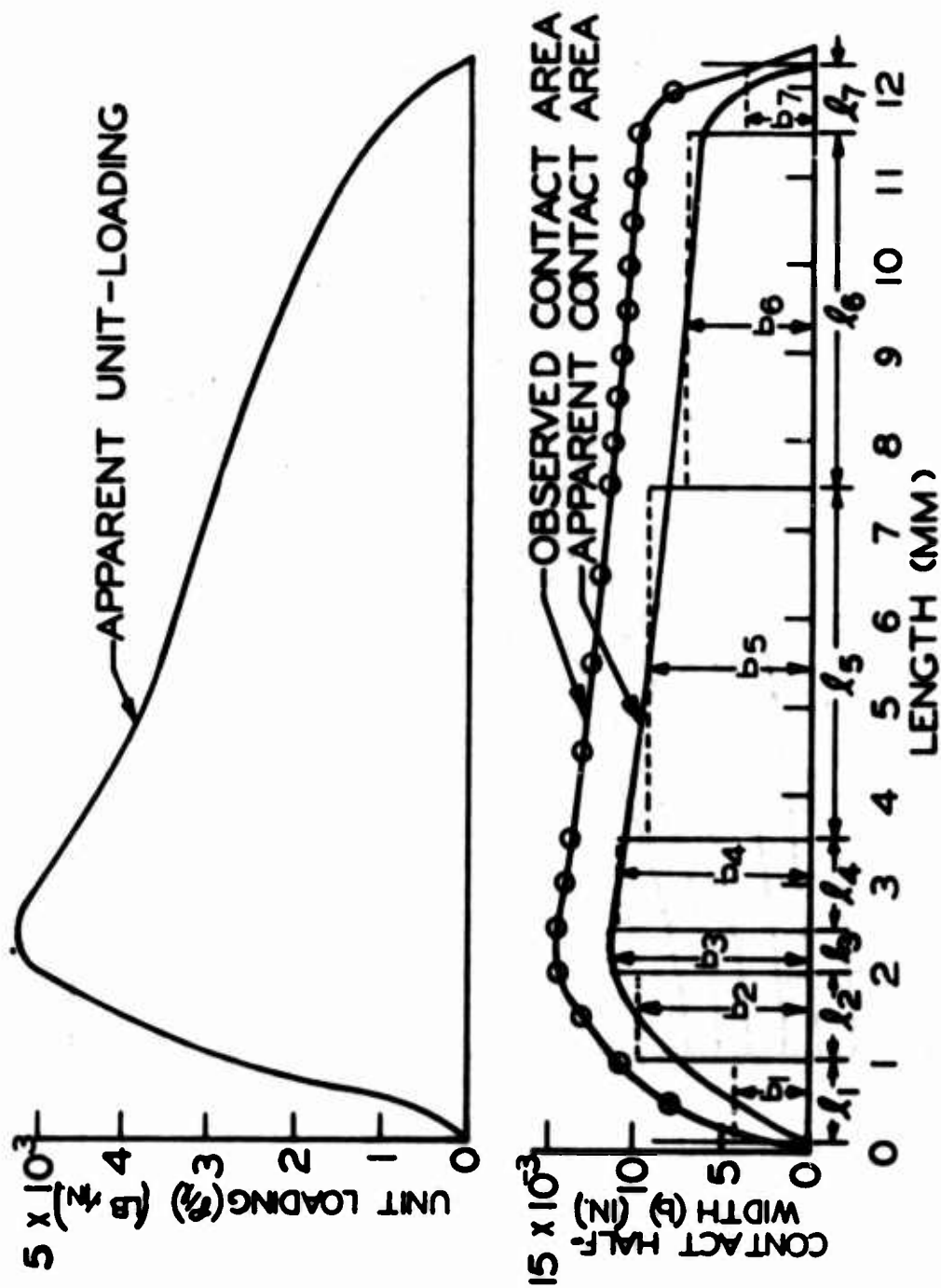


Figure 6. Example Graphical Layout and Resultant Stress Analysis of a Typical "Footprint".

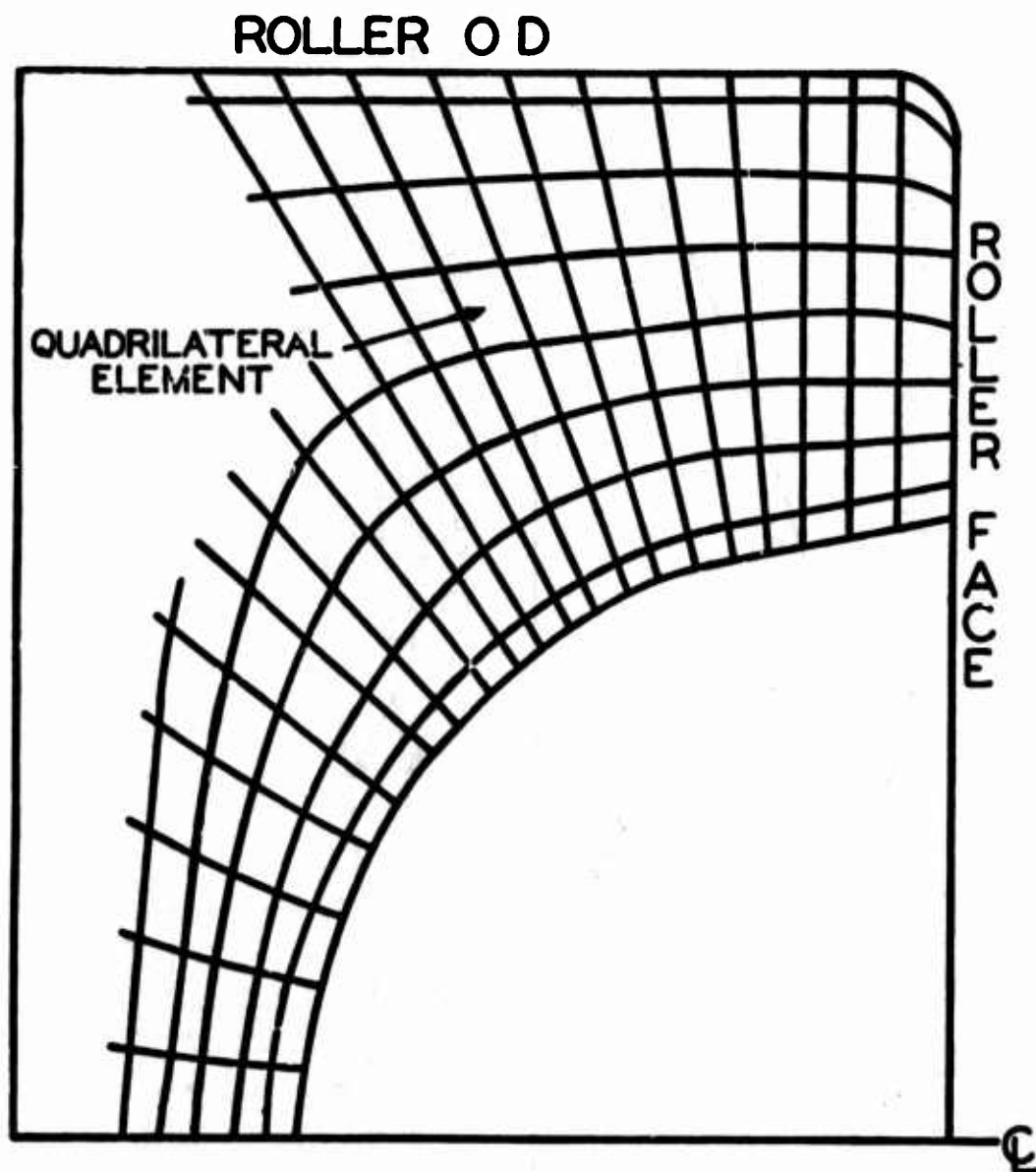
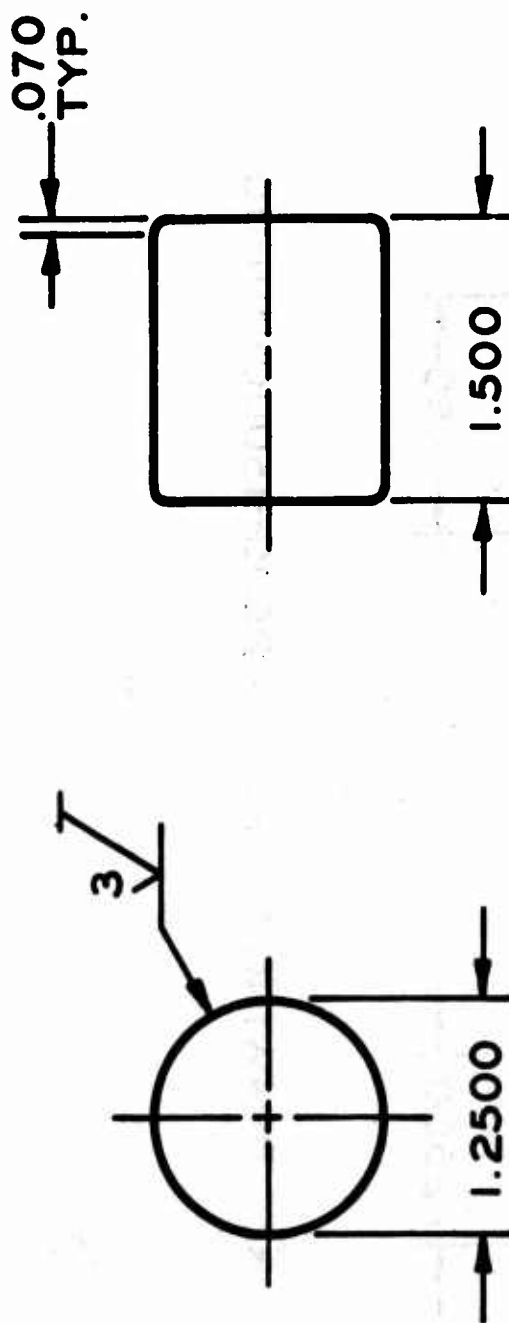
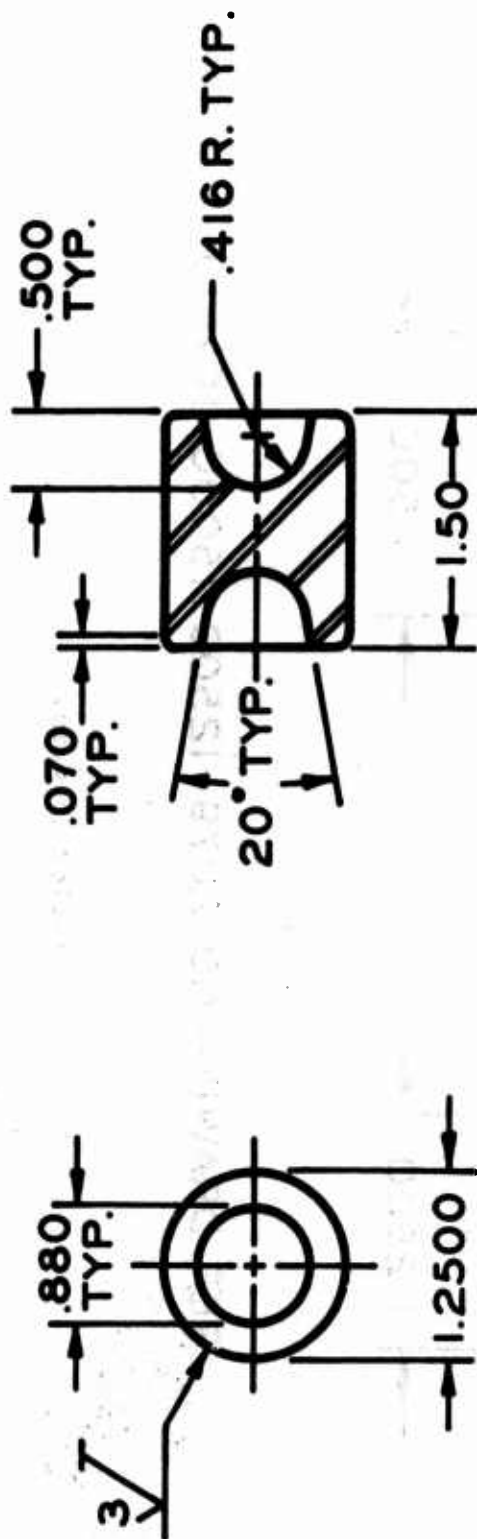


Figure 7. Finite Element Idealization for Rim Section of Hollow-Ended Roller (Example Grid).



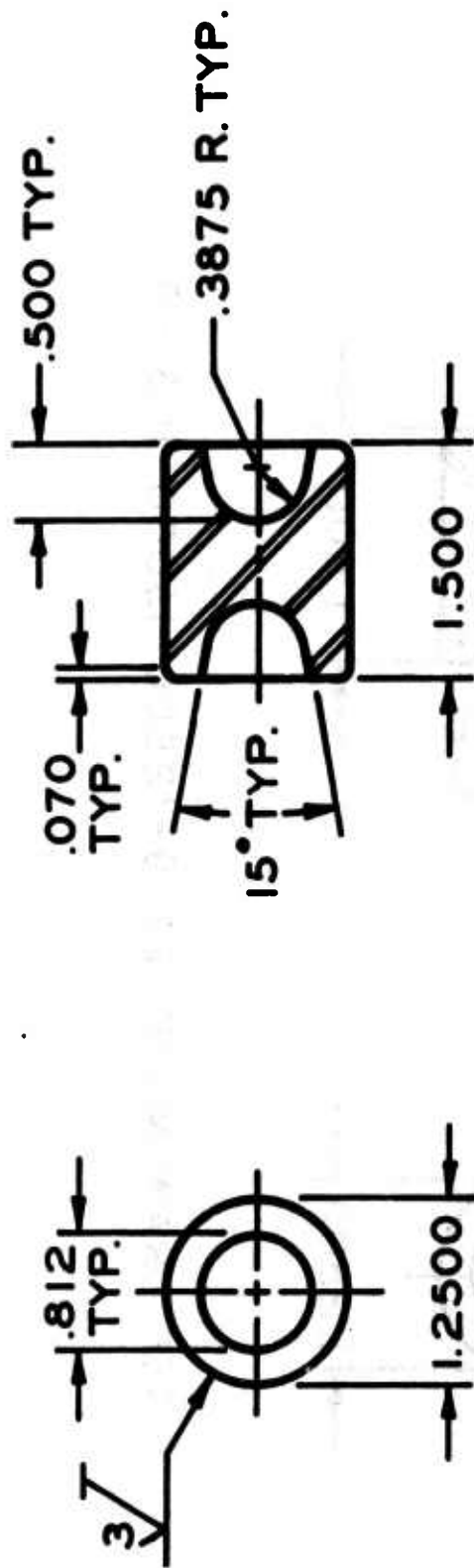
REF. DRAWING NO. 2079-12500-15000-107-10

Figure 8. Solid Roller Design.



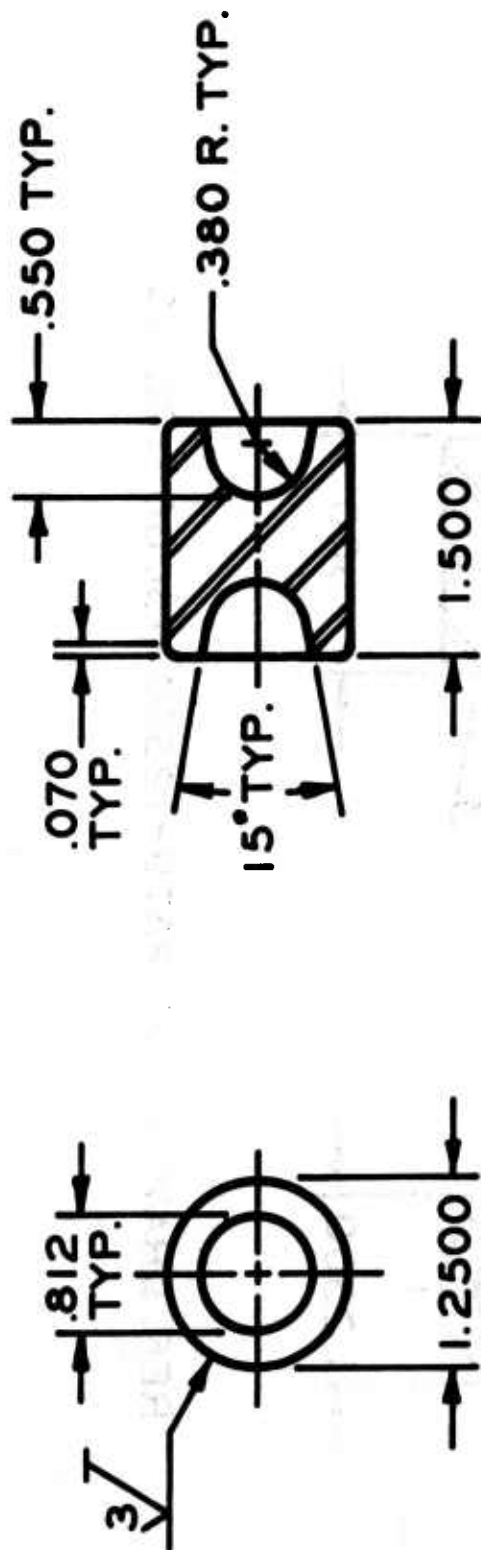
REF. DRAWING NO. 2579-12500-15000-101-10

Figure 9. Hollow-Ended Roller Design - Bore No. 1.



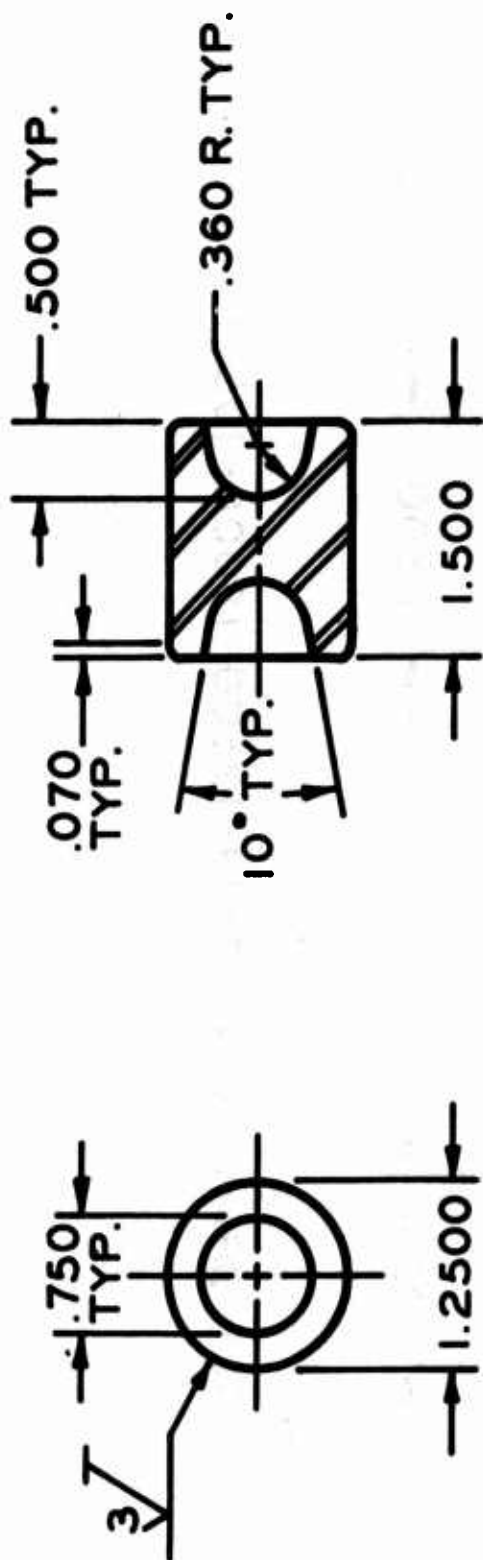
REF. DRAWING NO. 2579-12500-15000-102-10

Figure 10. Hollow-Ended Roller Design - Bore No. 2.



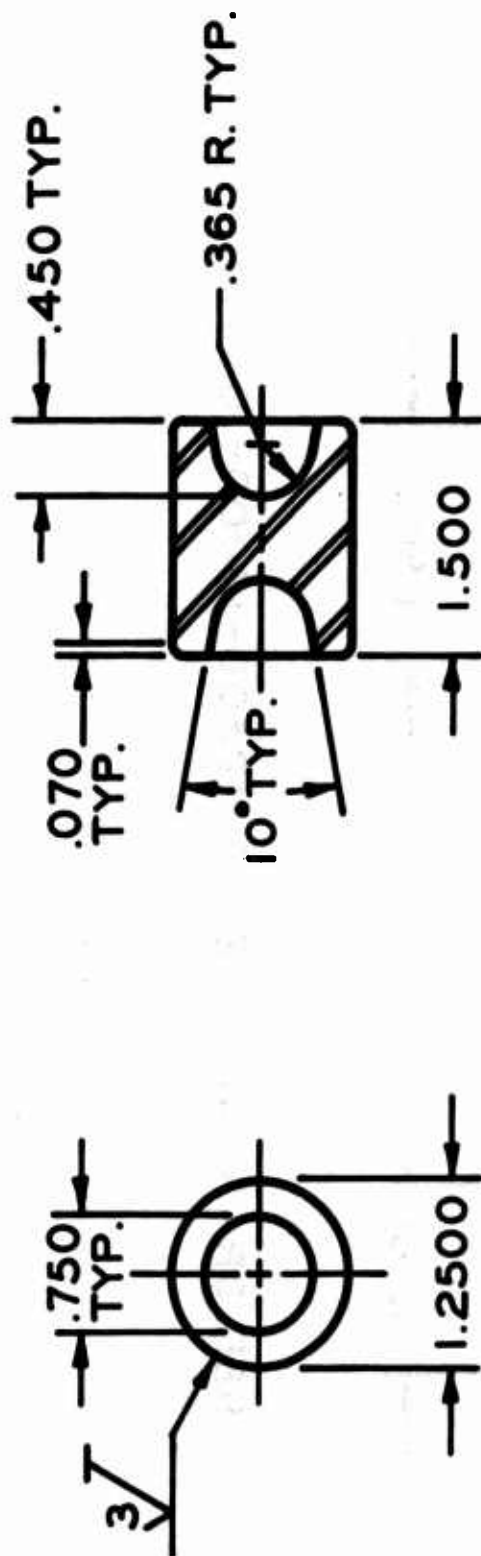
REF. DRAWING NO. 2579-12500-15000-103-10

Figure 11. Hollow-Ended Roller Design - Bore No. 3.



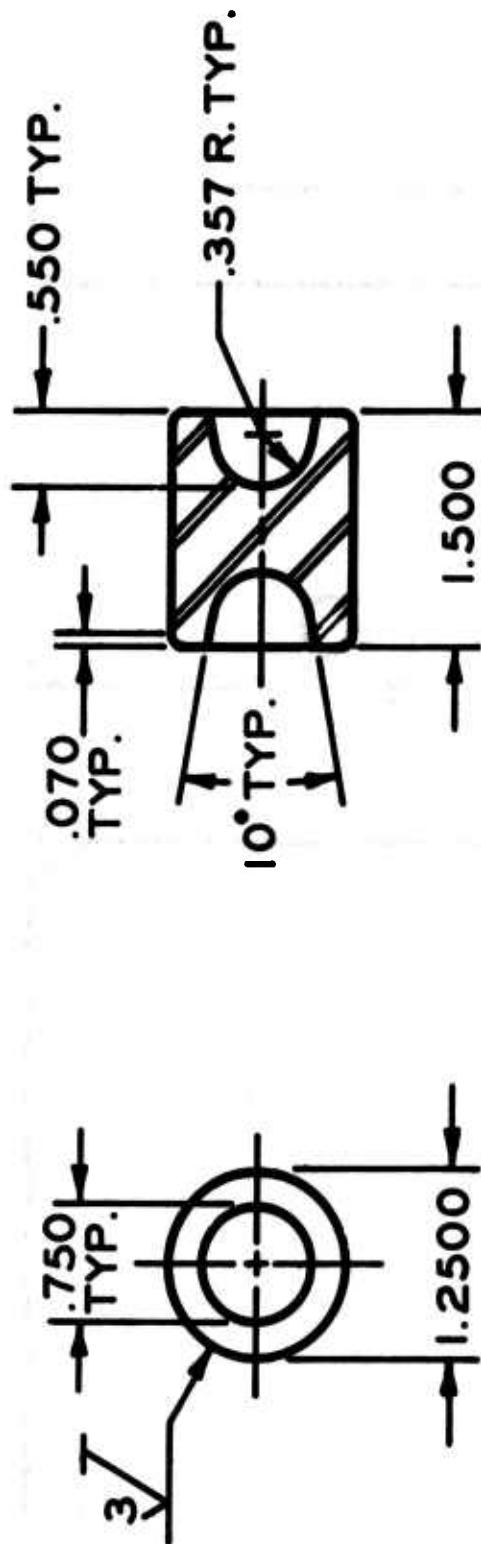
REF. DRAWING NO. 2579-12500-15000-104-10

Figure 12. Hollow-Ended Roller, Design - Bore No. 4.



REF. DRAWING NO. 2579-12500-15000-105-10

Figure 13. Hollow-Ended Roller Design - Bore No. 5.



REF. DRAWING NO. 2579-12500-15000-106-10

Figure 14. Hollow-Ended Roller Design - Bore No. 6.

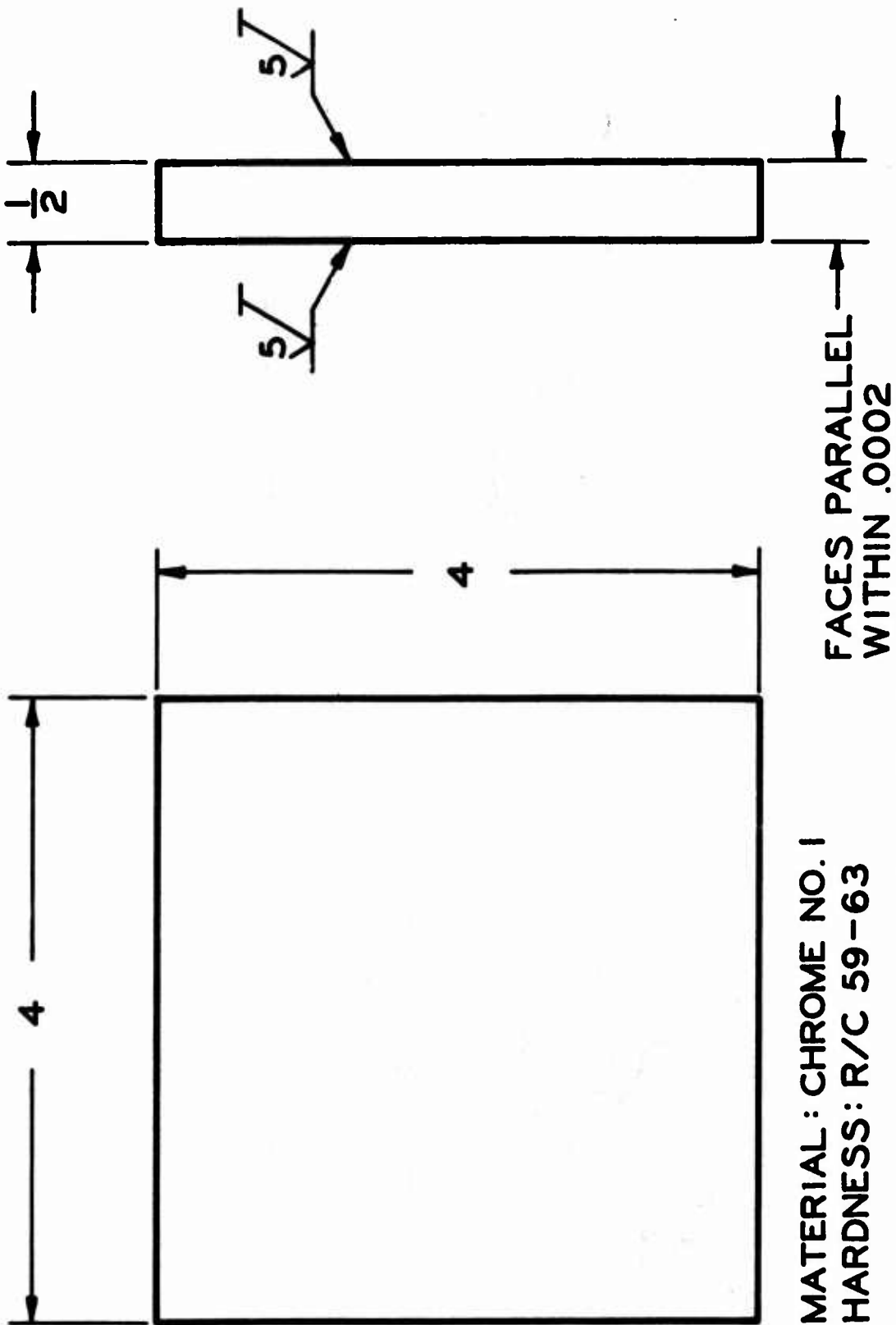


Figure 15. Test Plate.



43

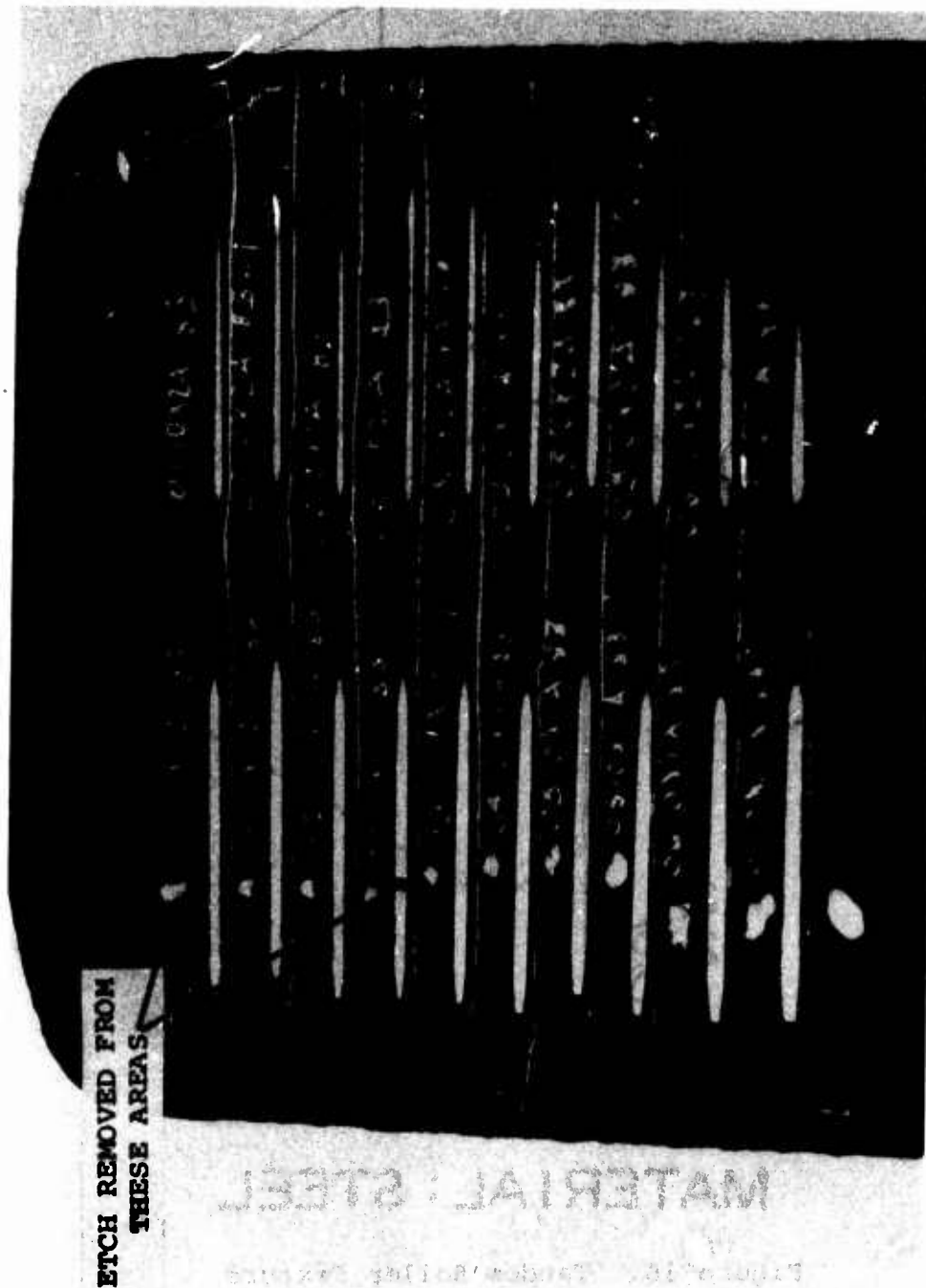


Figure 17. Test Plate Showing Areas Used in Determination of Etch Film Thickness Adjacent to Footprints.

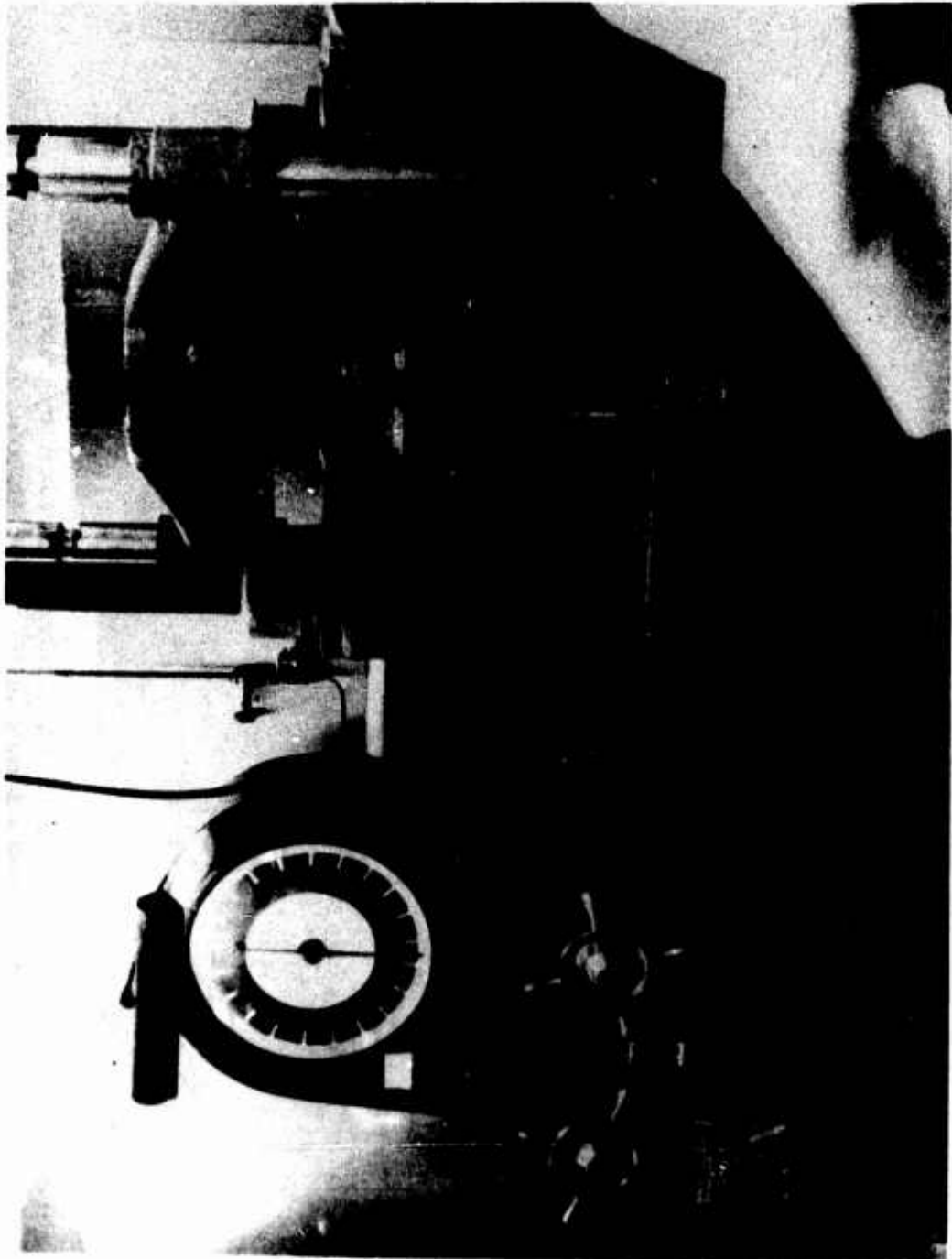


Figure 18. Photograph of Baldwin-Southwark Hydraulic Loading Device.

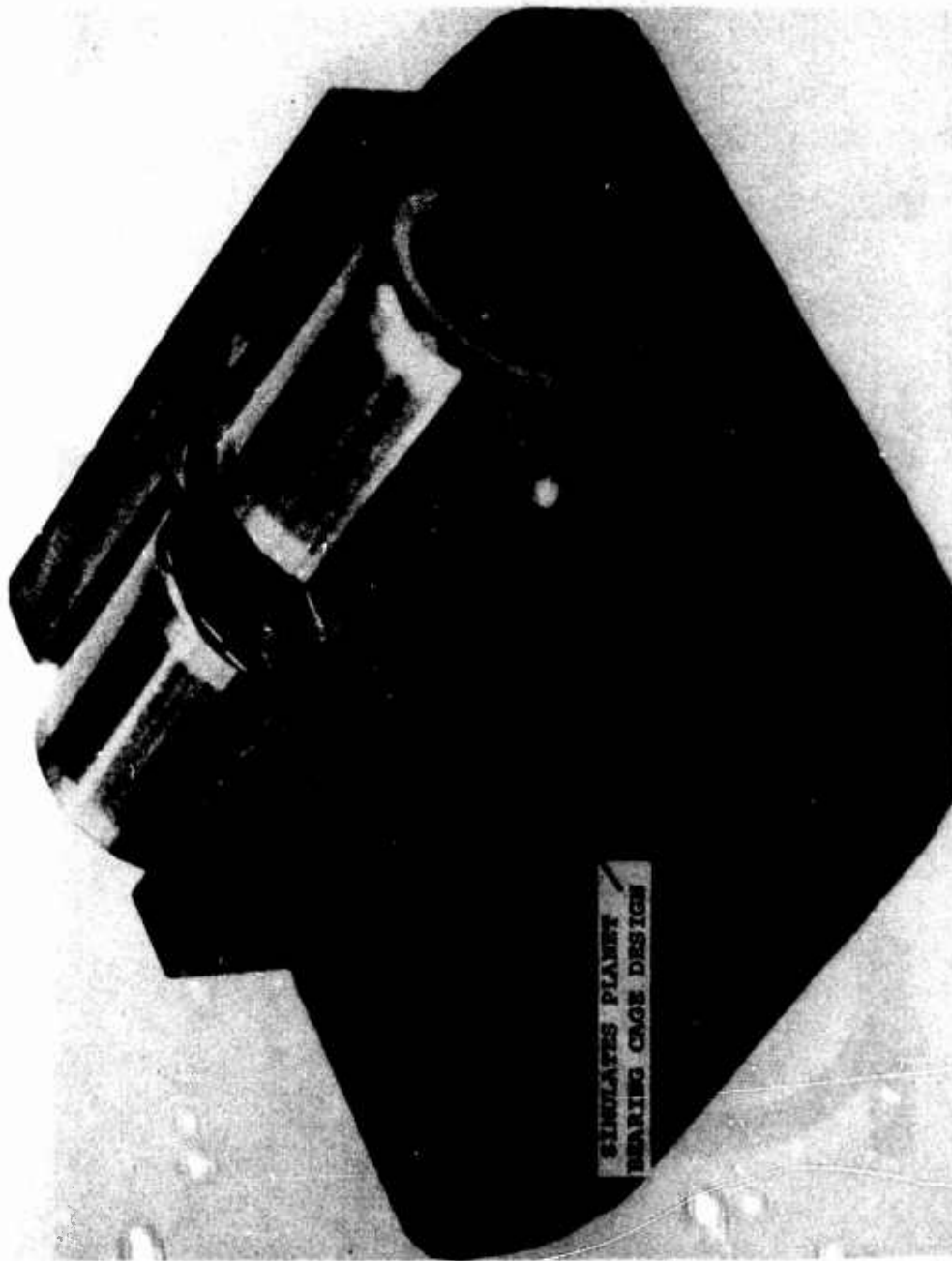


Figure 19. Test Rollers Held In Tandem Position by Fixture.

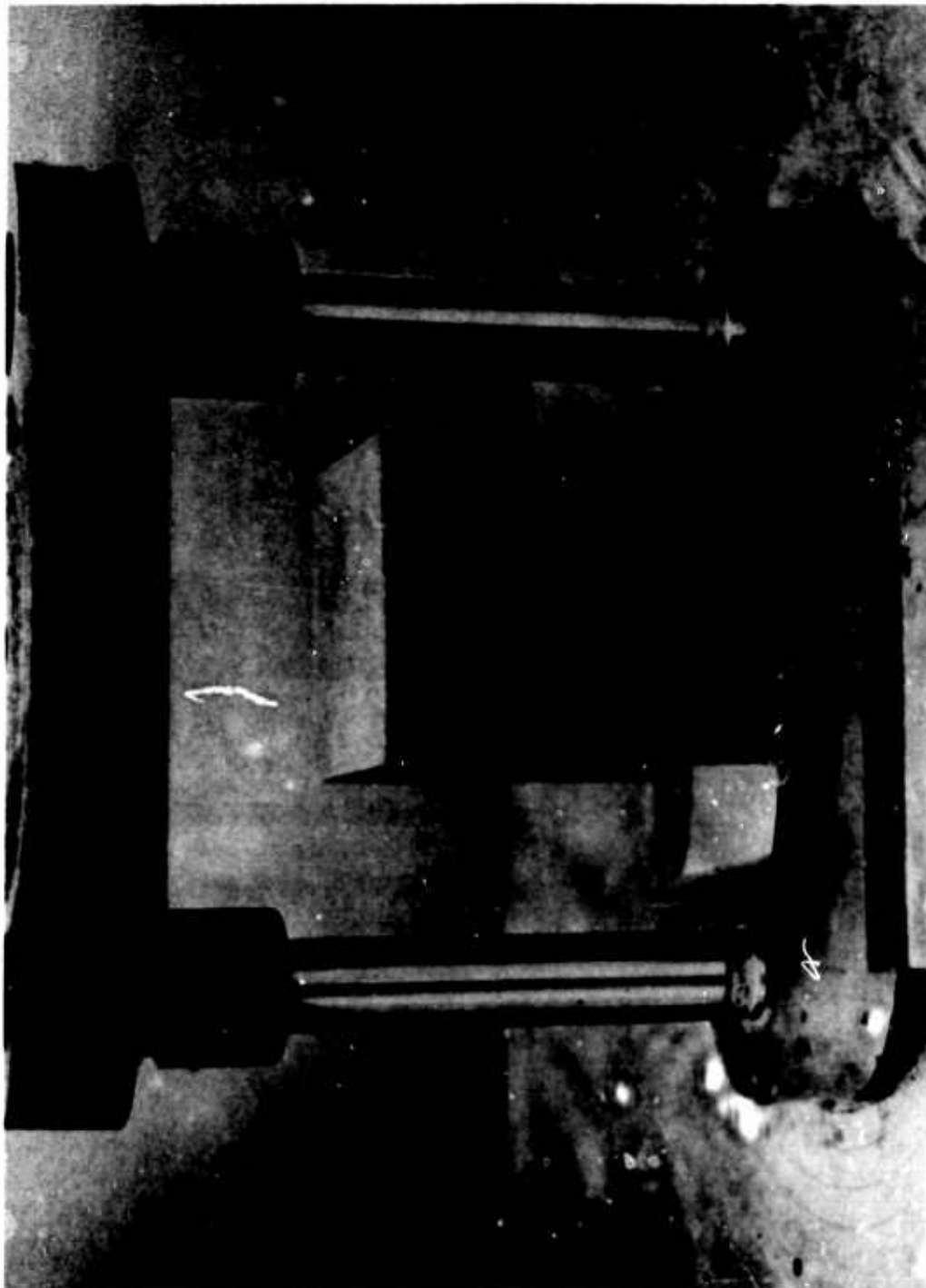


Figure 20. Inducing Misalignment in Test Rig by Shimming.

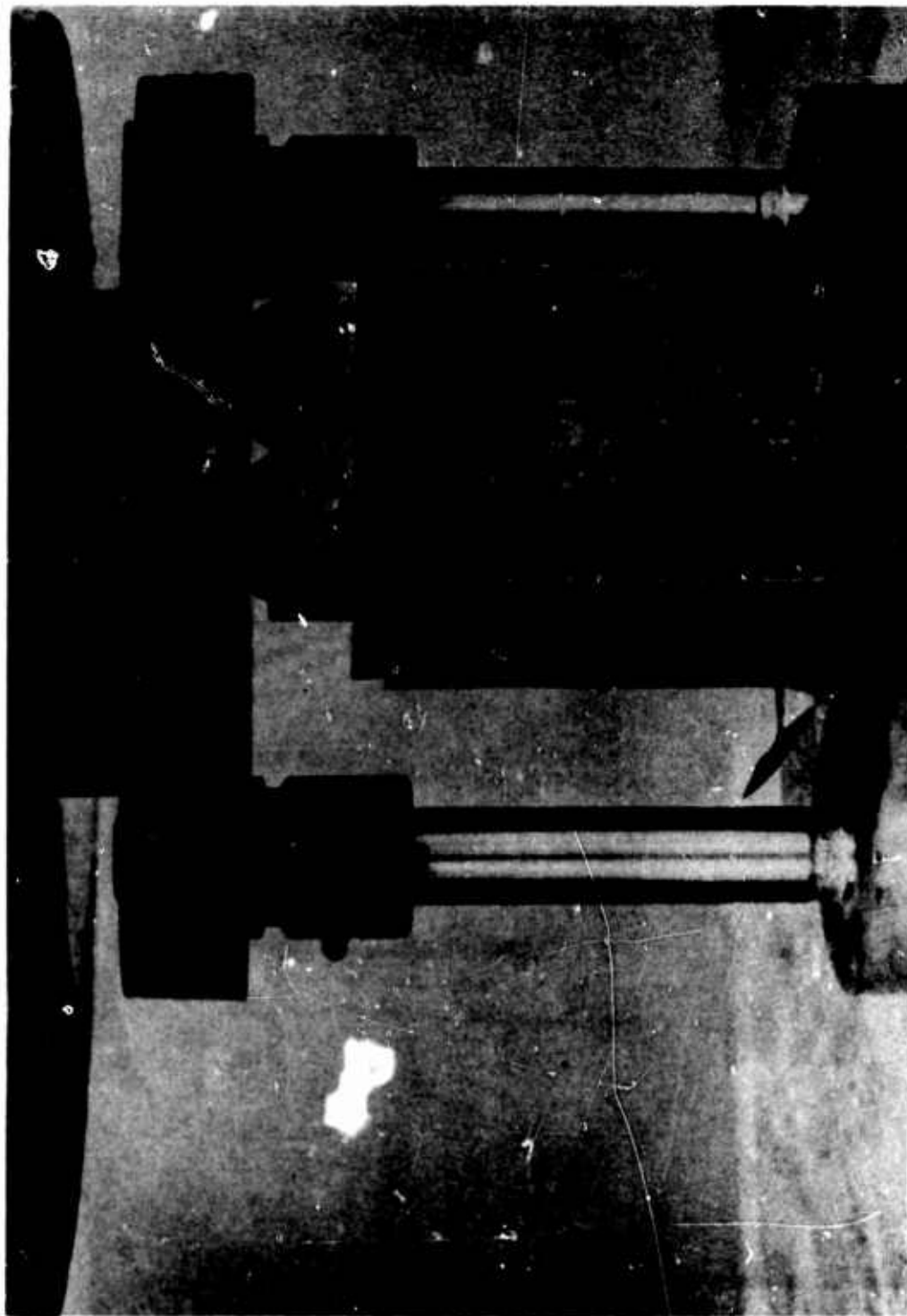


Figure 21. Method of Applying Load to Test Rollers.

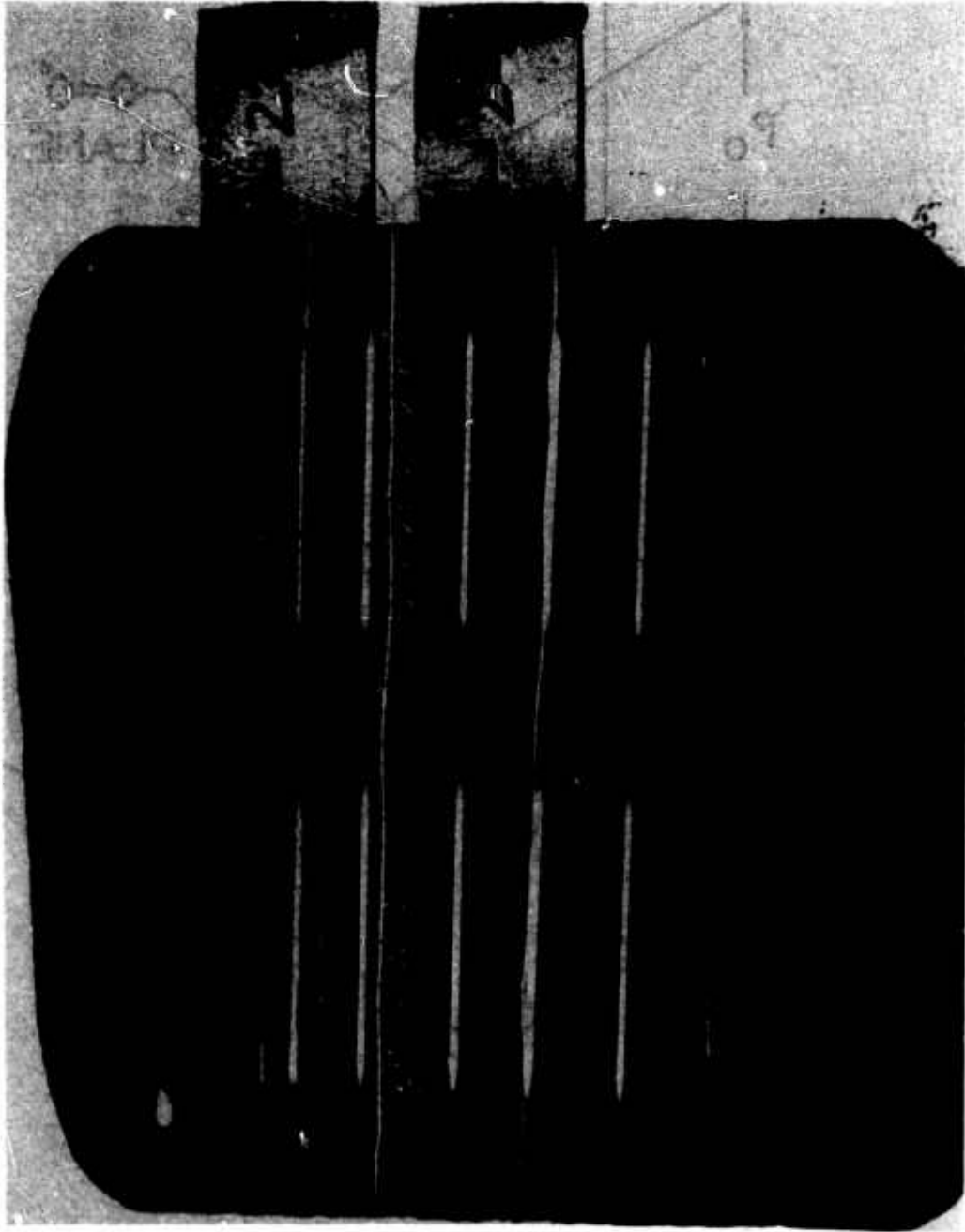


Figure 22. Example of Recorded Contact Area on Actual Test Plate.

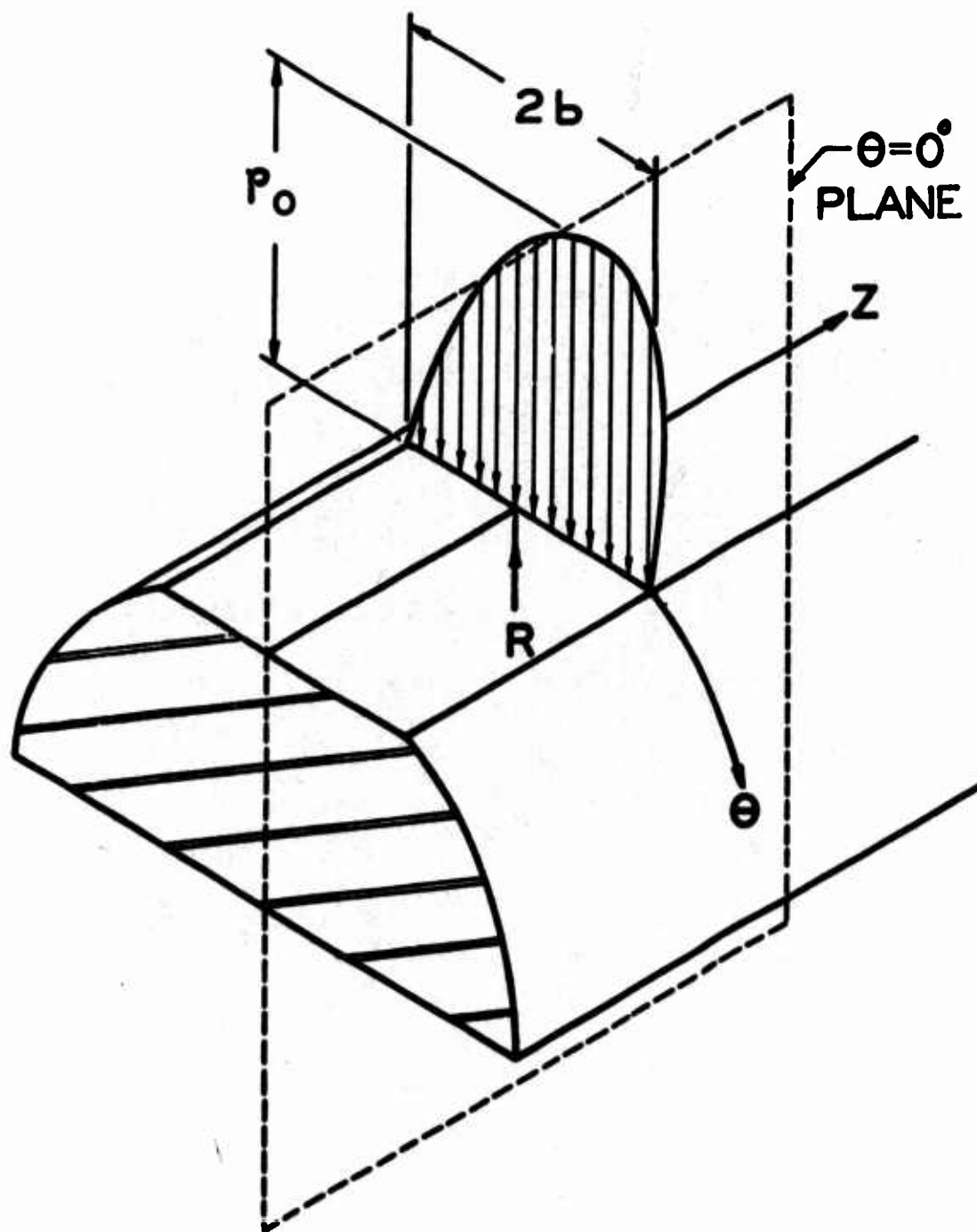


Figure 23. Roller Coordinate System.

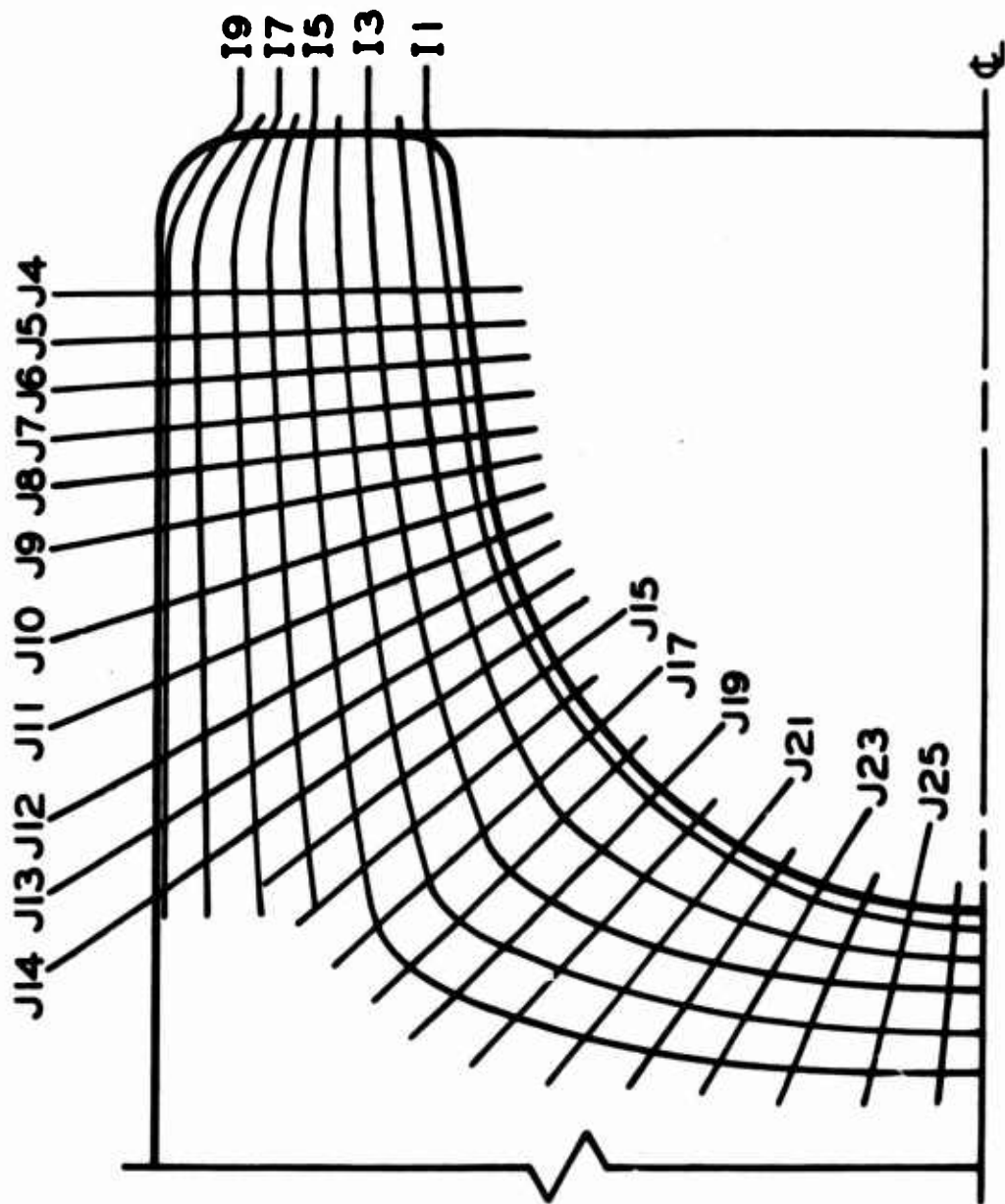


Figure 24. Stress Planes (J and I) With Stresses (σ_H^*) Computed at Intersections.

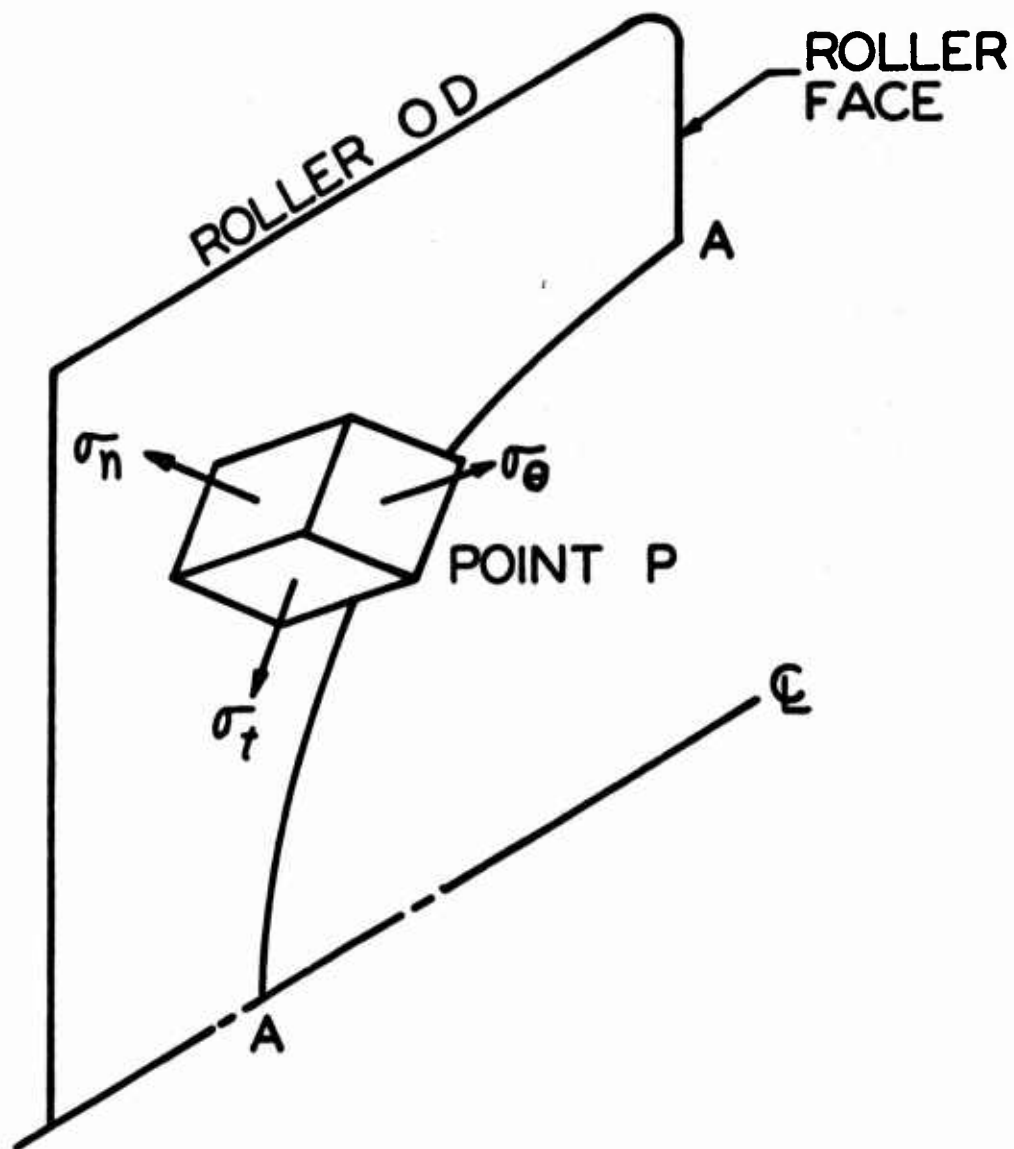


Figure 25. Bore Stress Orientation.

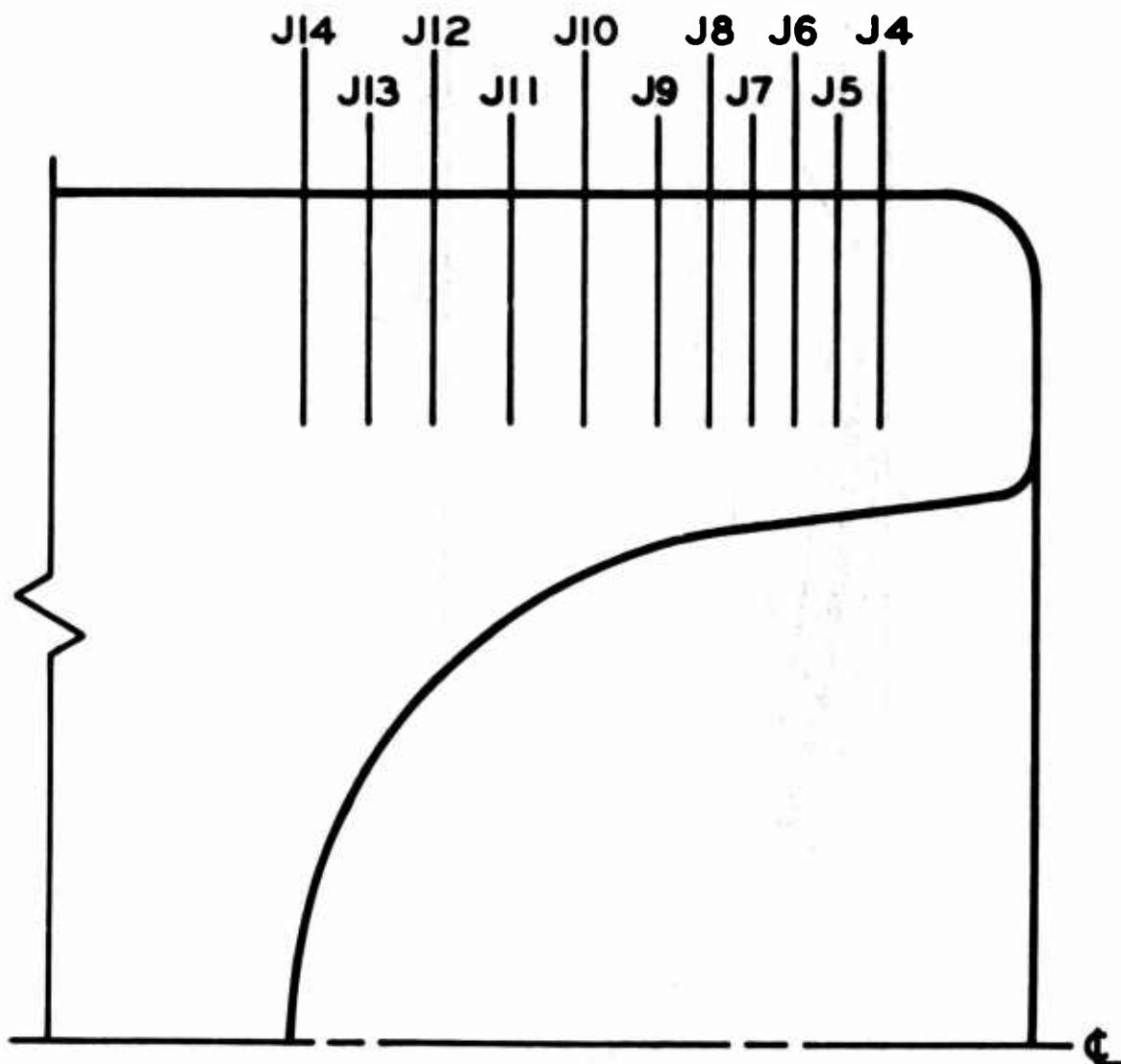


Figure 26. J Stress Planes for Stress Distribution of Hertzian Contact Stresses (σ_s).

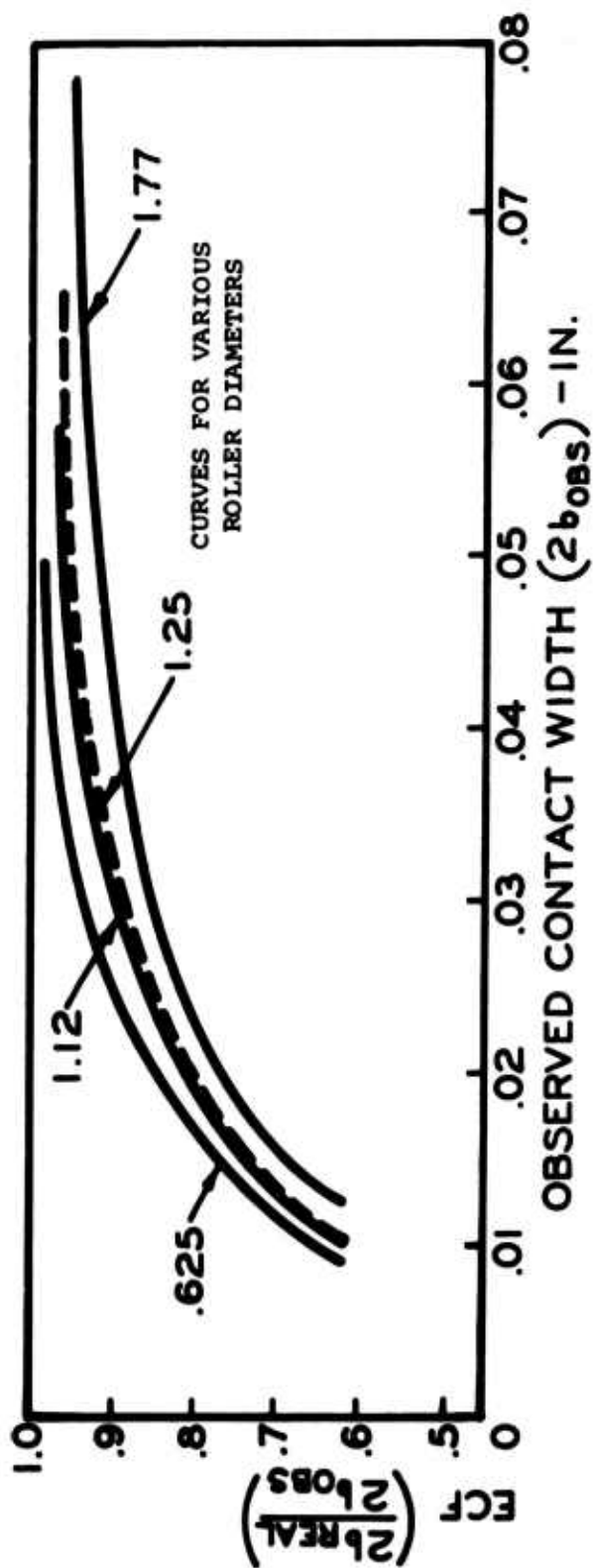


Figure 27. Etch Correction Factors for a Film Thickness of 57μ Inch.

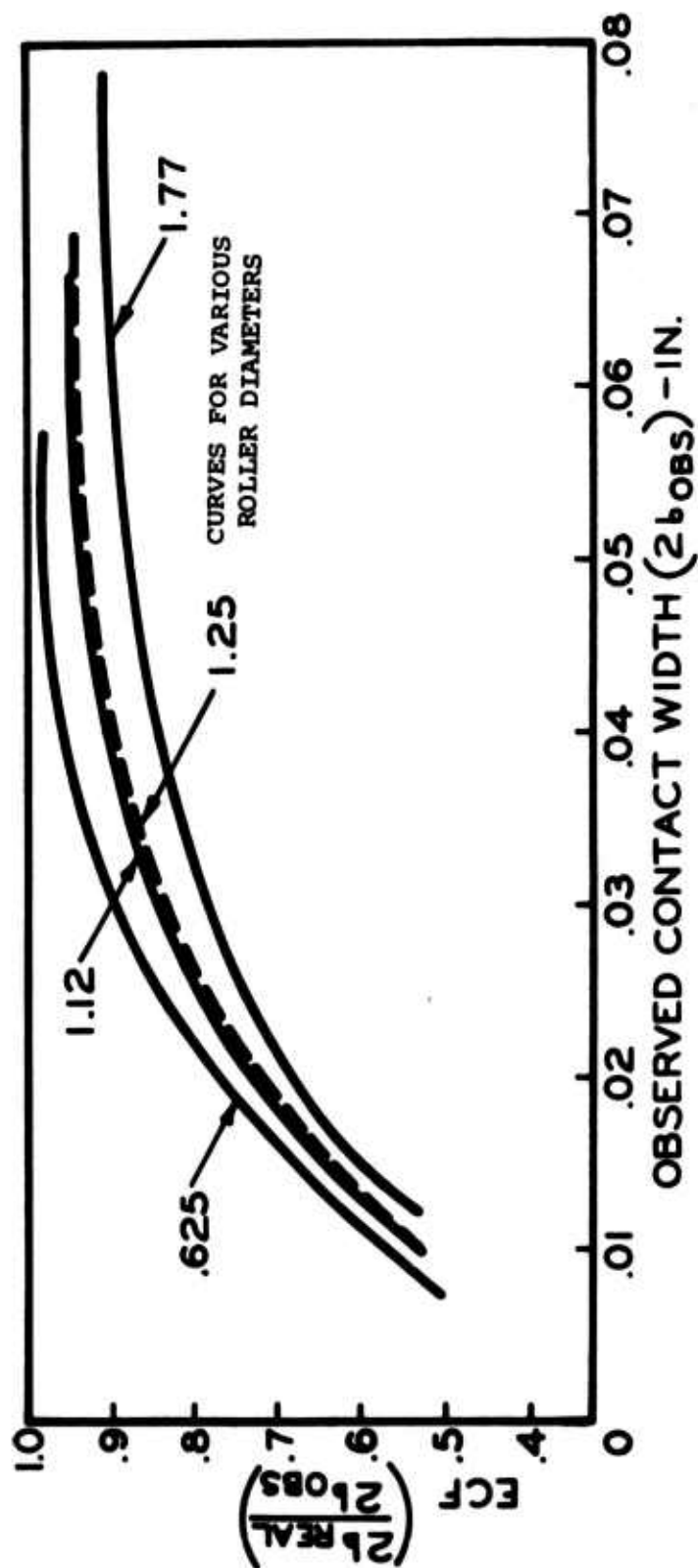


Figure 28. Etch Correction Factors for a Film Thickness of 86 μ Inch.

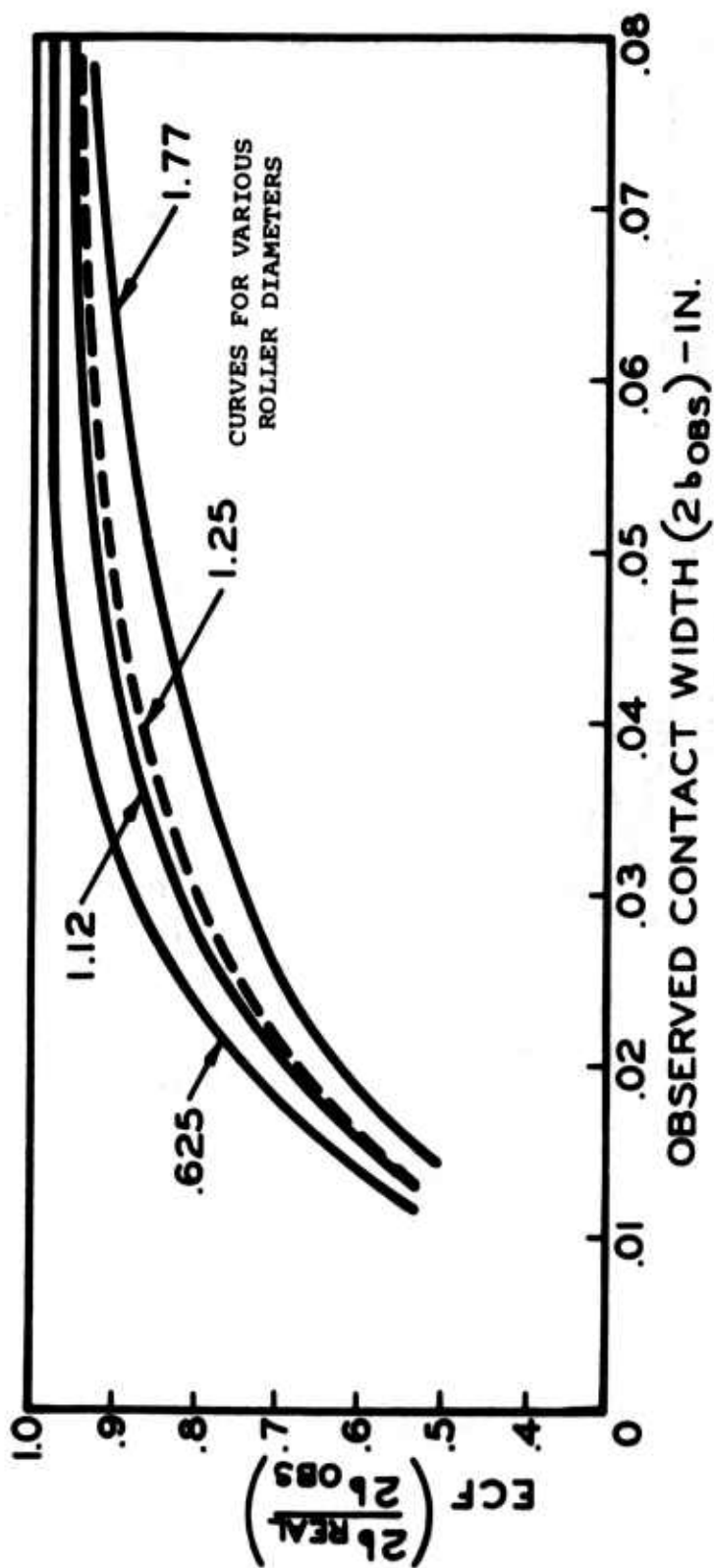
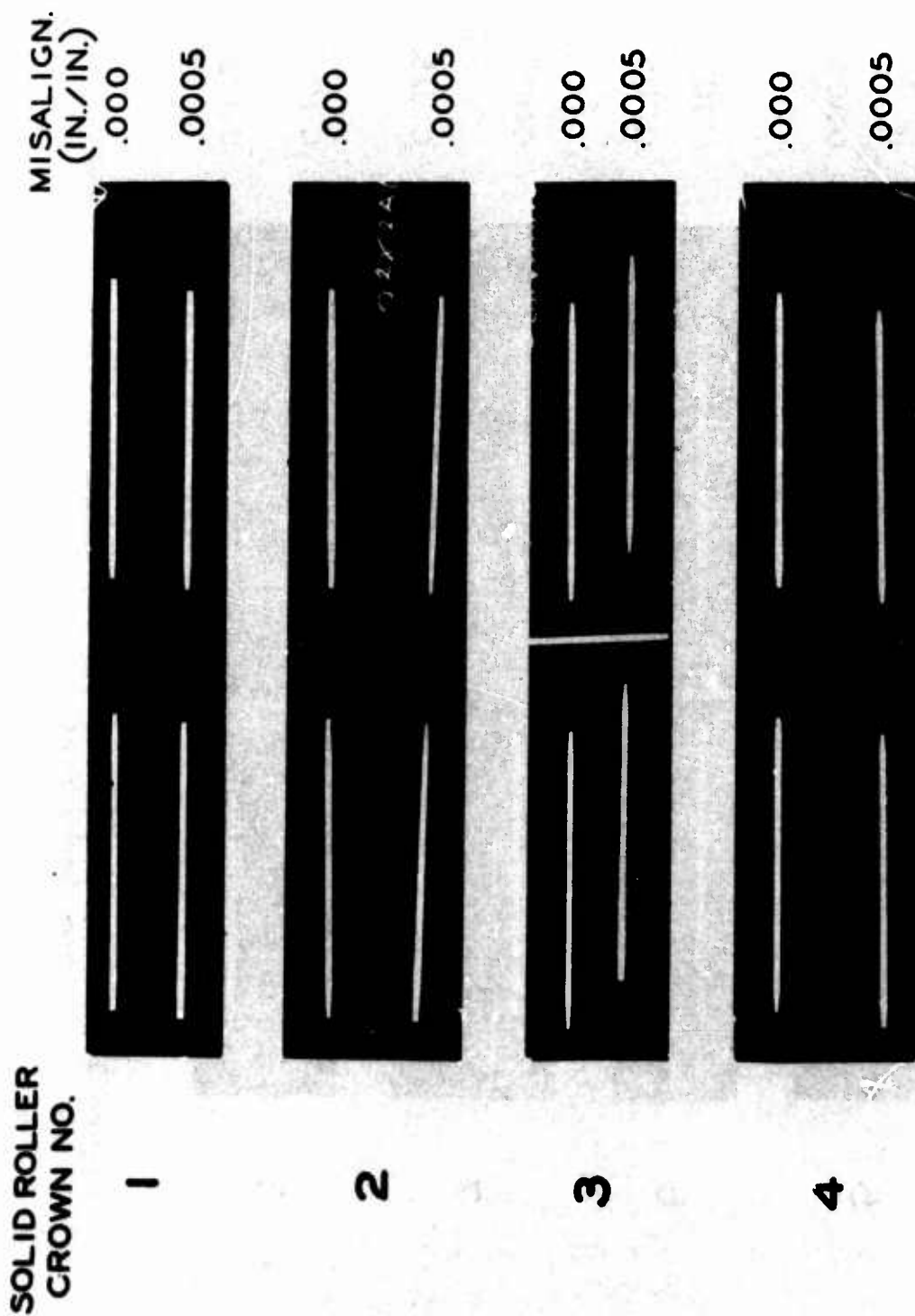
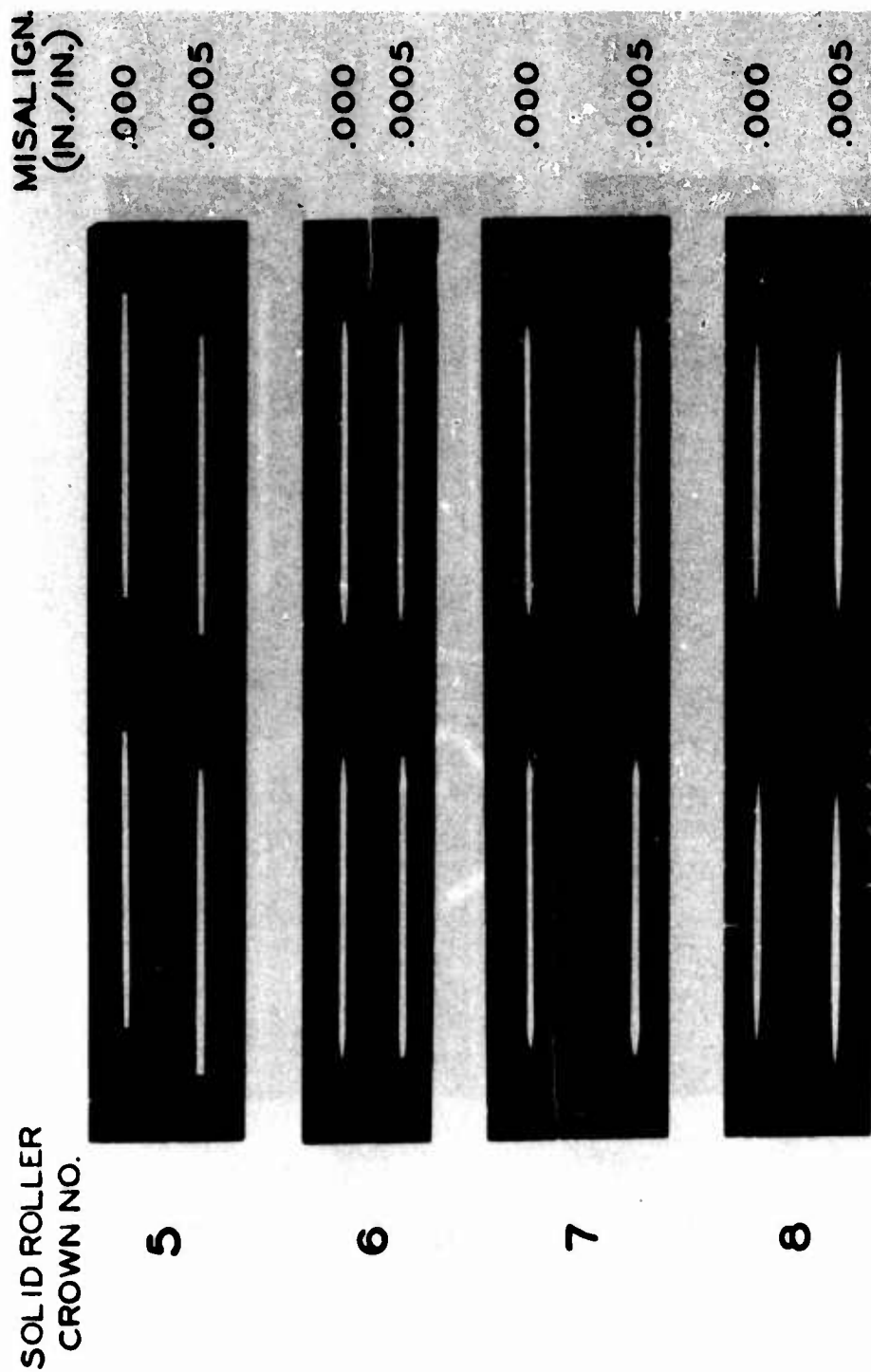


Figure 29. Etch Correction Factors for a Film Thickness of 99μ Inch.



18,000 Pounds Applied Load

Figure 30. Footprints Created Using Solid Rollers
With Various Crown Geometries.



18,000 Pounds Applied Load

Figure 31. Footprints Created Using Solid Rollers With Various Crown Geometries.

SOLID ROLLER
CROWN NO.

MISALIGN.
(IN./IN.)

9		.000
		.0005
10		.000
		.0005

18,000 Pounds Applied Load

Figure 32. Footprints Created Using Solid Rollers With Various Crown Geometries.

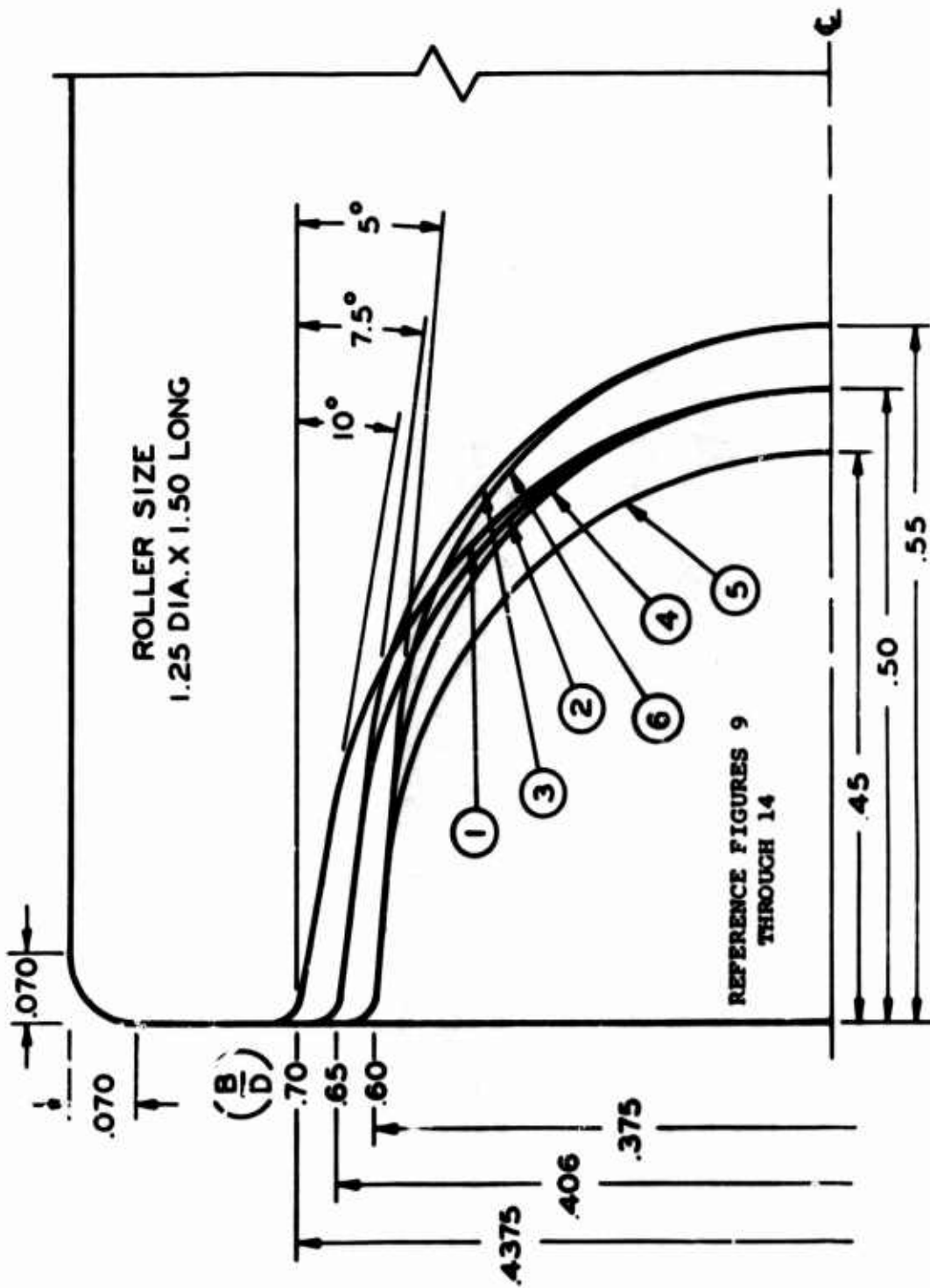


Figure 33. Prototype Hollow-Ended Roller Bore Shape Comparison.

PLATE NO. 25

18,000 LB. APPLIED LOAD
.003 IN./IN. MISALIGNMENT
NO. 10 CROWN

ENTRY
NO.

BORE
NO.

1
2
3
4
5
6
7

1
2
3
4
5
6
0
(SOLID)

NOTE - SEE TABLE NO. IV

Figure 34. Footprints Created Using Hollow-Ended Enders With Various Bore Configurations.

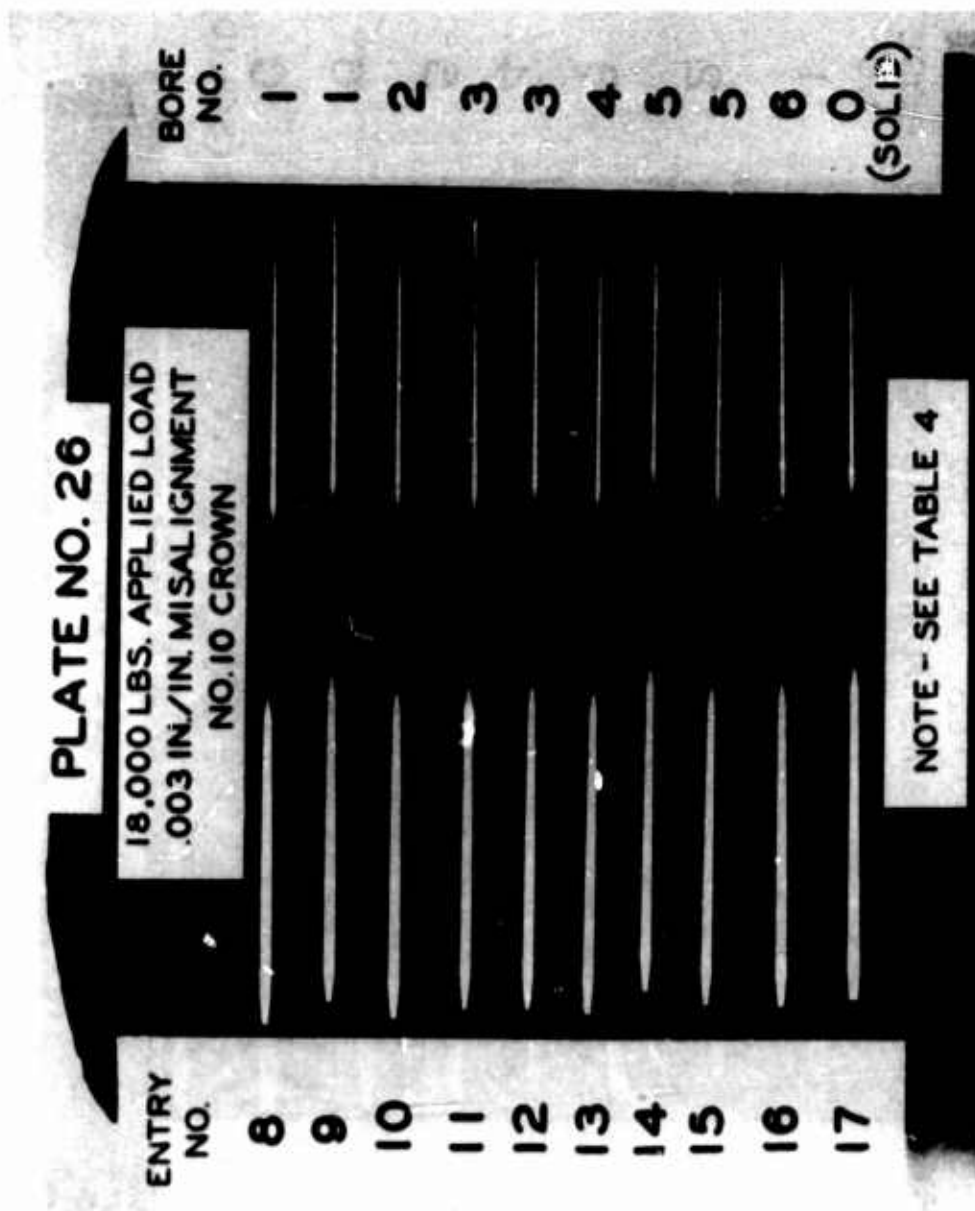
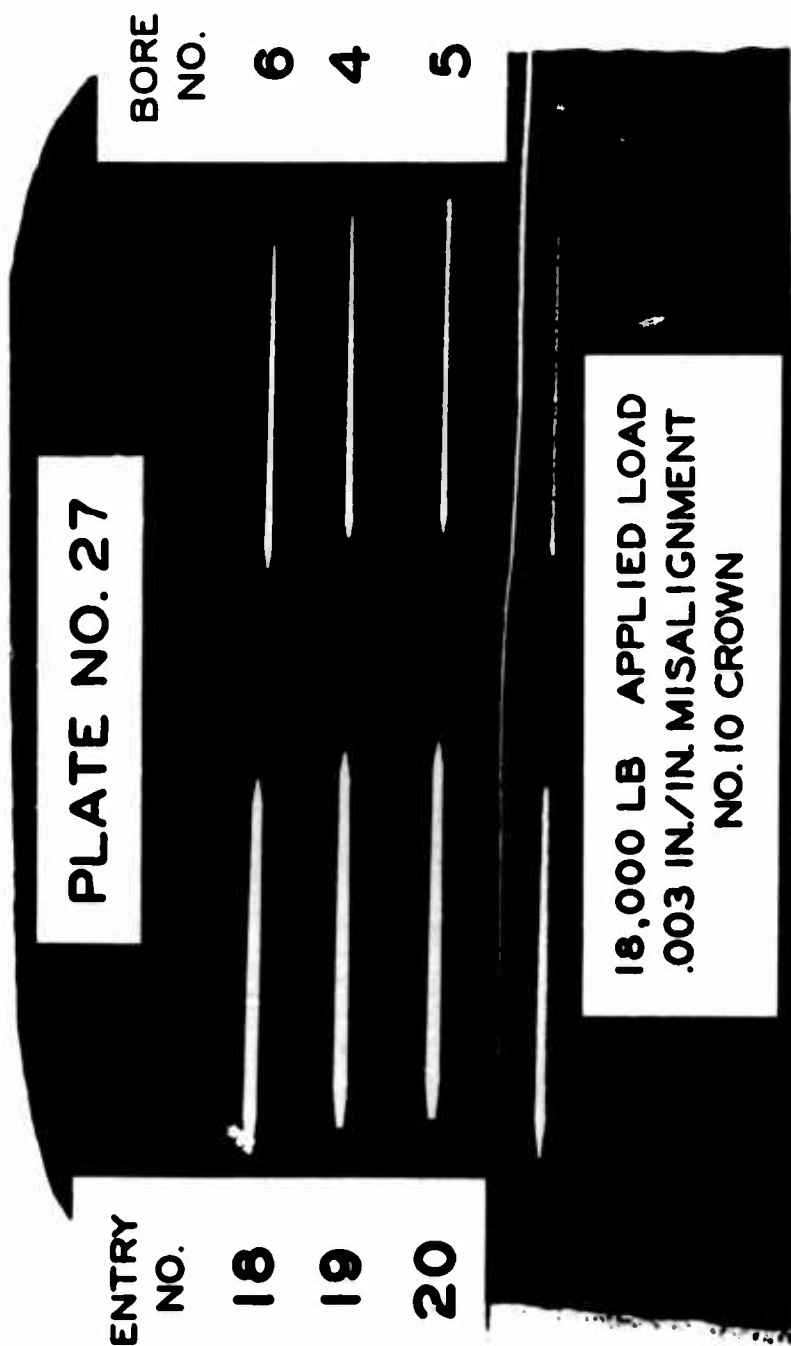


Figure 35. Footprints Created Using Hollow-Ended Rollers With Various Bore Configurations.



NOTE - SEE TABLE IV

Figure 36. Footprints Created Using Hollow-Ended Rollers With Various Bore Configurations.

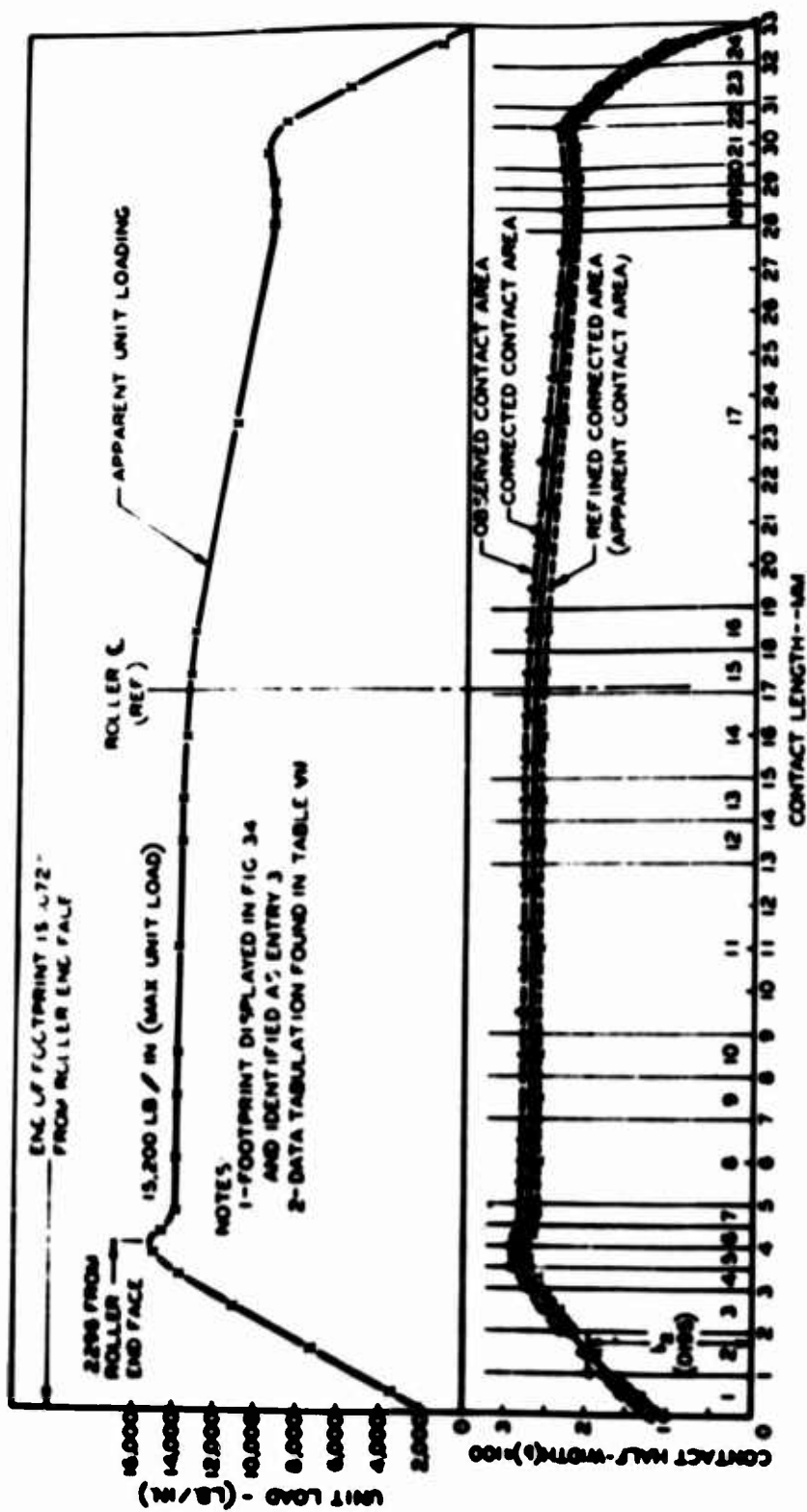


Figure 37. Graphical Layout and Resultant Load Analysis for the Most Heavily Loaded Hollow-Ended Roller Footprint (Major) in the Best Comparative Tandem Footprint Set.

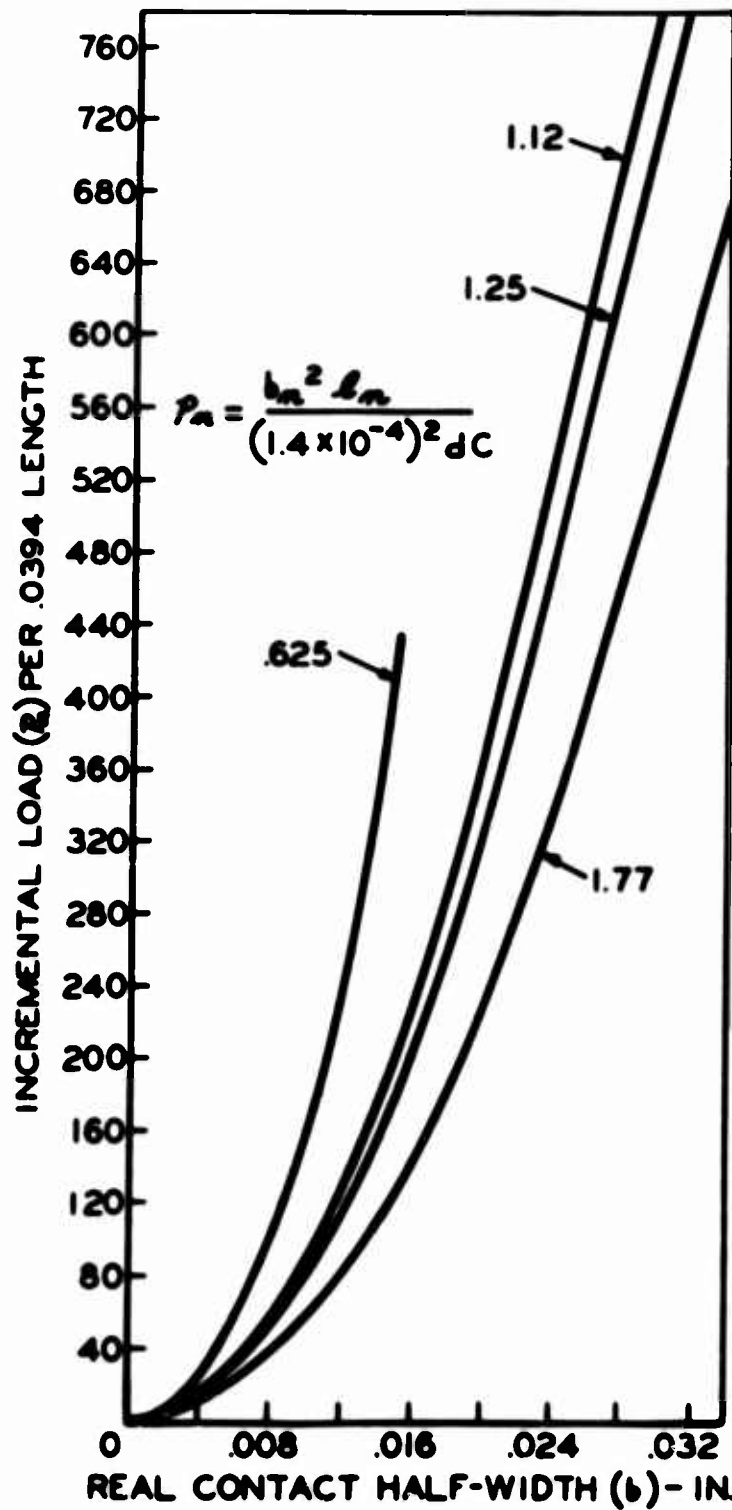


Figure 38. Load Required for Creating Contact Areas of Various Widths and .0394 Inch Length for Various Roller Diameters.

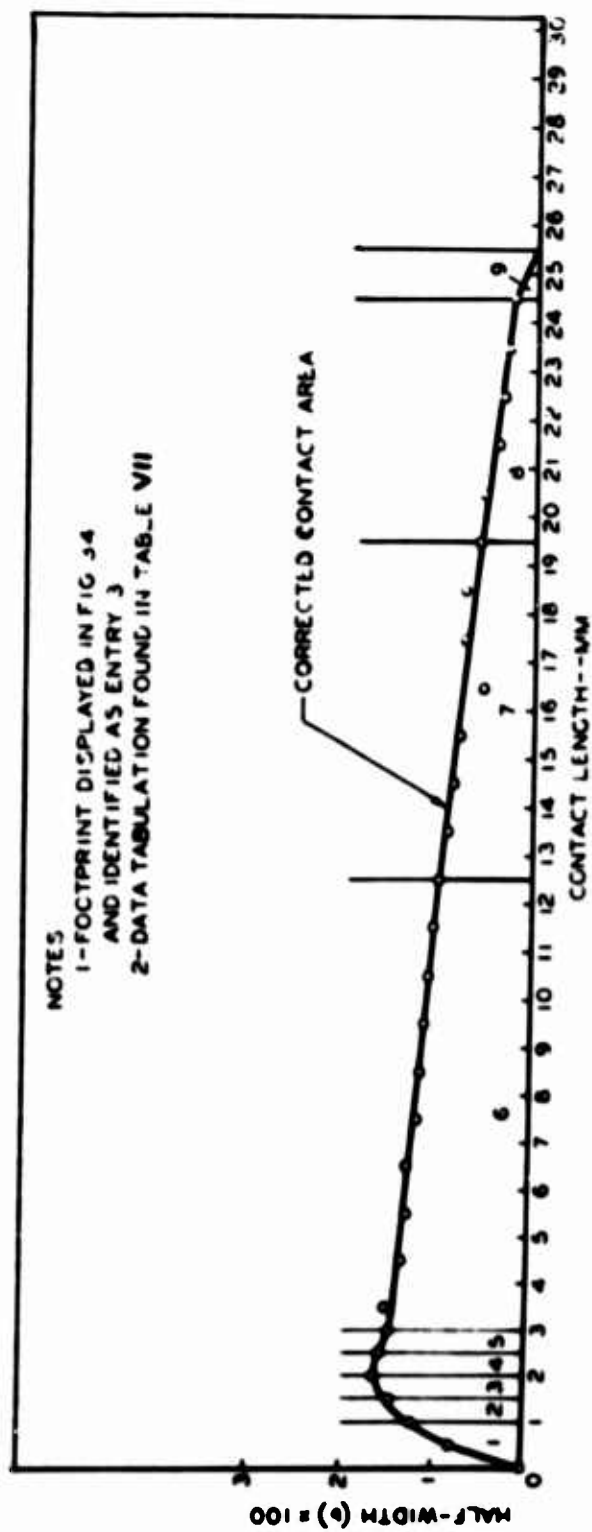


Figure 39. Graphical Layout and Resultant Load Analysis for the Least Loaded Hollow-Ended Roller Footprint (Minor) in the Best Comparative Tandem Footprint Set.

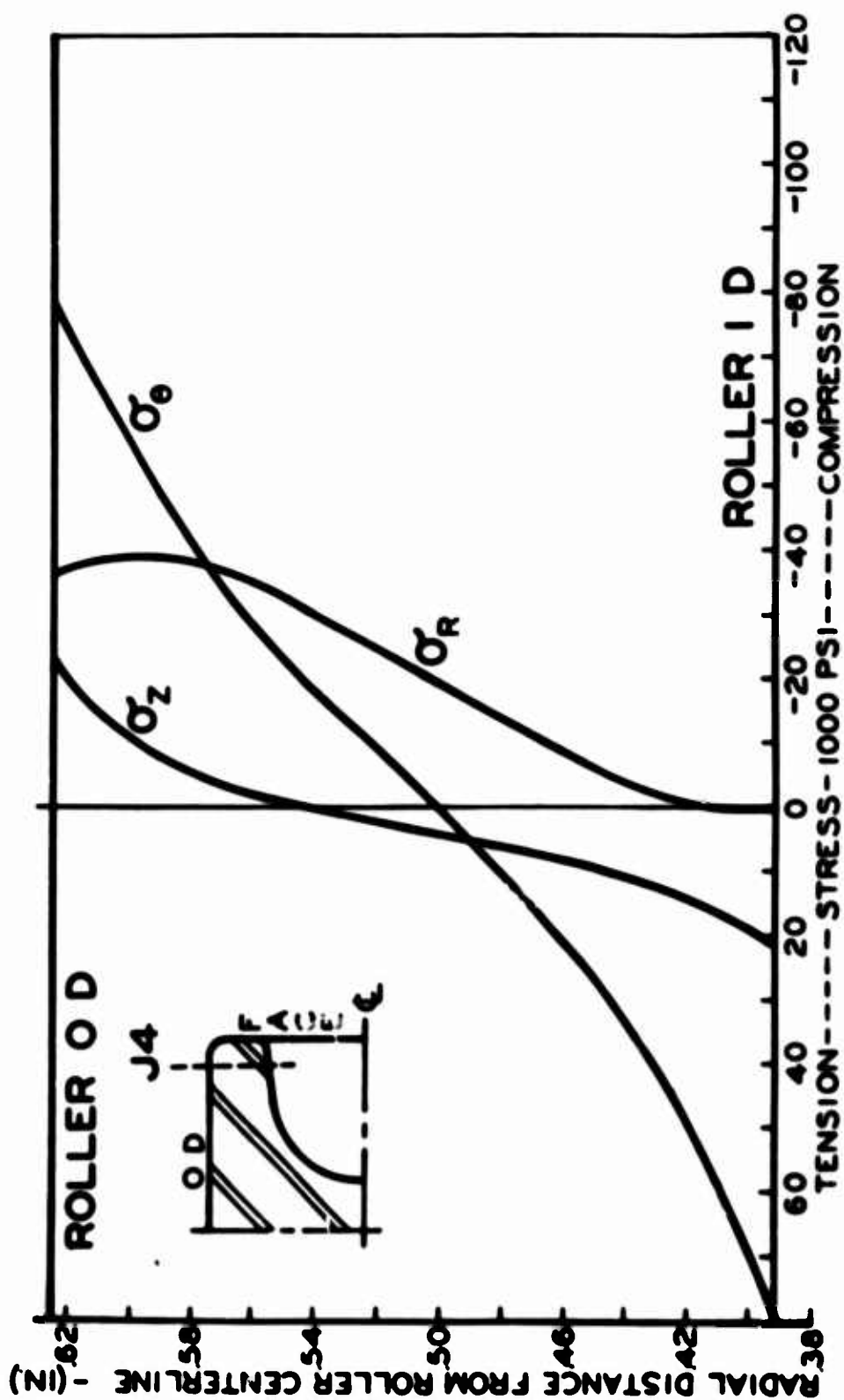


Figure 40. Stress Distribution (σ_H^* Stress State) in Hollow-Ended Roller Along Stress Plane J4 in Plane of Load ($\theta = 0^\circ$) From Bore to OD.

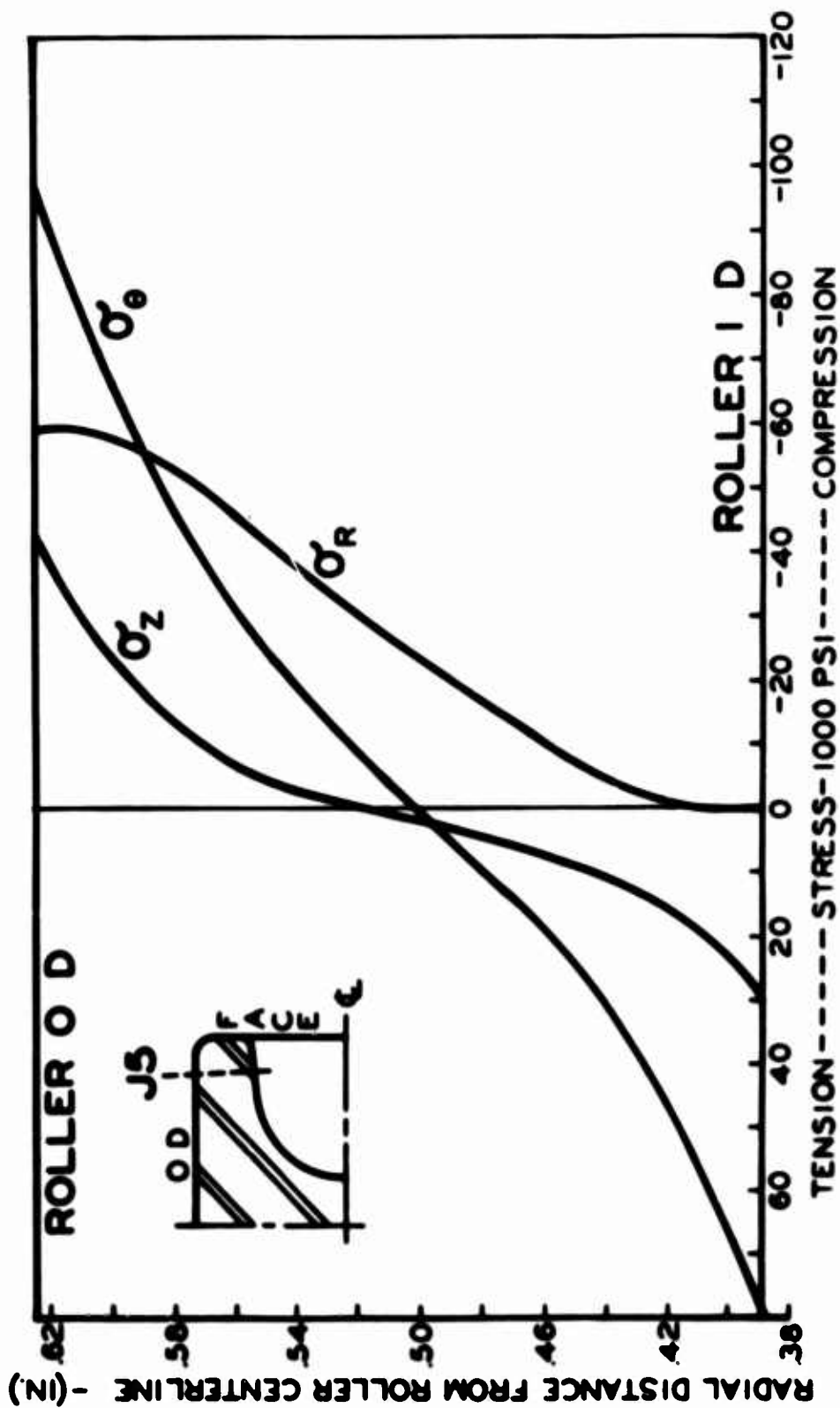


Figure 41. Stress Distribution (σ_H^* Stress State) in Hollow-Ended Roller Along Stress Plane J5 in Plane of Load ($\theta = 0^\circ$) From Bore to OD.

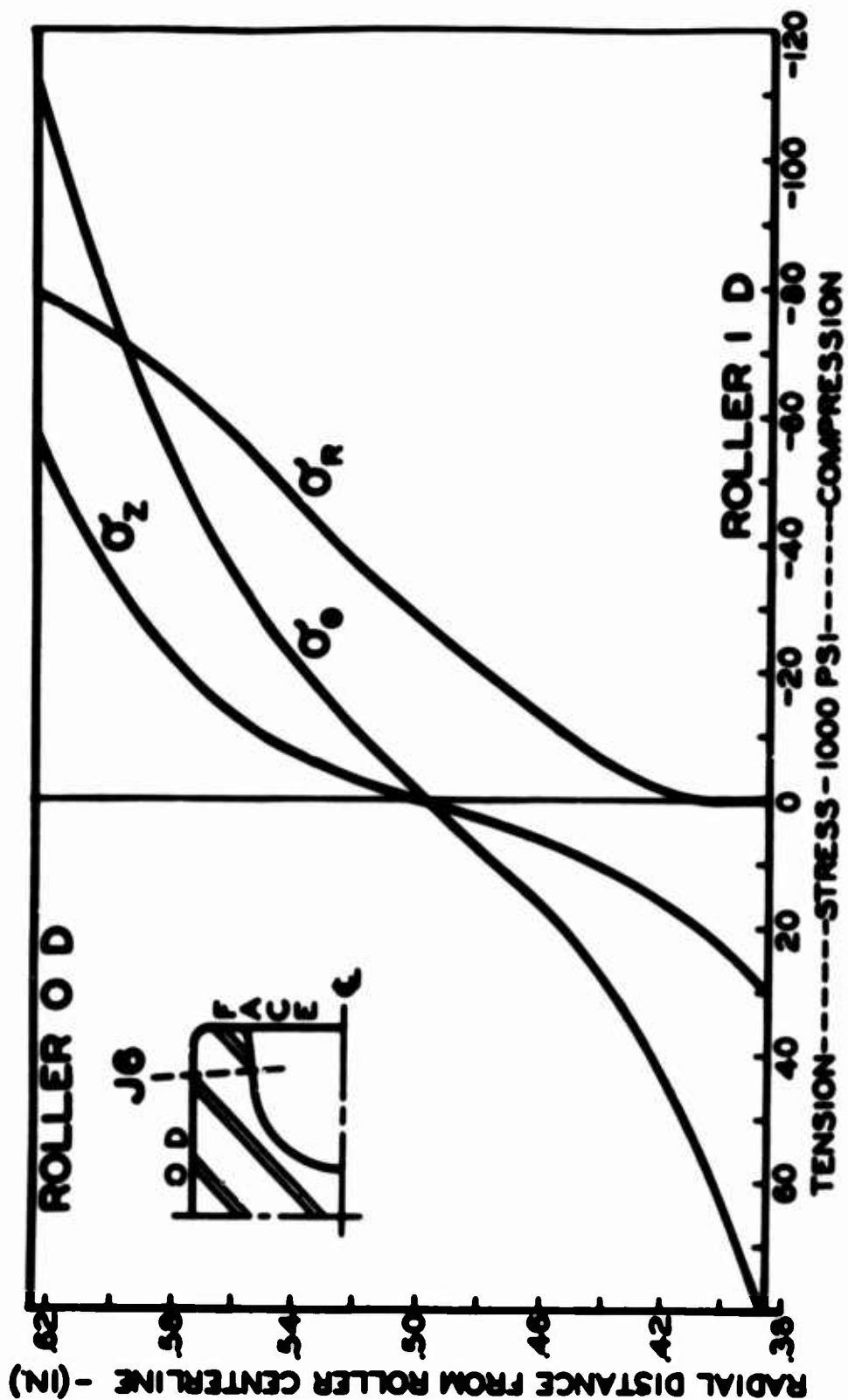


Figure 42. Stress Distribution (σ_H* Stress State) in Hollow-Ended Roller Along Stress Plane J6 in Plane of Load (θ = 0°) from Bore to OD.

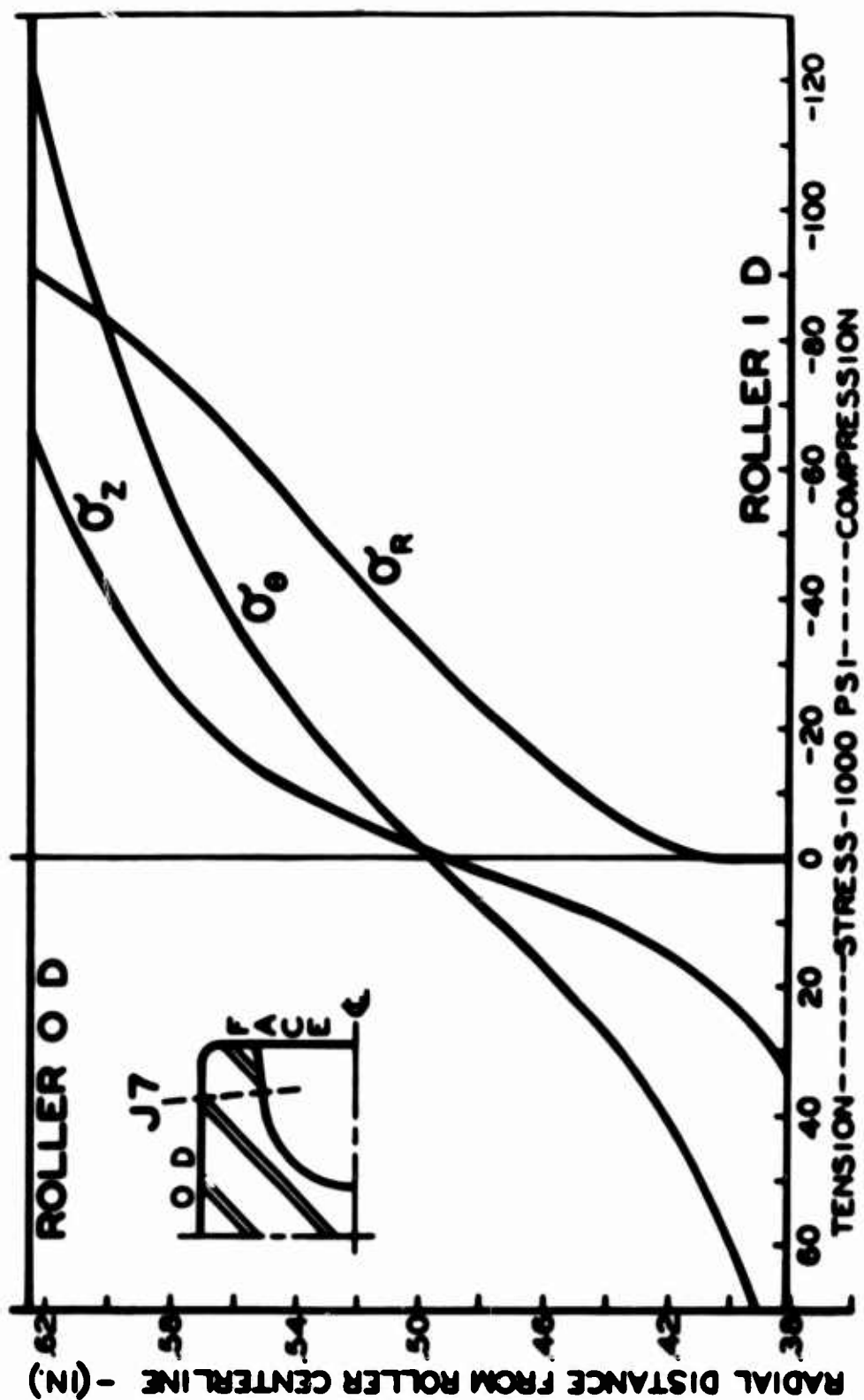


Figure 43. Stress Distribution (σ_H^* Stress State) in Hollow-Ended Roller Along Stress Plane J7 in Plane of Load ($\theta = 0^\circ$) from Bore to OD.

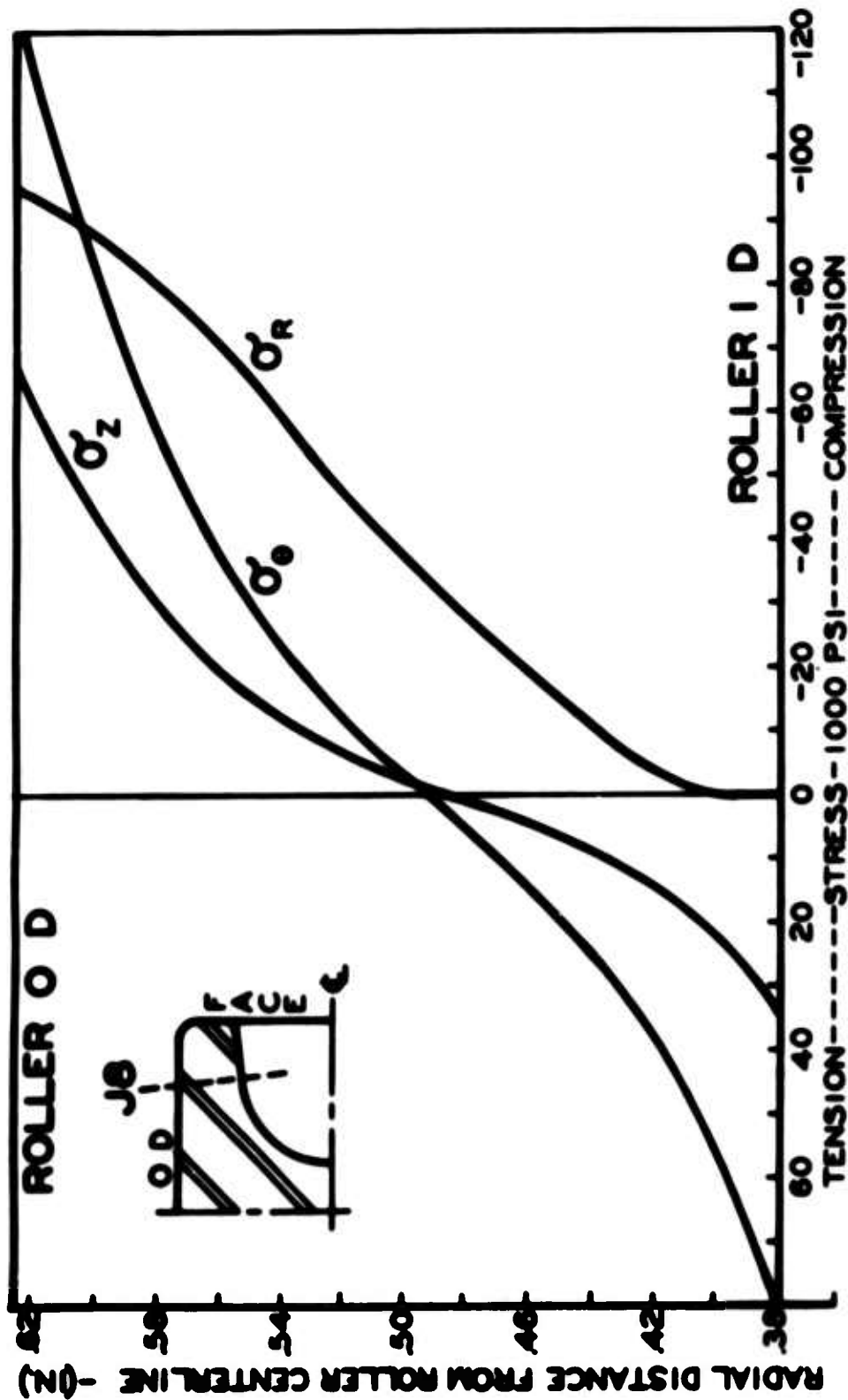


Figure 44. Stress Distribution (σ_H^* Stress State) in Hollow-Ended Roller Along Stress Plane J8 in Plane of Load ($\theta = 0^\circ$) from Bore to OD.

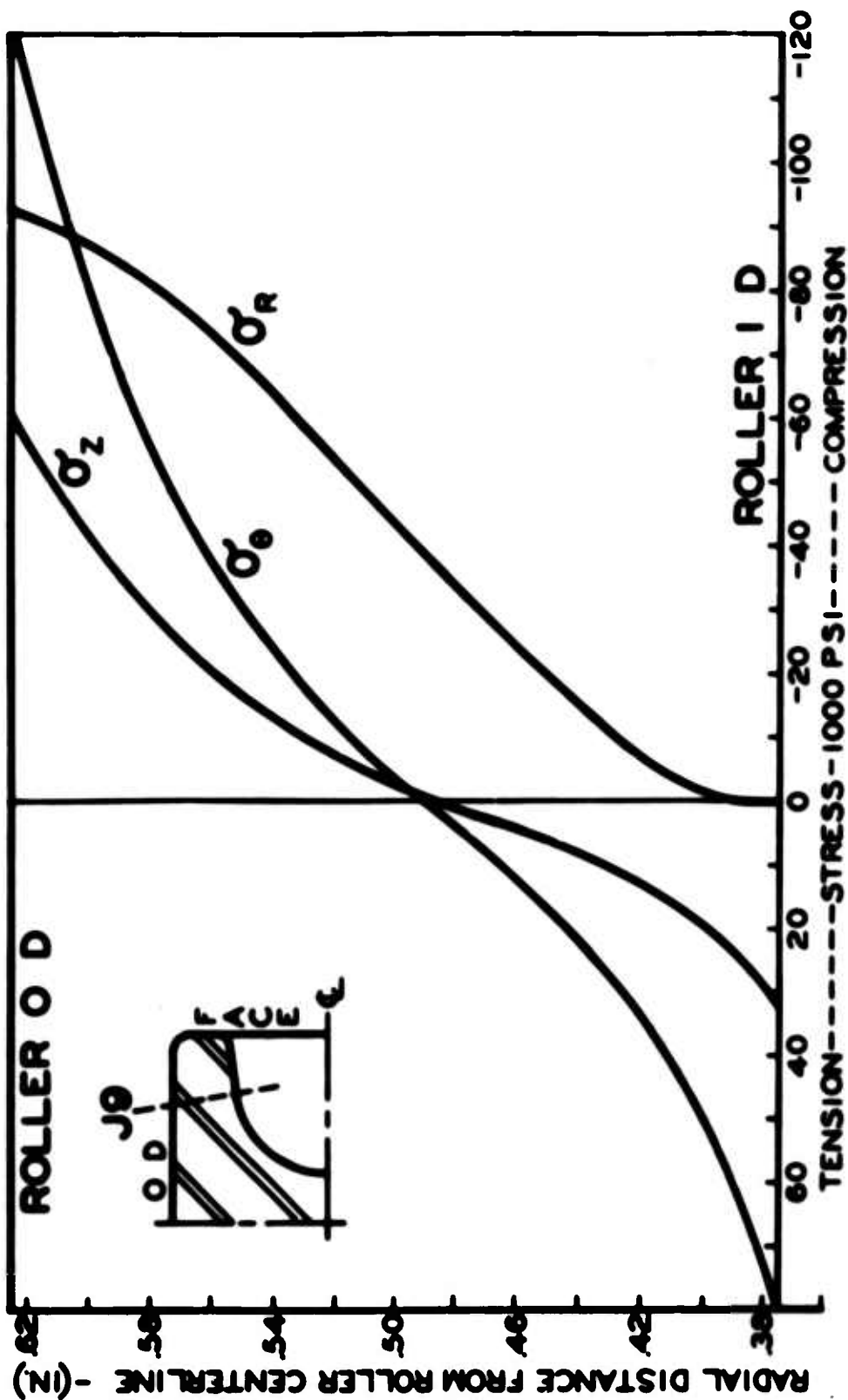


Figure 45. Stress Distribution (σ_H^* Stress State) in Hollow-Ended Roller Along Stress Plane J9 in Plane of Load ($\theta = 0^\circ$) from Bore to OD.

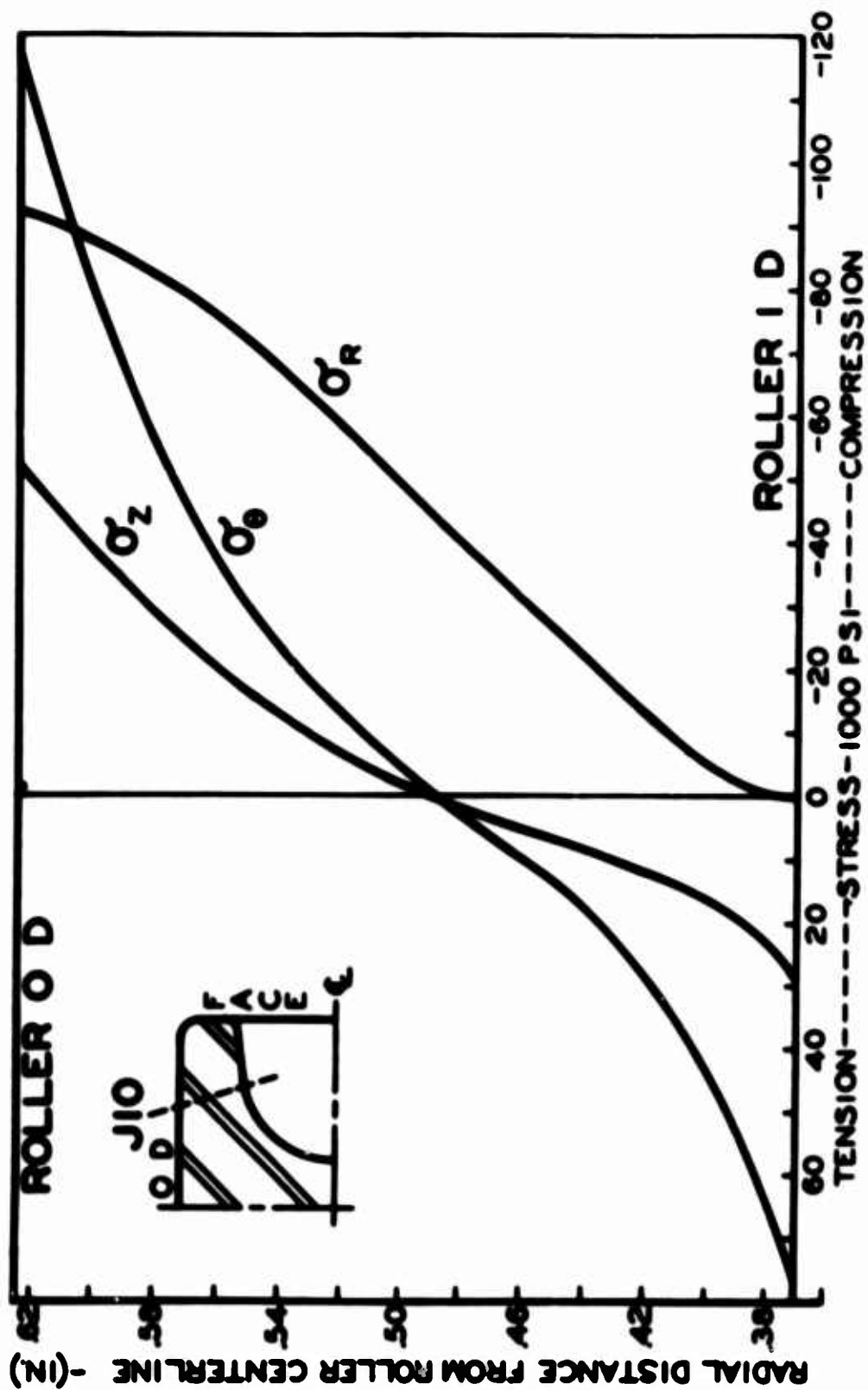


Figure 46. Stress Distribution (σ_H^* Stress State) in Hollow-Ended Roller Along Stress Plane J10 in Plane of Load ($\theta = 0^\circ$) from Bore to OD.

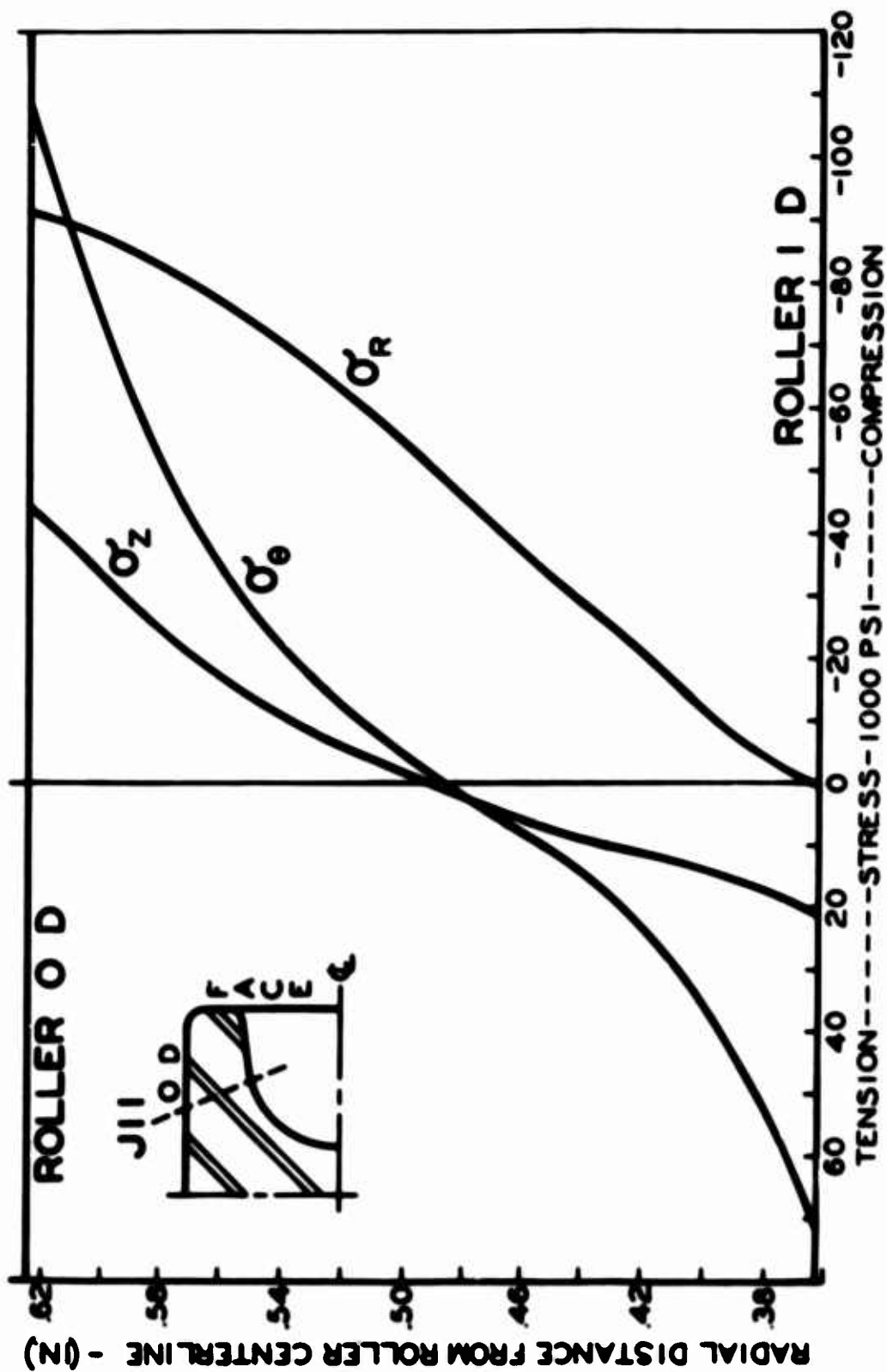


Figure 47. Stress Distribution (σ_H^* Stress State) in Hollow-Ended Roller Along Stress Plane J II in Plane of Load ($\theta = 0^\circ$) from Bore to OD.

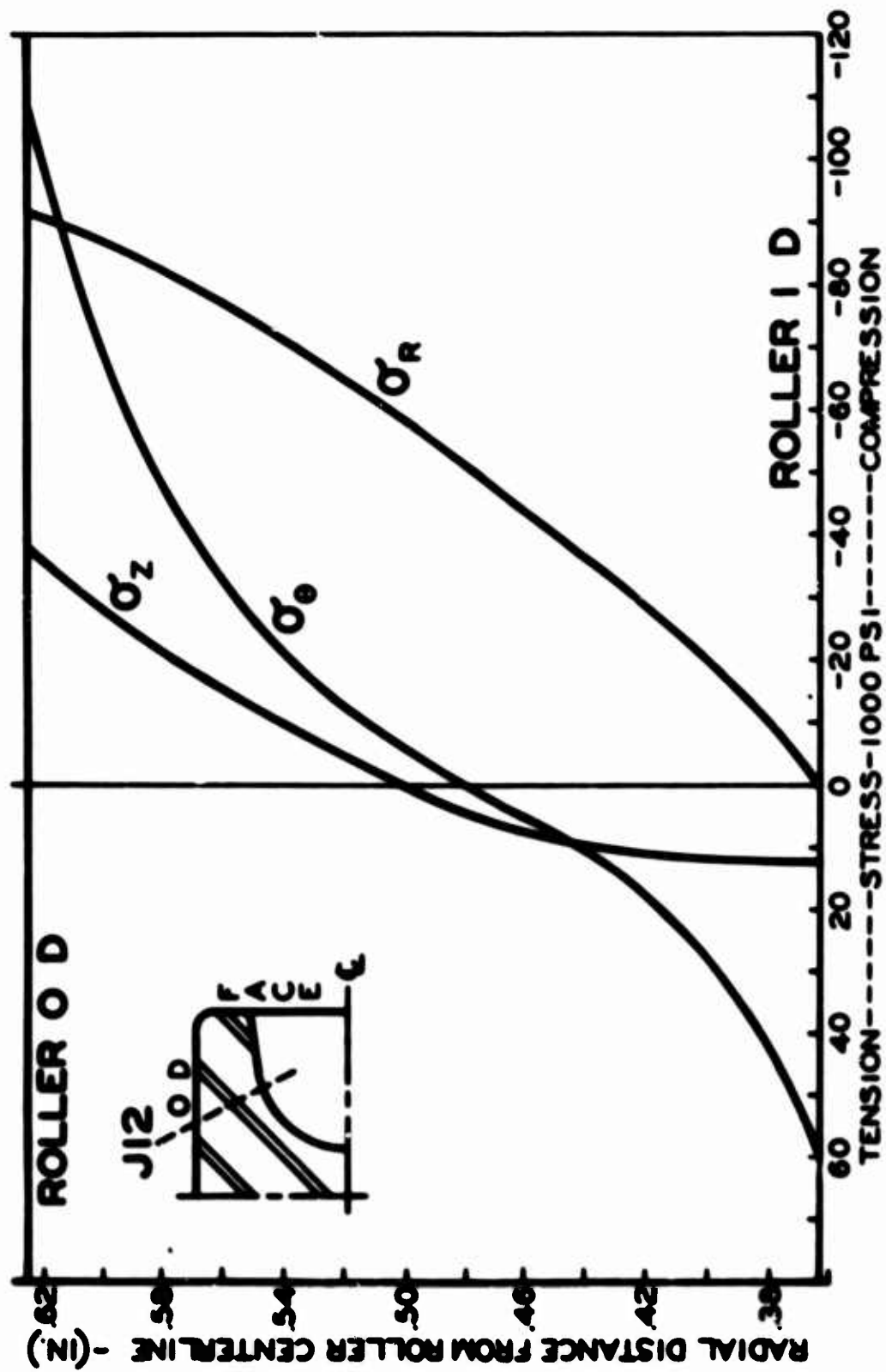


Figure 48. Stress Distribution (σ_H^* Stress State) in Hollow-Ended Roller Along Stress Plane J12 in Plane of Load ($\theta = 0^\circ$) from Bore to OD.

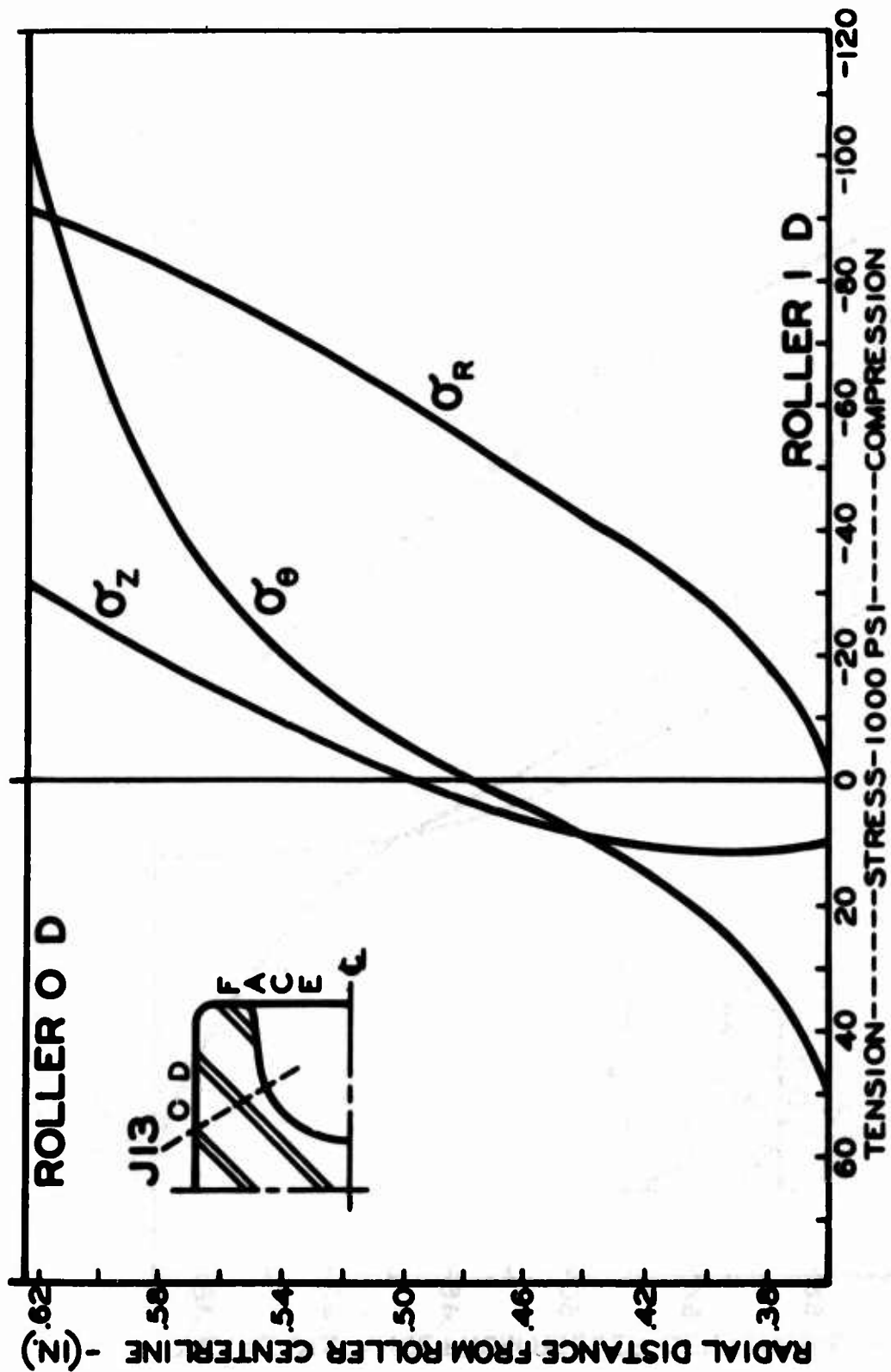


Figure 49. Stress Distribution (σ_H^* Stress State) in Hollow-Ended Roller Along Stress Plane J13 in Plane of Load ($\theta = 0^\circ$) from Bore to OD.

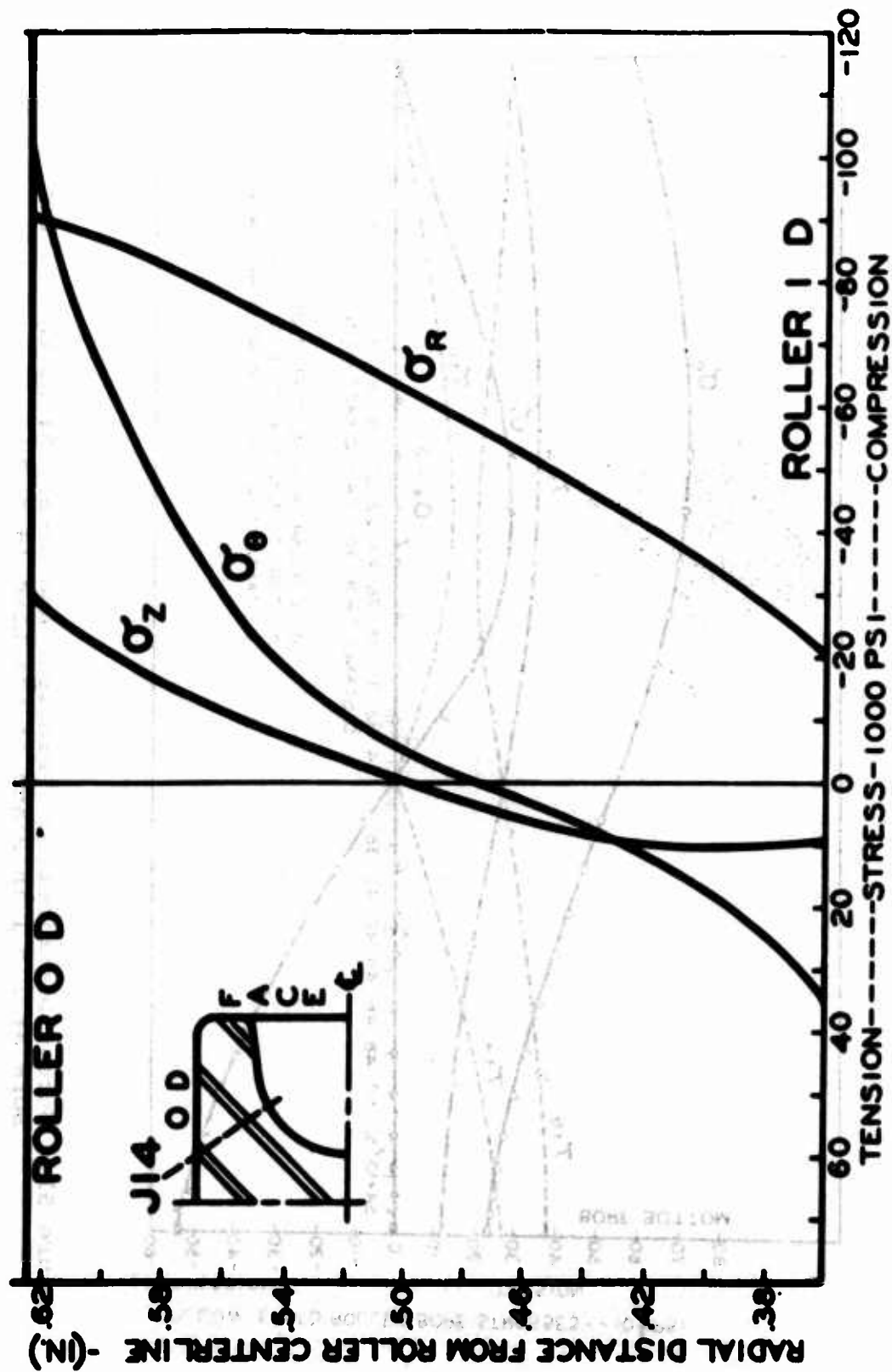


Figure 50. Stress Distribution (σ_H^* Stress State) in Hollow-Ended Roller Along Stress Plane J14 in Plane of Load ($\theta = 0^\circ$) from Bore to OD.

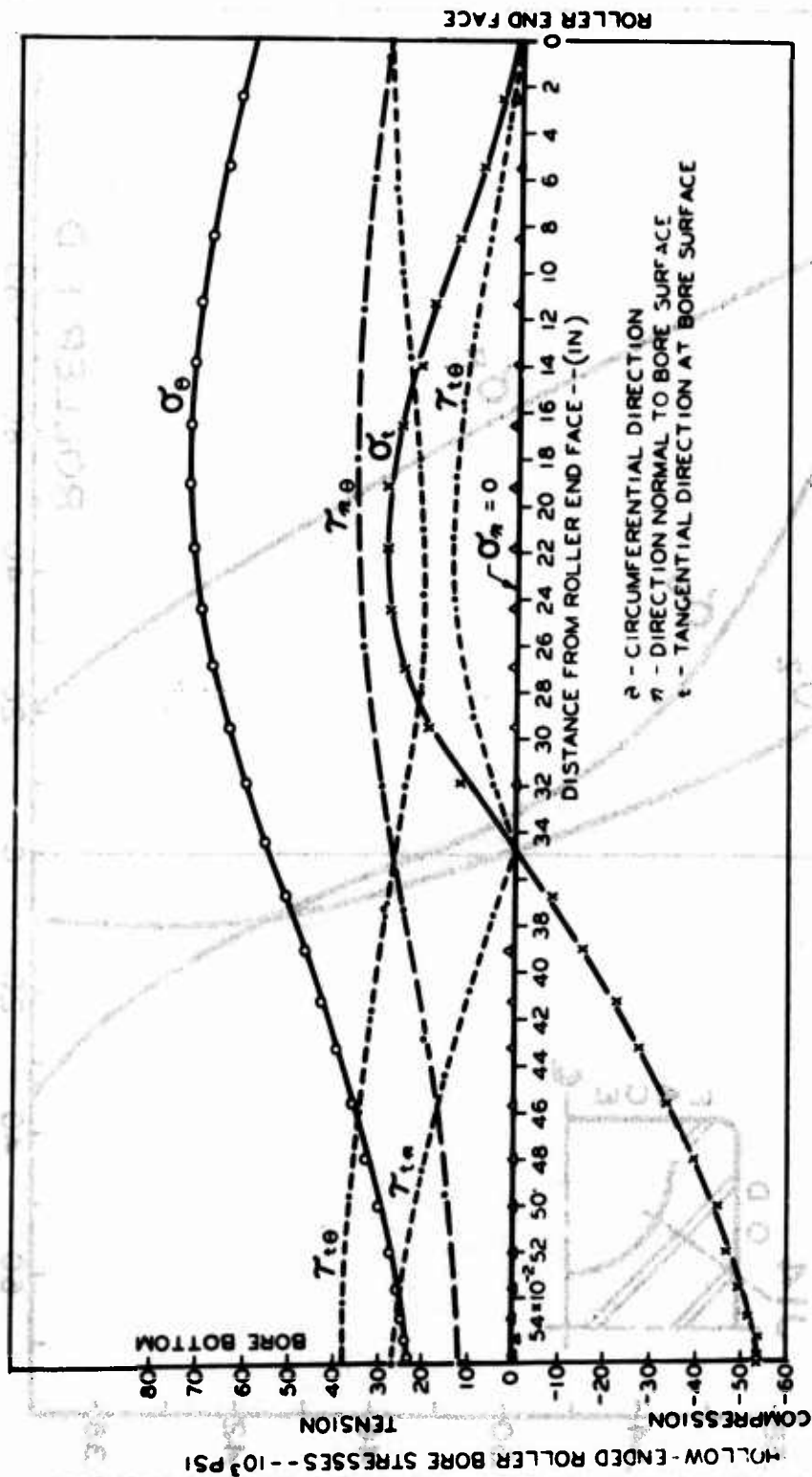


Figure 51. Stress Distribution (Principal and Shear) Along the Roller Bore at $I = 1$ in Plane of the Load ($\theta = 0^\circ$).

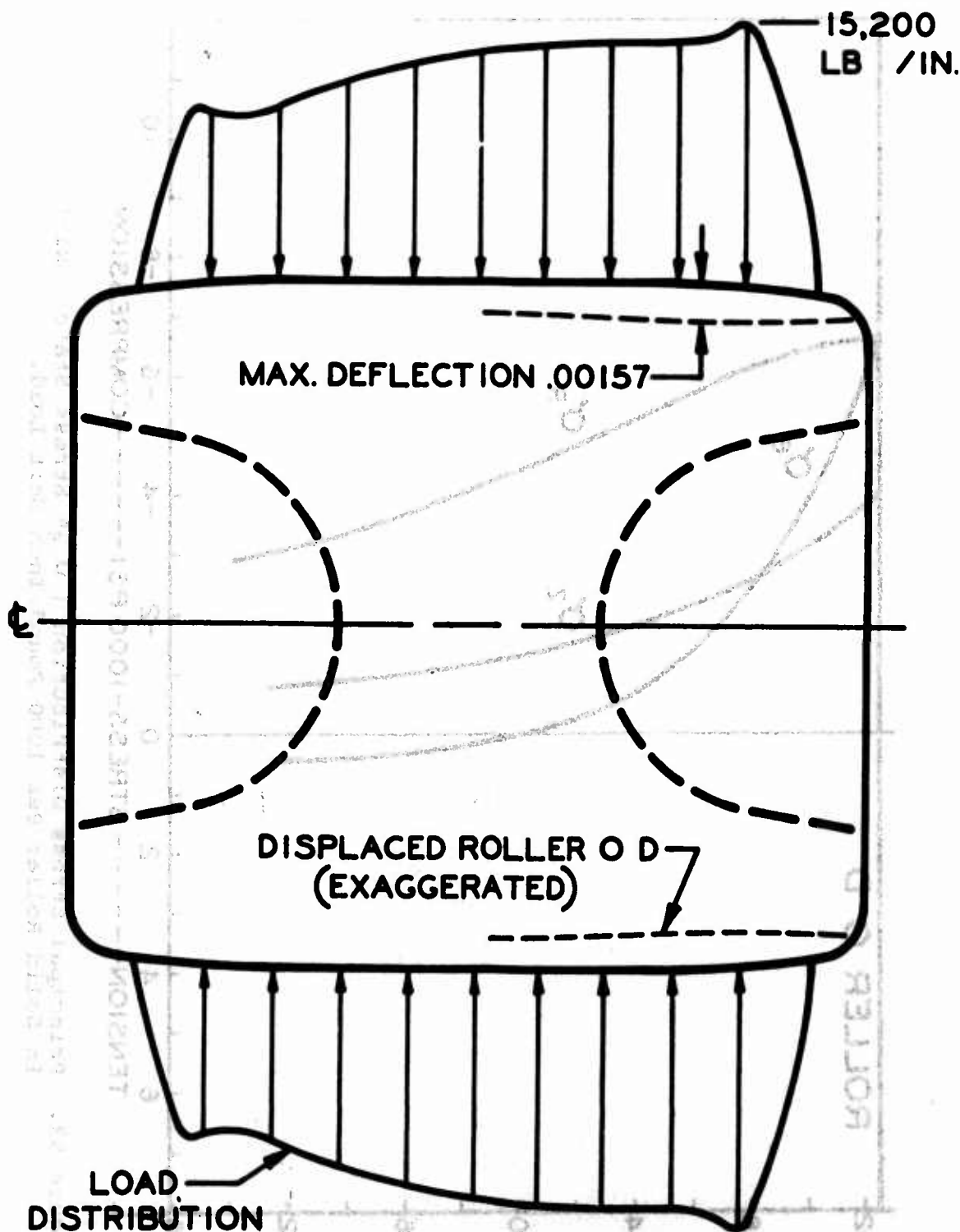


Figure 52. Elastic Radial Displacement of Hollow-Ended Roller Rim at Contact Surface.

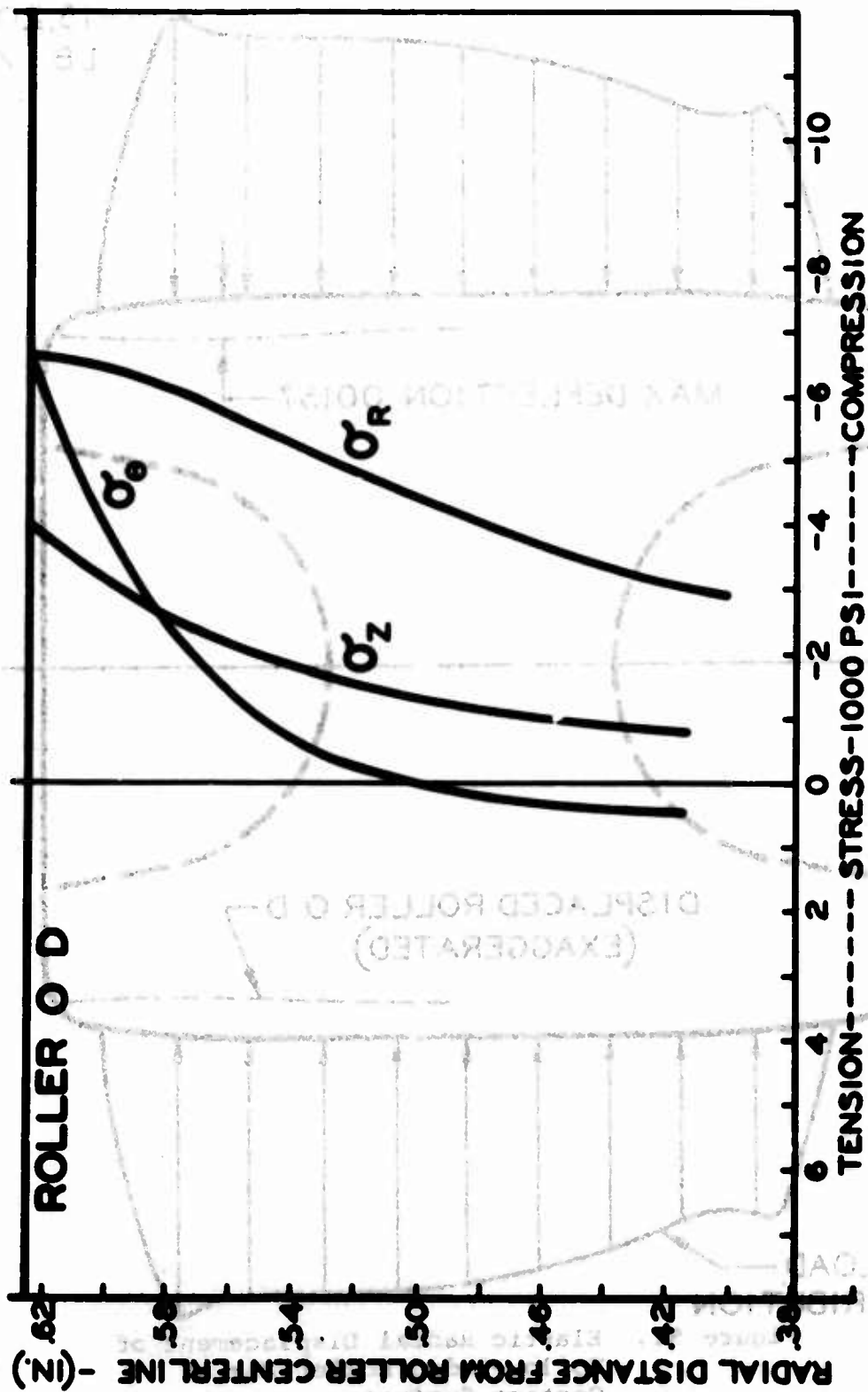


Figure 53. Principal Stress Distribution (σ_s^* Stress State) Existing in Solid Roller Per 1000 Pound/Inch Unit Load.

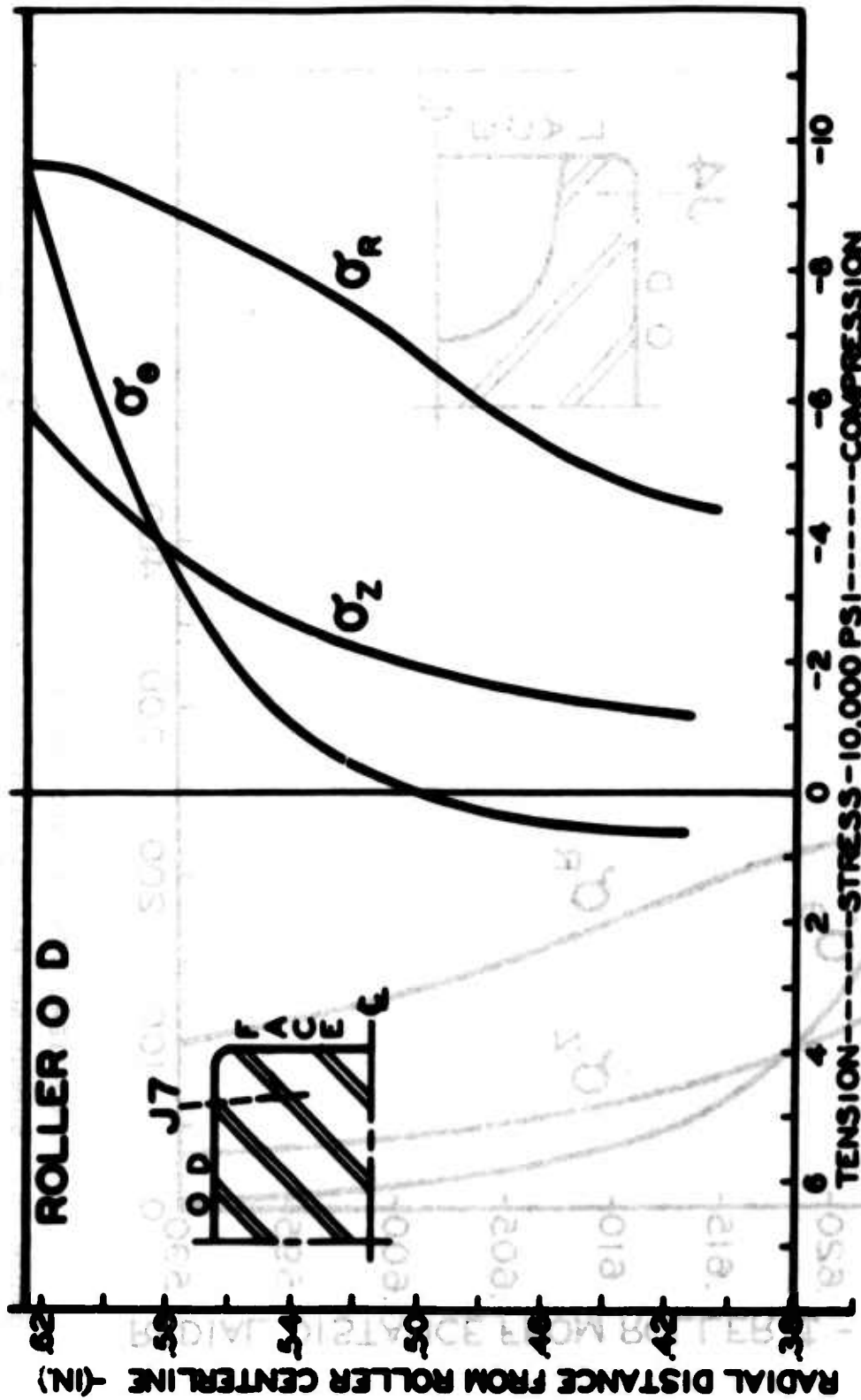


Figure 54. Principal Stress Distribution (σ_x , σ_r , σ_z Stress State) Existing in Solid Roller for a 14,630 Pound/Inch Unit Load - Plane J7.

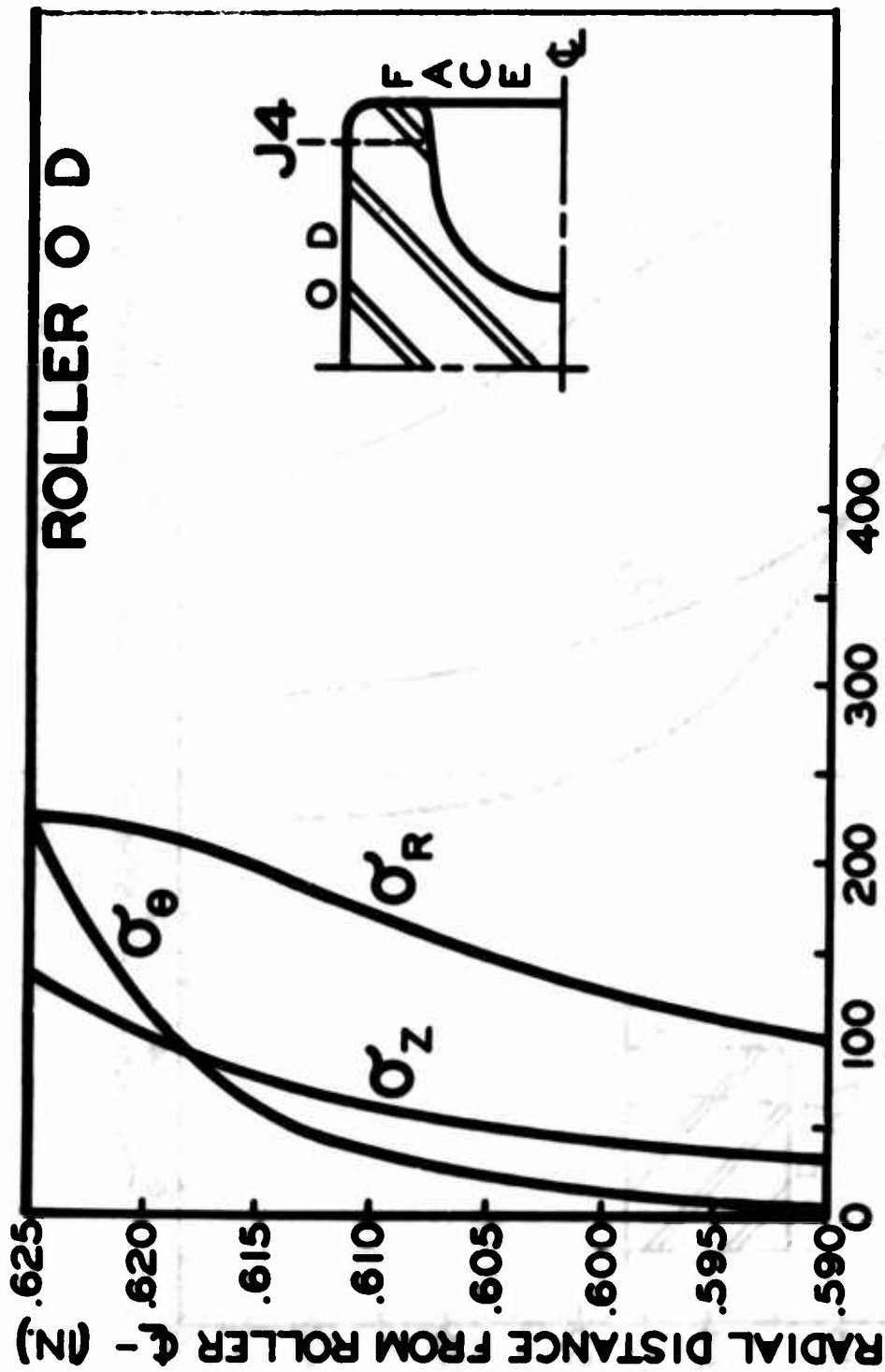


Figure 55. Subsurface Principal Stress Distribution (σ_s Stress State) in Hollow-Ended Roller Due to Hertzian Contact in Plane of Load ($\theta = 0^\circ$) Along J4 Stress Plane.

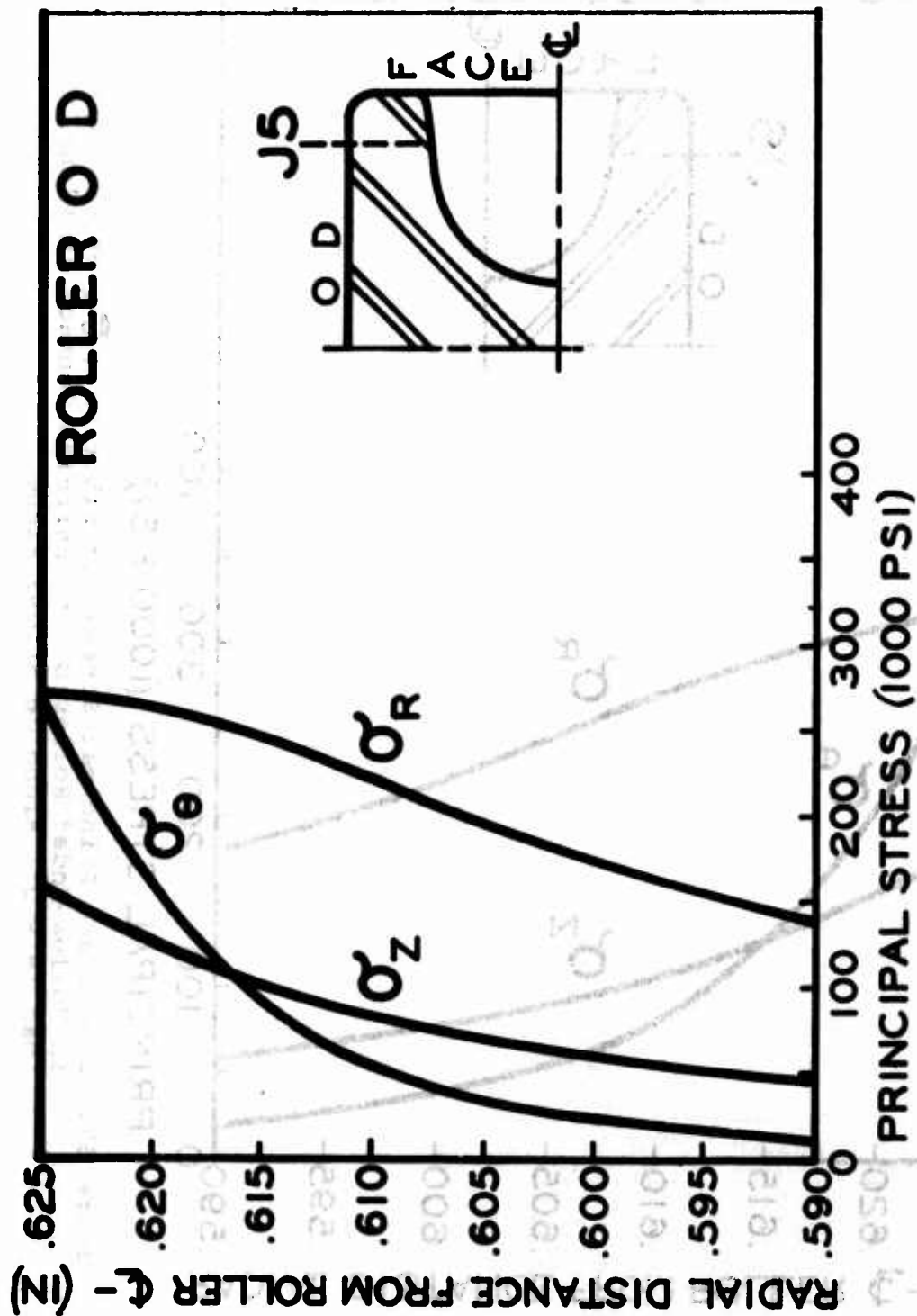


Figure 56. Subsurface Principal Stress Distribution (σ_s Stress State) in Hollow-Ended Roller Due to Hertzian Contact in Plane of Load ($\theta = 0^\circ$) Along J5 Stress Plane.

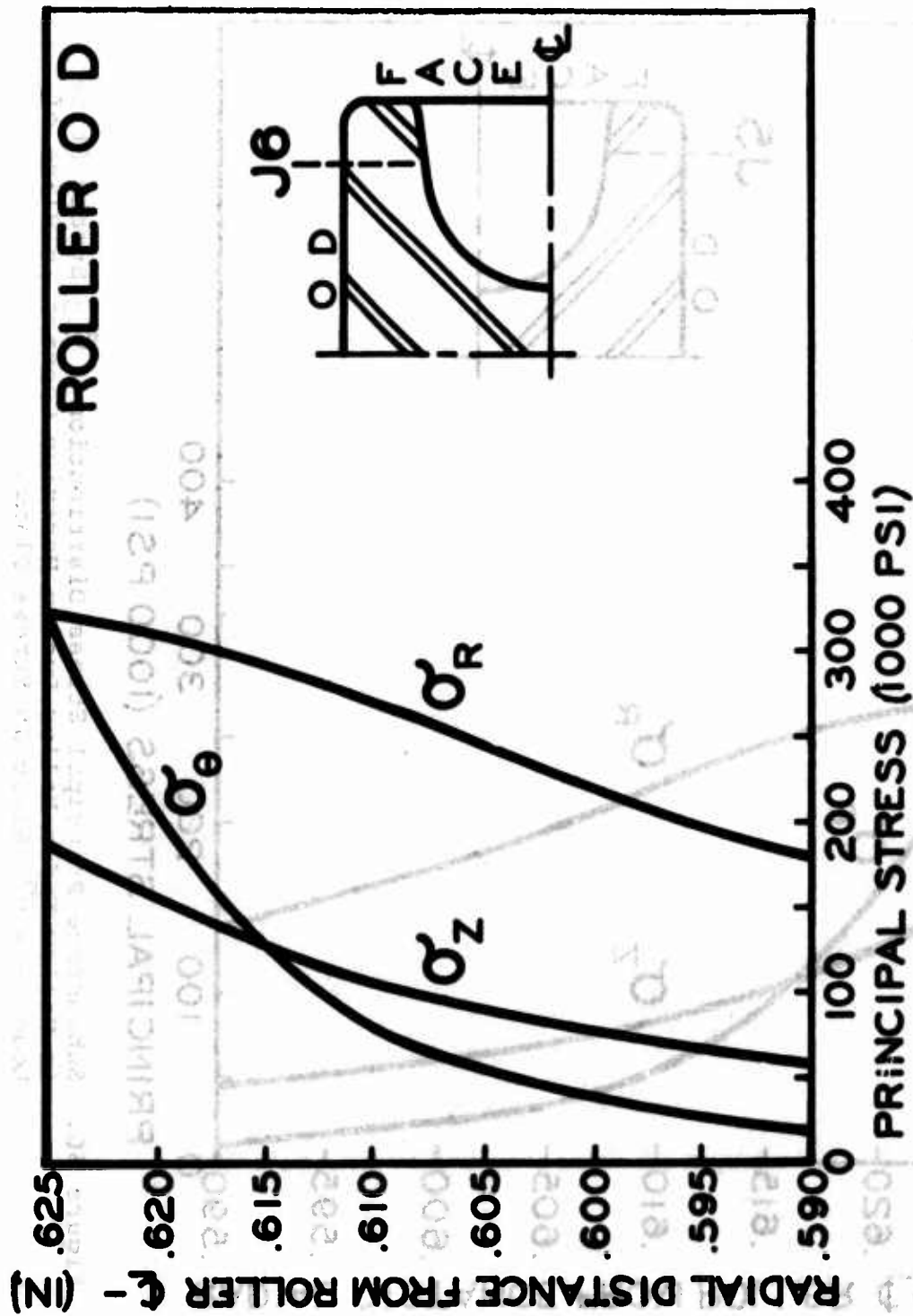


Figure 57. Subsurface Principal Stress Distribution (σ_s Stress State) in Hollow-Ended Roller Due to Hertzian Contact in Plane of Load ($\theta = 0^\circ$) Along J6 Stress Plane.

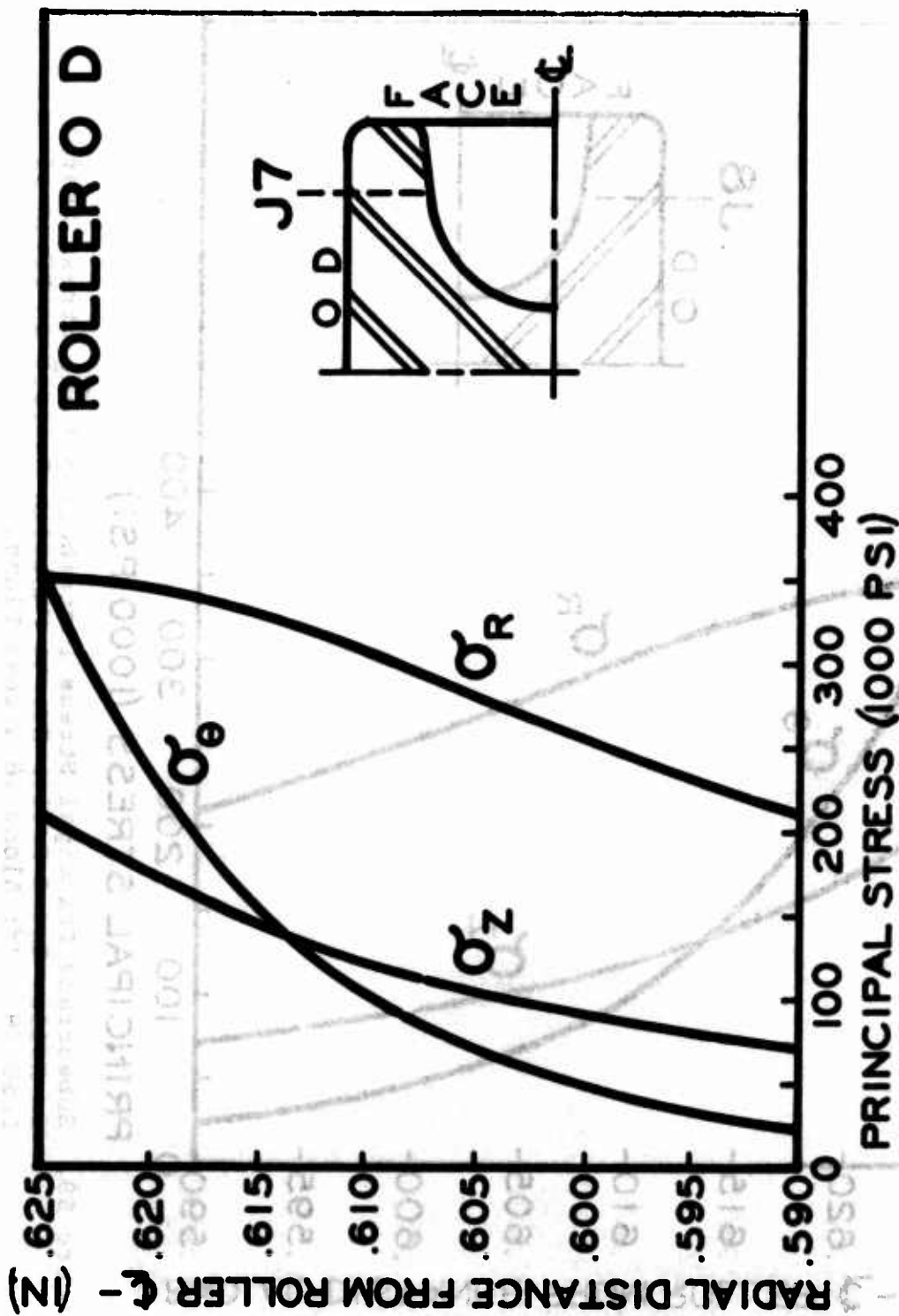


Figure 58. Subsurface Principal Stress Distribution (σ_s Stress State) in Hollow-Ended Roller Due to Hertzian Contact in Plane of Load ($\theta = 0^\circ$) Along J7 Stress Plane.

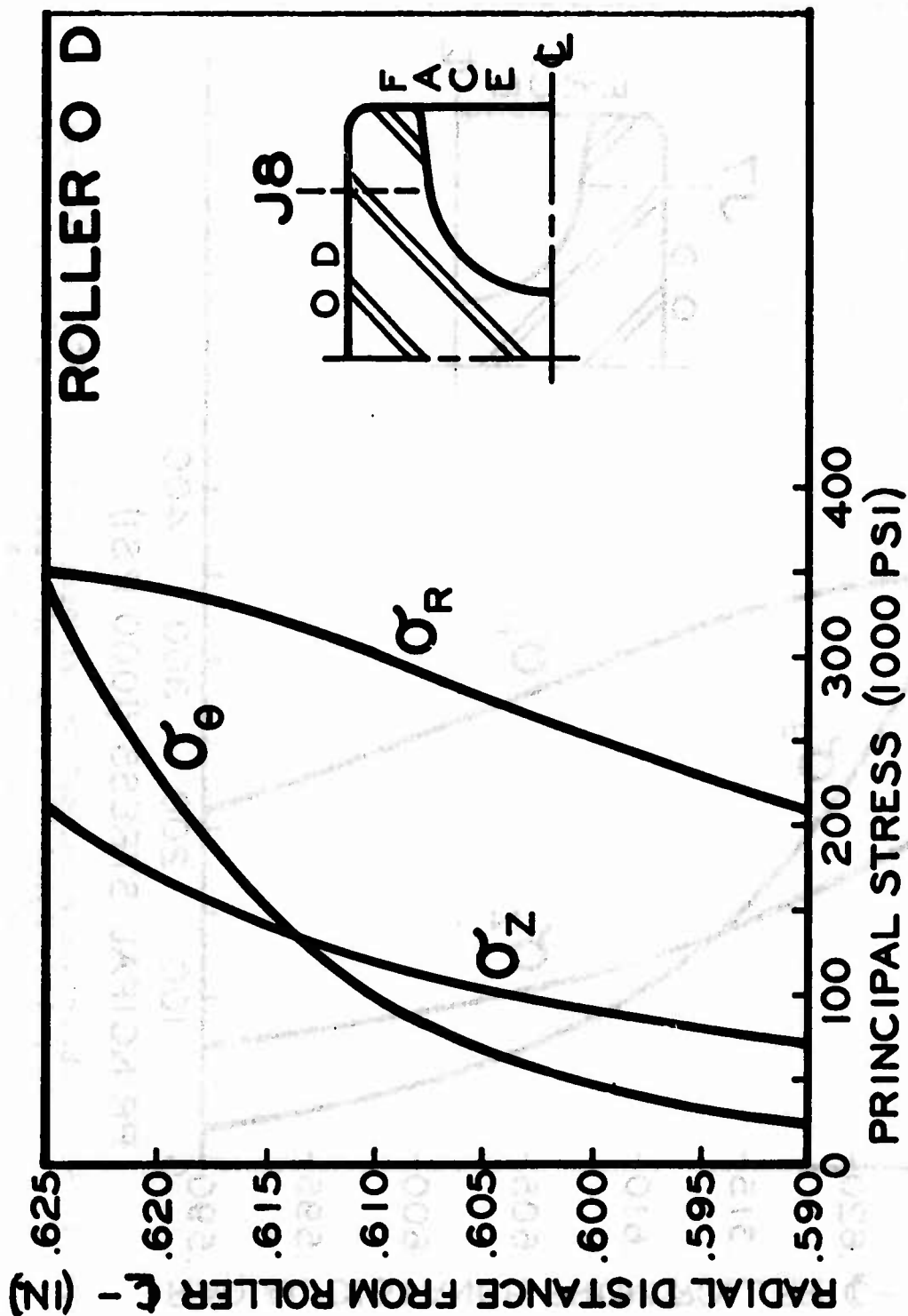


Figure 59. Subsurface Principal Stress Distribution (σ_s Stress State) in Hollow-Ended Roller Due to Hertzian Contact in Plane of Load ($\theta = 0^\circ$) Along J8 Stress Plane.

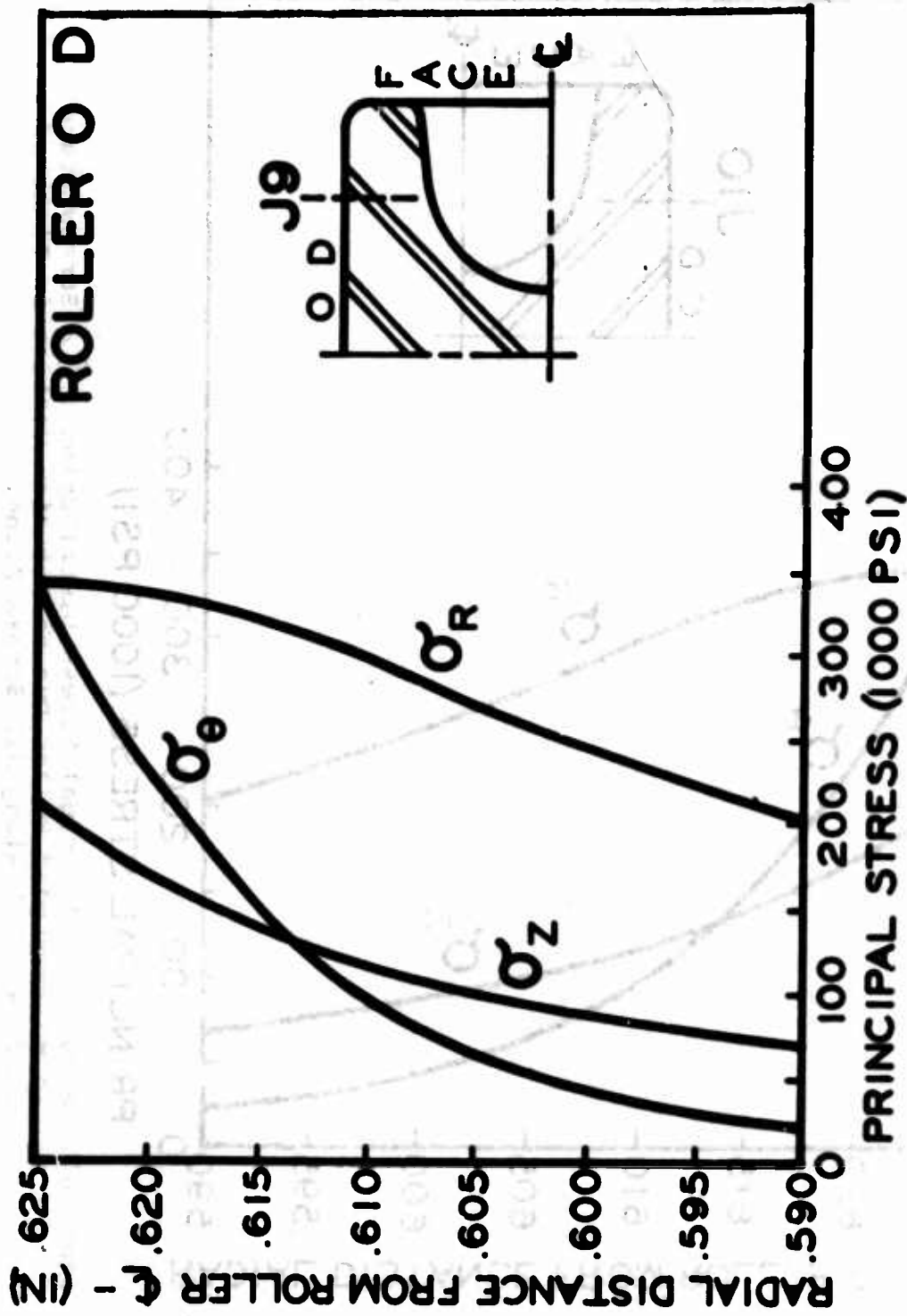


Figure 60. Subsurface Principal Stress Distribution (σ_θ Stress State) in Hollow-Ended Roller Due to Hertzian Contact in Plane of Load ($\theta = 0^\circ$) Along J9 Stress Plane.

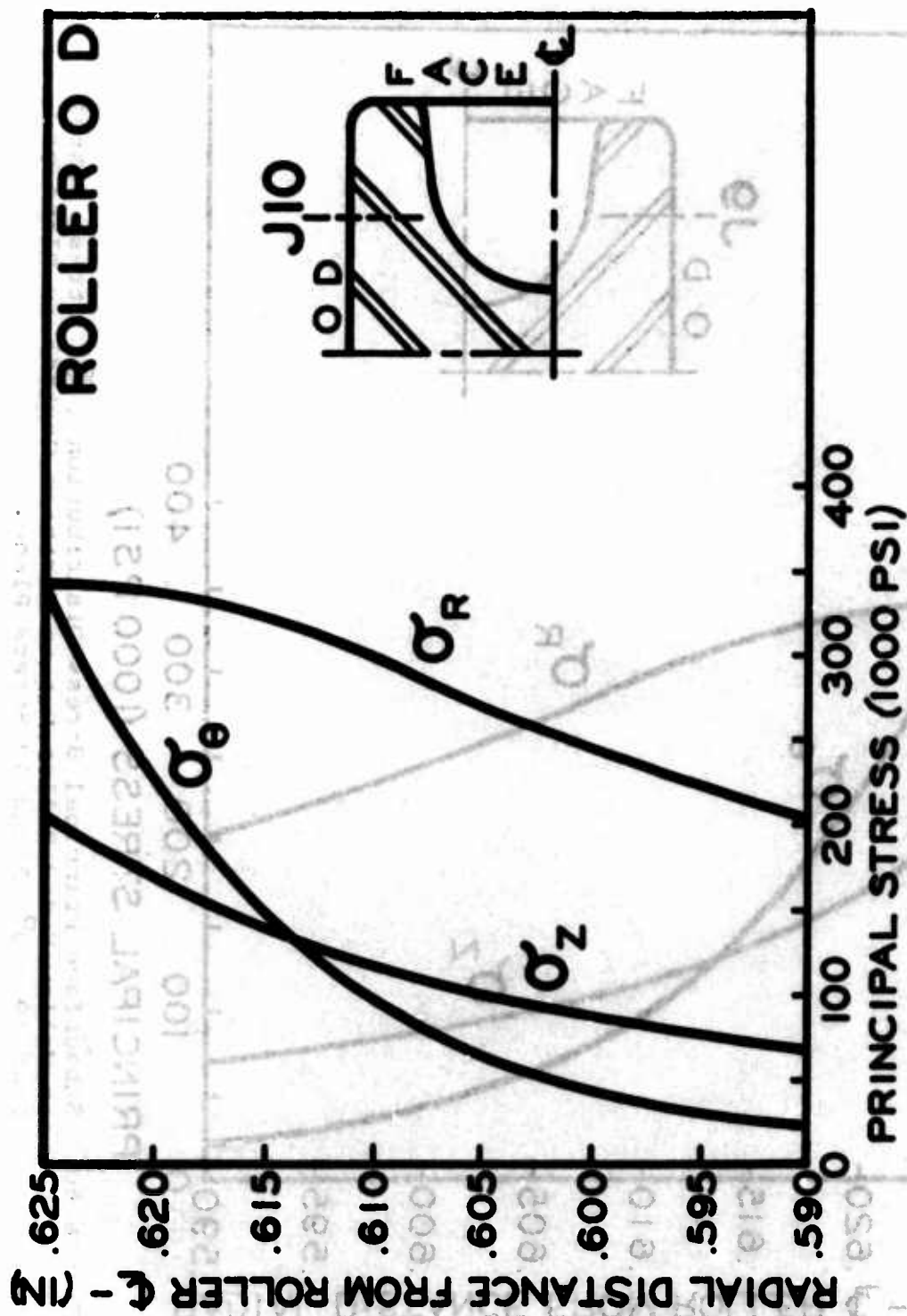


Figure 61. Subsurface Principal Stress Distribution (σ_g Stress State) in Hollow-Ended Roller Due to Hertzian Contact in Plane of Load ($\theta = 0^\circ$) Along J10 Stress Plane.

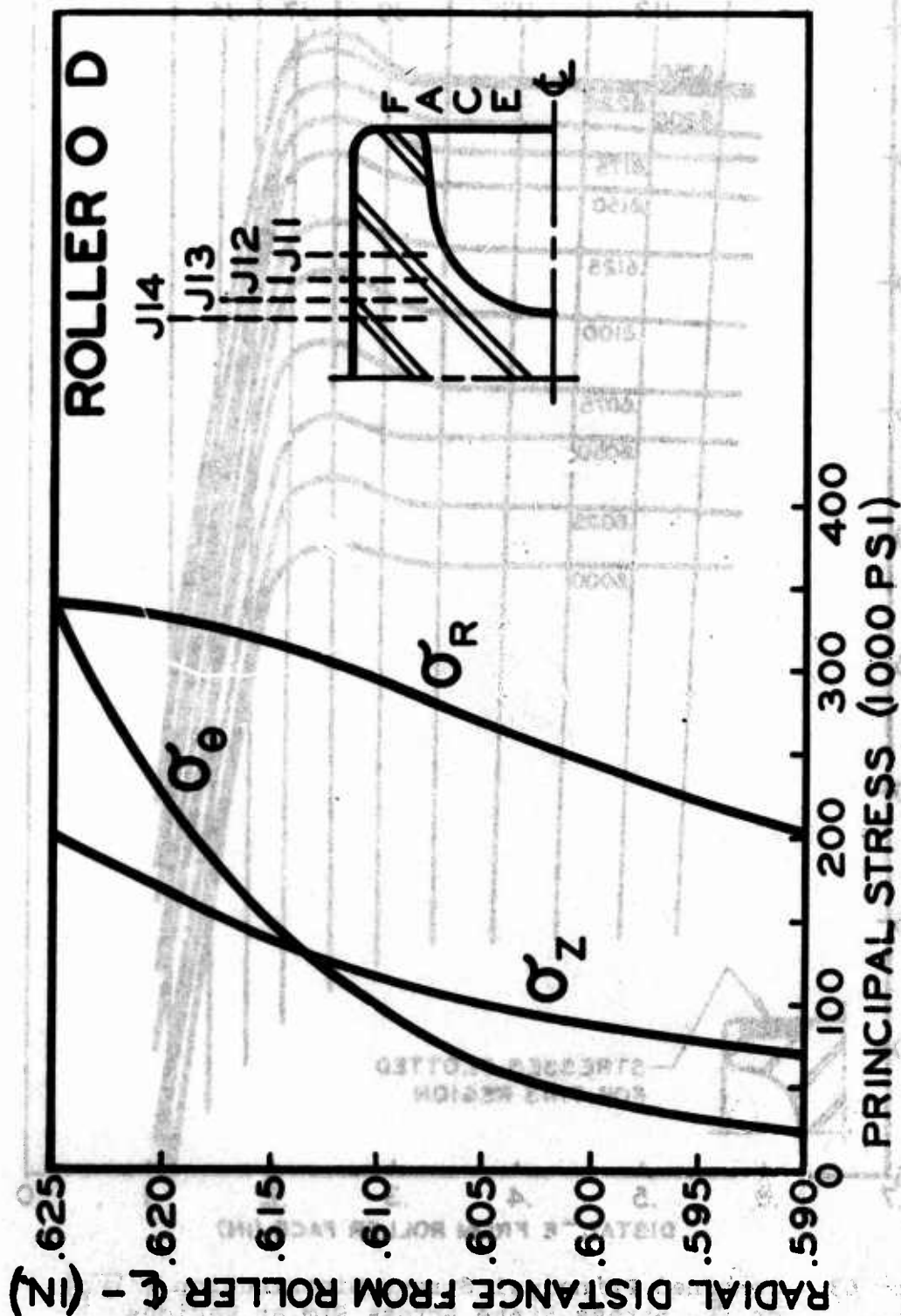


Figure 62. Subsurface Principal Stress Distribution (σ_s Stress State) in Hollow-Ended Roller Due to Hertzian Contact in Plane of Load ($\theta = 0^\circ$) Along J11-J14 Stress Planes.

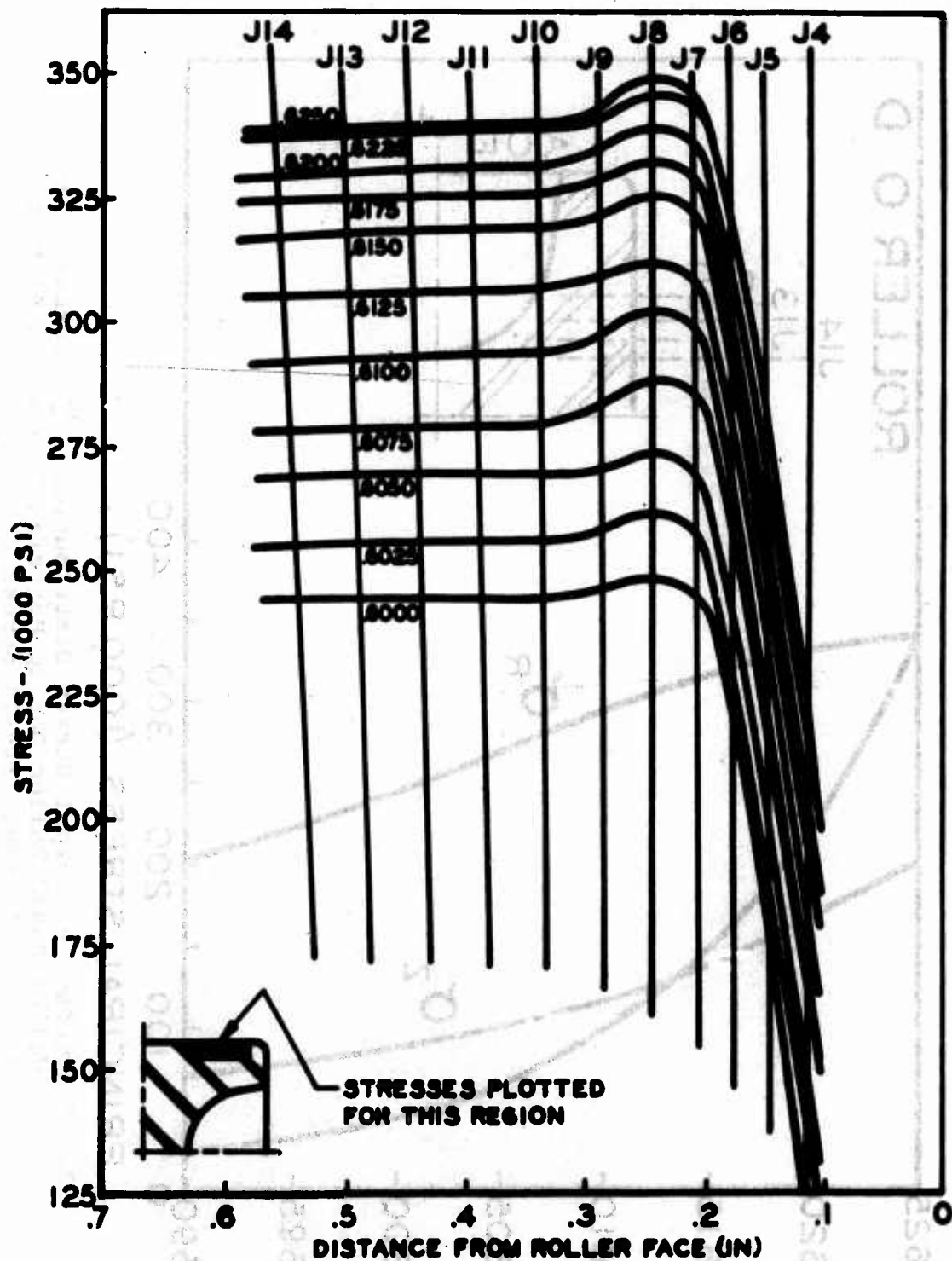


Figure 63. Combined Principal Stress Distribution (σ_R) or σ_H Stress State Across Rim at Various Radii in Plane of Load ($\theta = 0^\circ$).

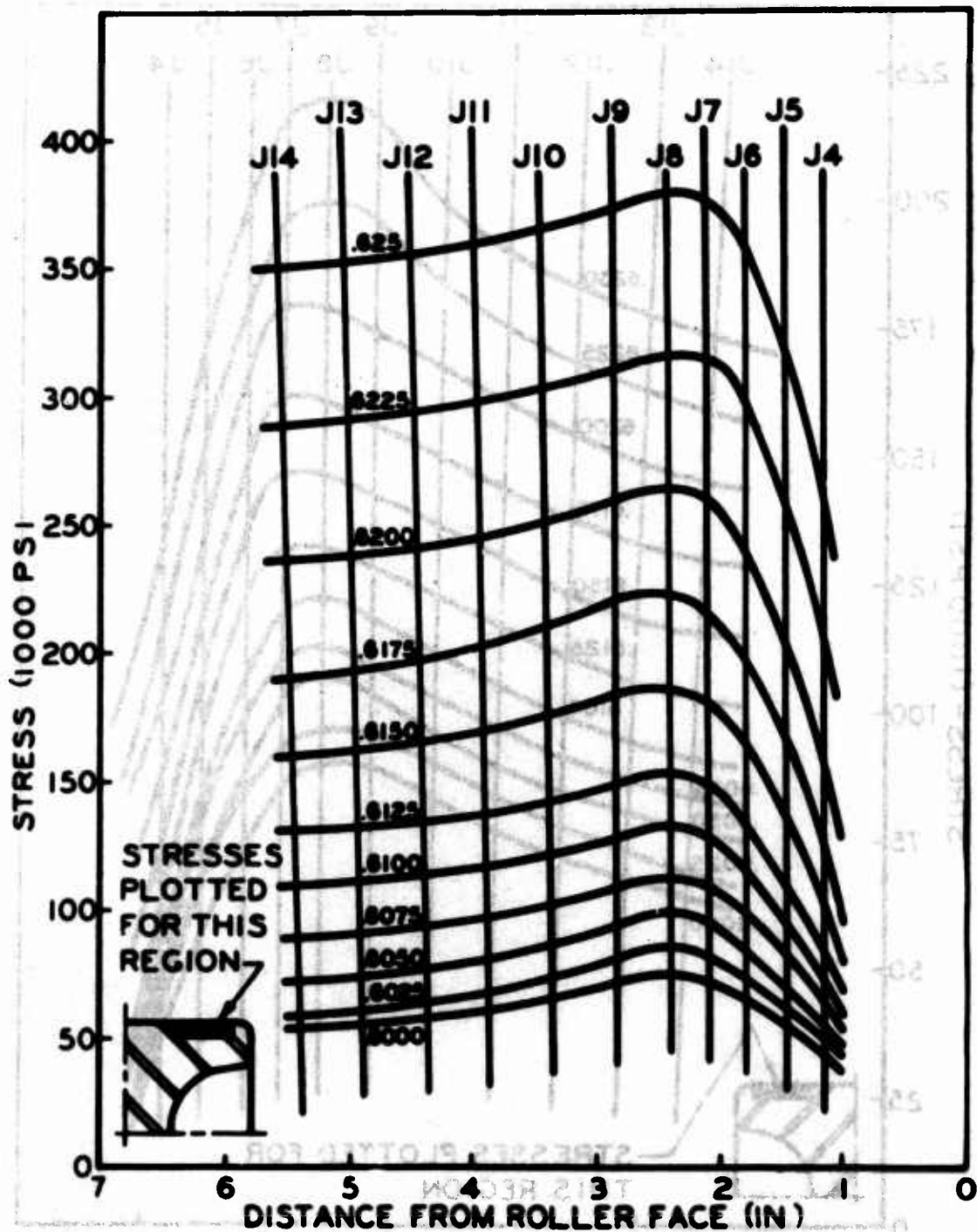


Figure 64. Combined Principal Stress Distribution (σ_{θ}) of σ_H Stress State Across Rim at Various Radii in Plane of Load ($\theta = 0^\circ$).

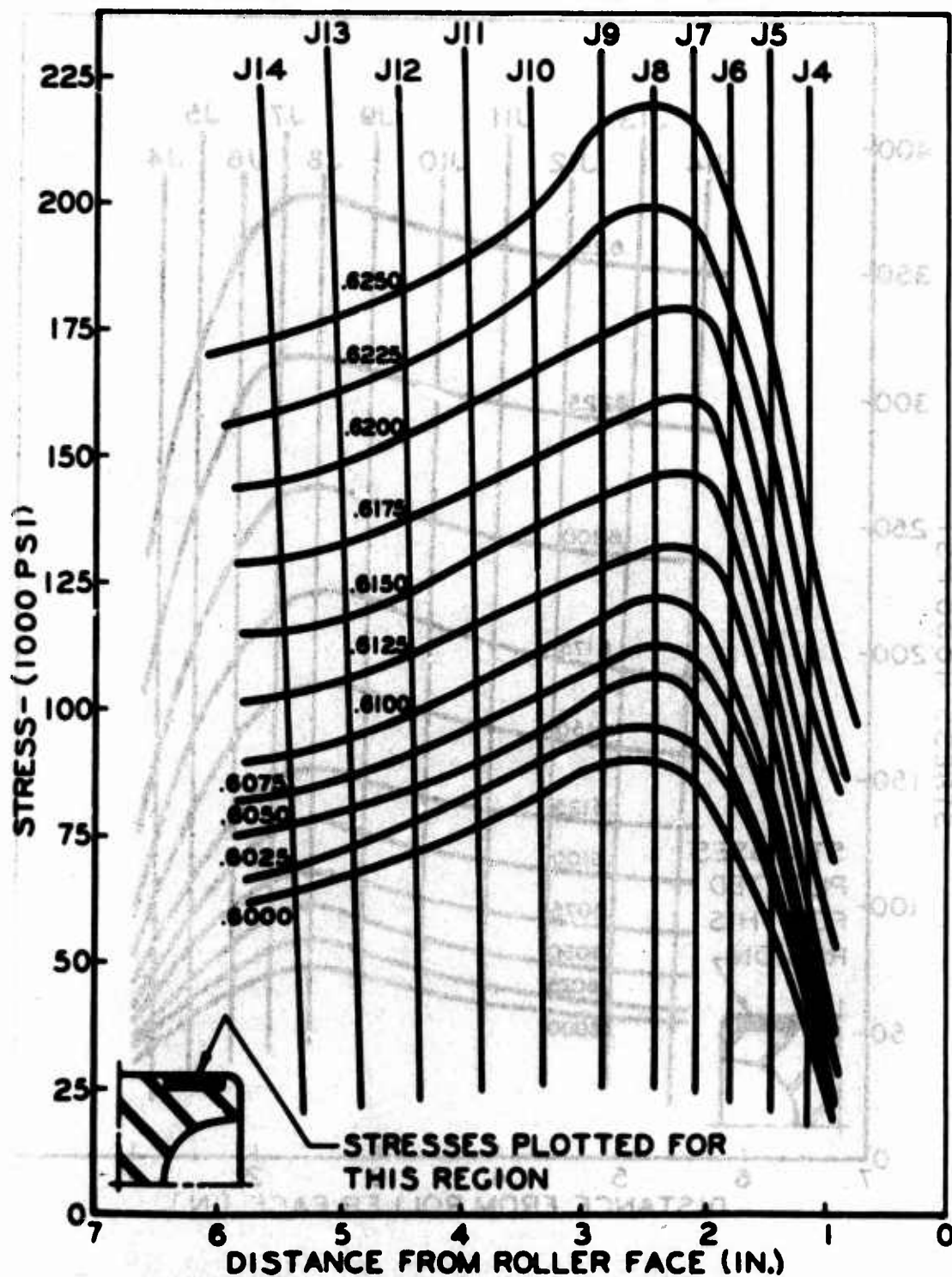


Figure 65. Combined Principal Stress Distribution (σ_z) of σ_H Stress State Across Rim at Various Radii in Plane of Load.

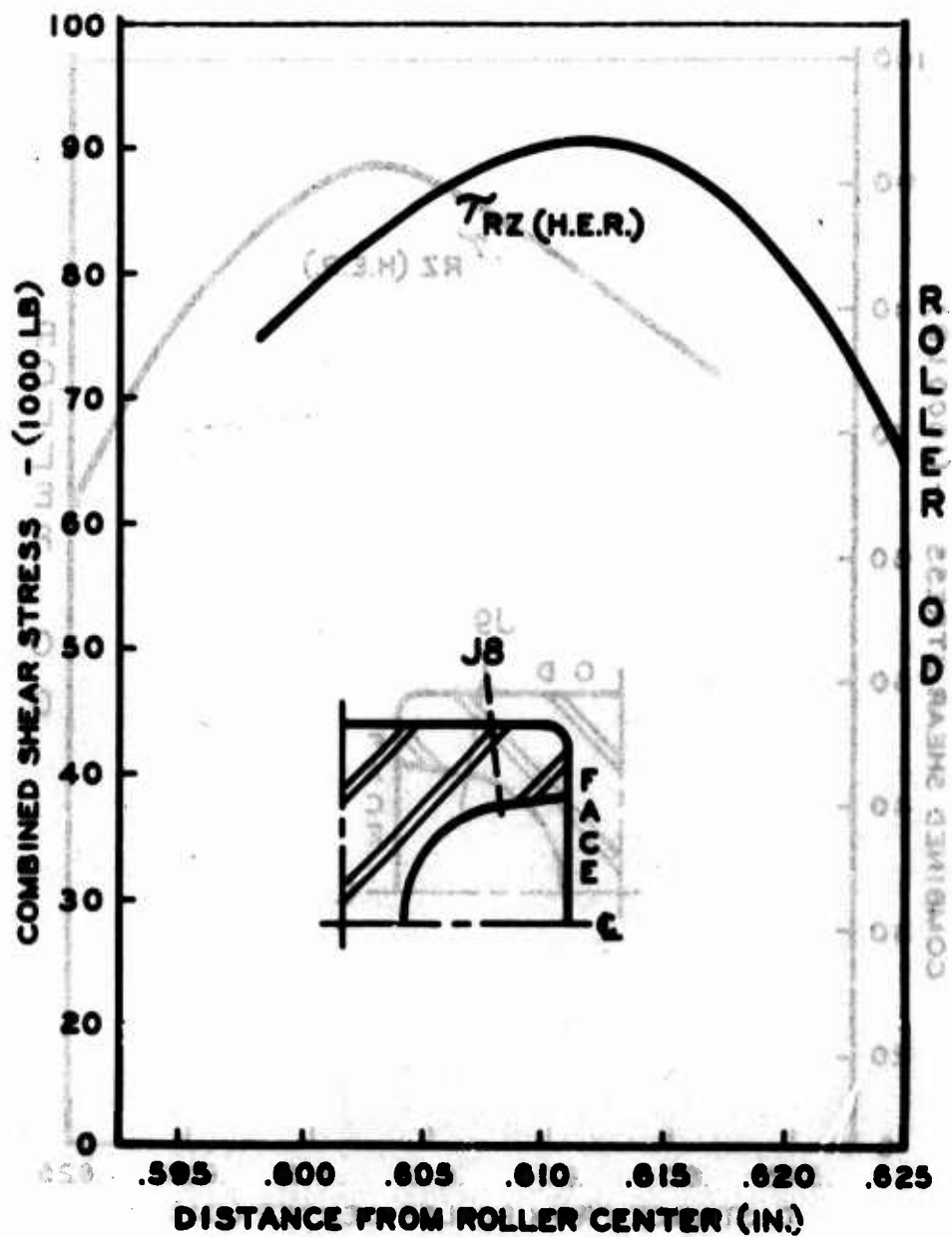


Figure 66. Significant Combined Shear Stress Distribution (σ_H Stress State) in Hollow-Ended Roller Along J8 Stress Plane in Plane of Load.

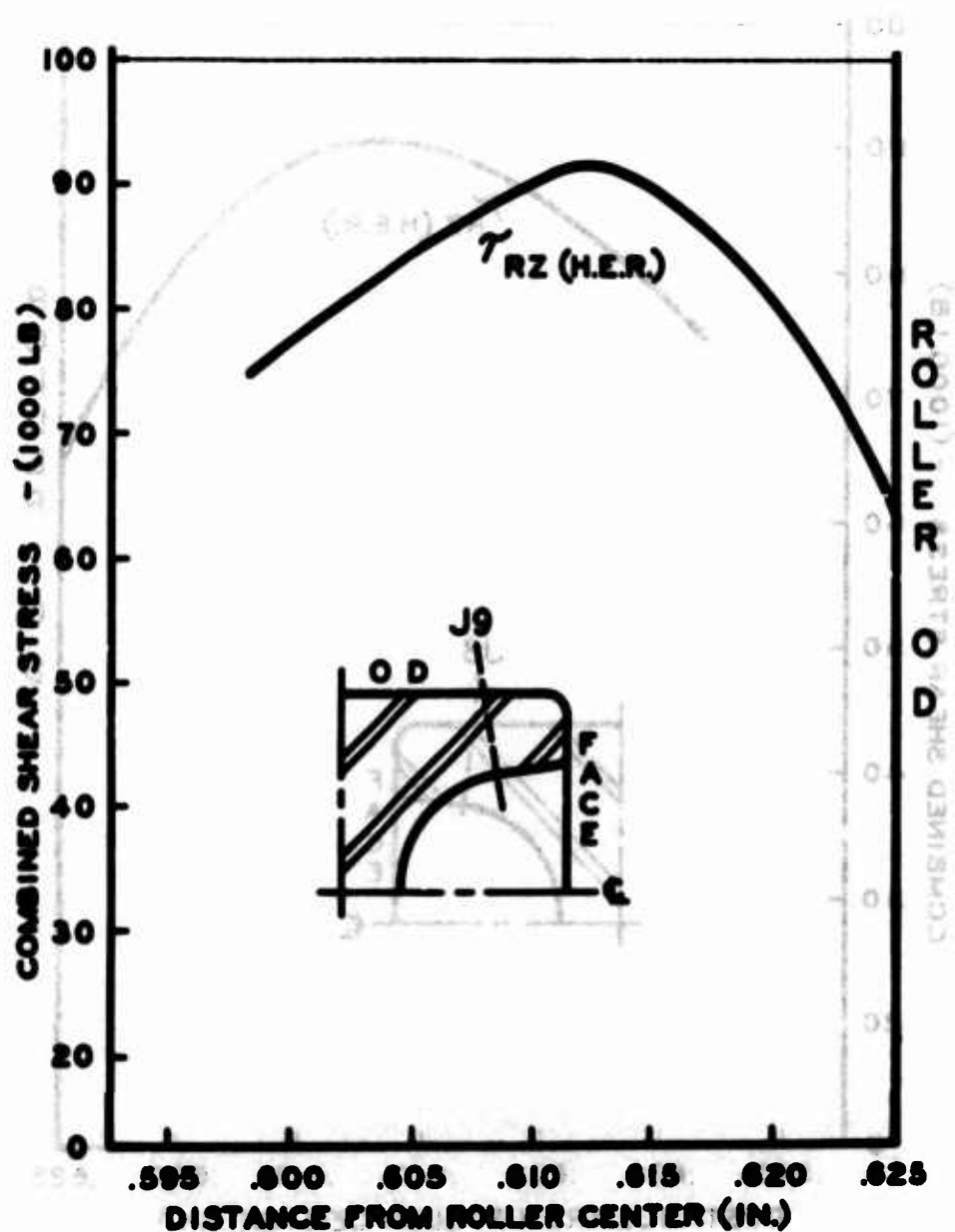


Figure 67. Significant Combined Shear Stress Distribution (τ_H Stress State) in Hollow-Ended Roller Along J9 Stress Plane in Plane of Load.

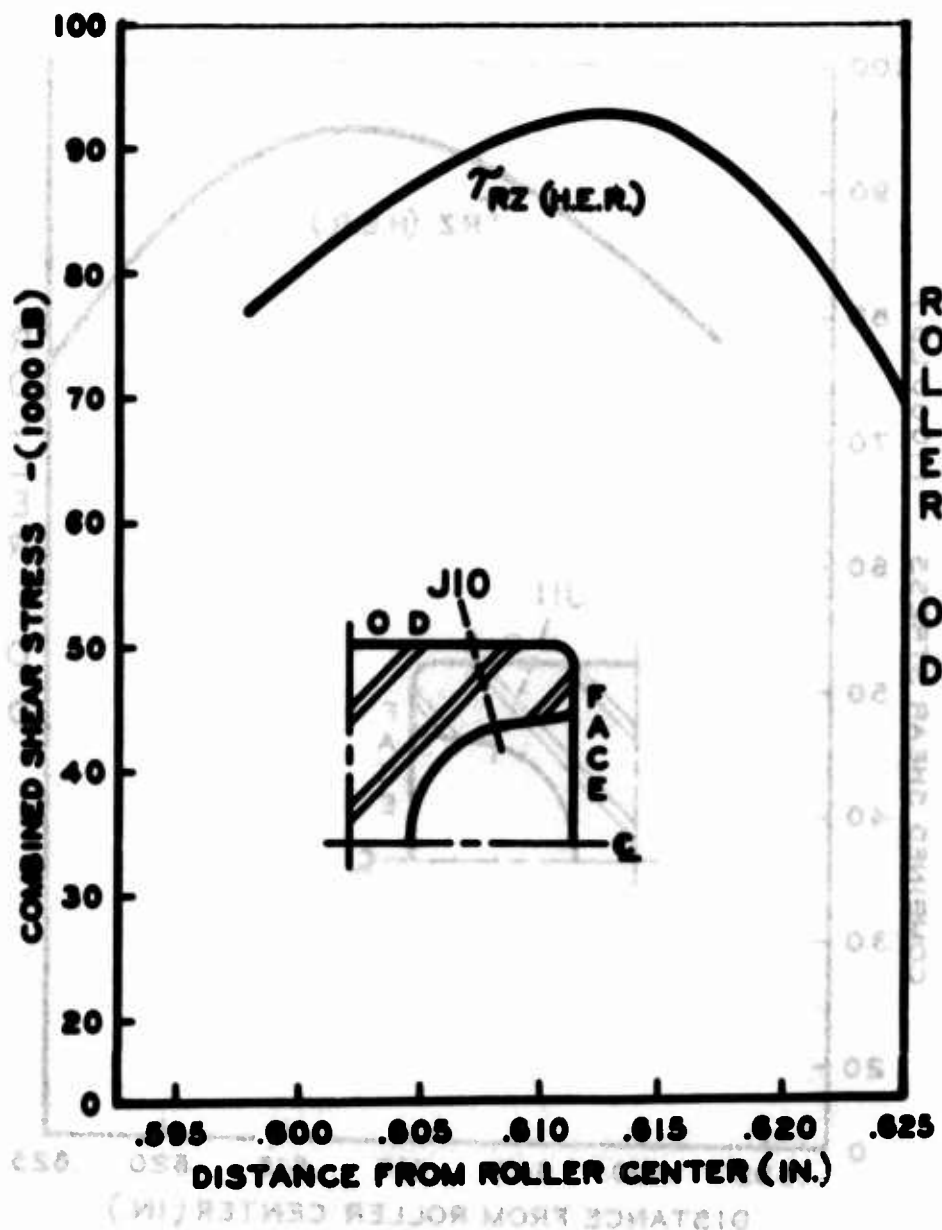


Figure 68. Significant Combined Shear Stress Distribution (σ_H Stress State) in Hollow-Ended Roller Along J10 Stress Plane in Plane of Load.

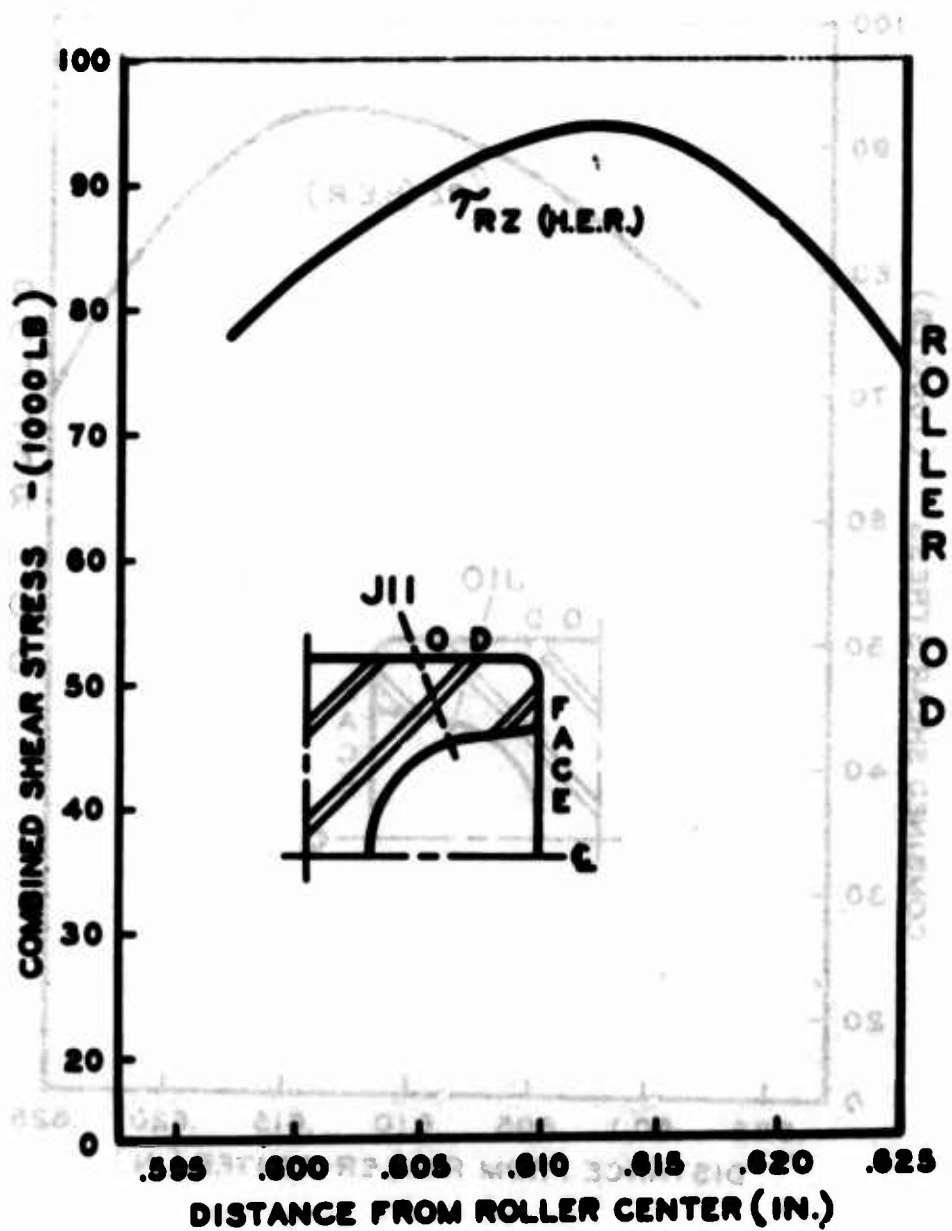


Figure 69. Significant Combined Shear Stress Distribution (σ_H Stress State) in Hollow-Ended Roller Along JII Stress Plane in Plane of Load.

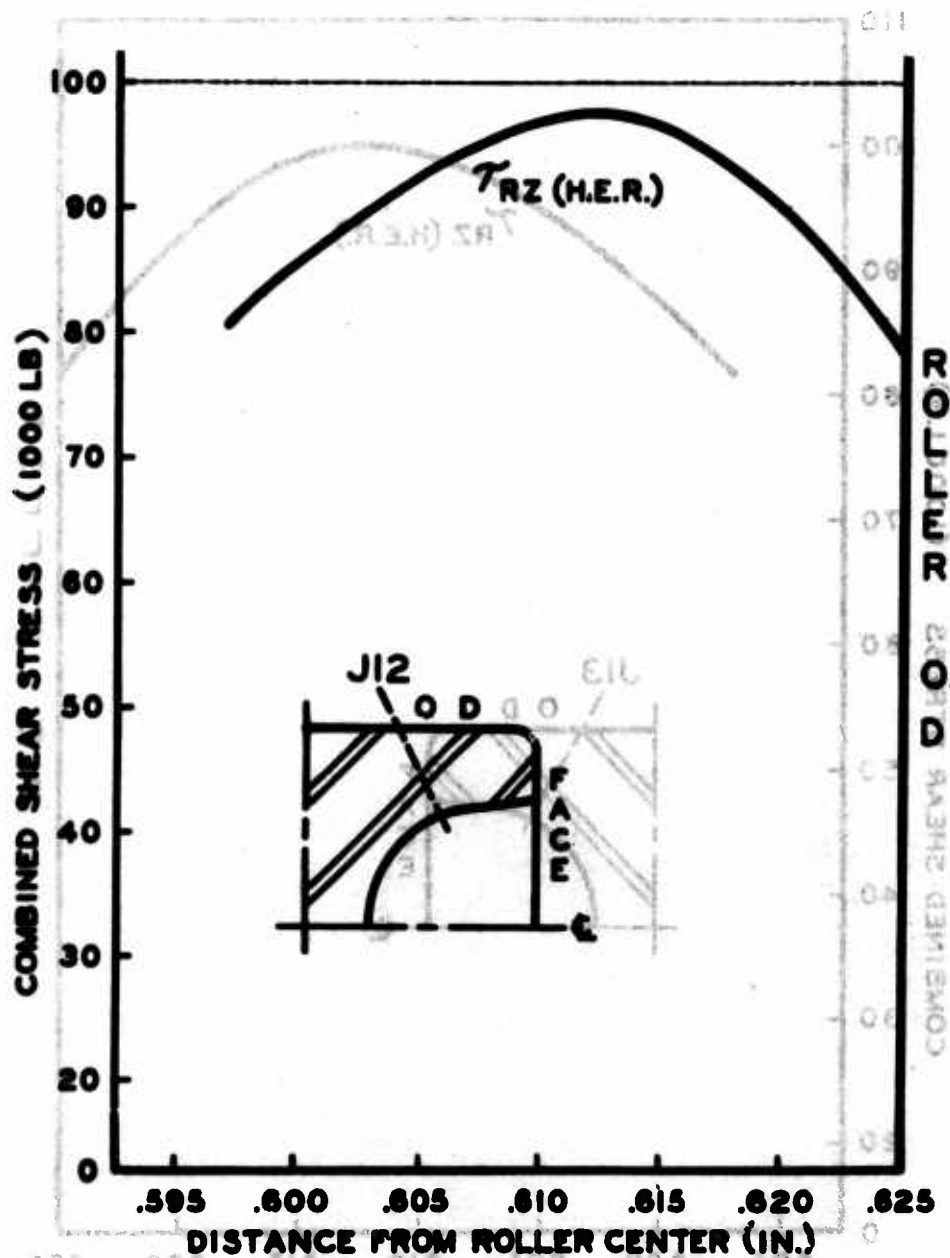


Figure 70. Significant Combined Shear Stress Distribution (σ_H Stress State) in Hollow-Ended Roller Along J12 Stress Plane in Plane of Load.

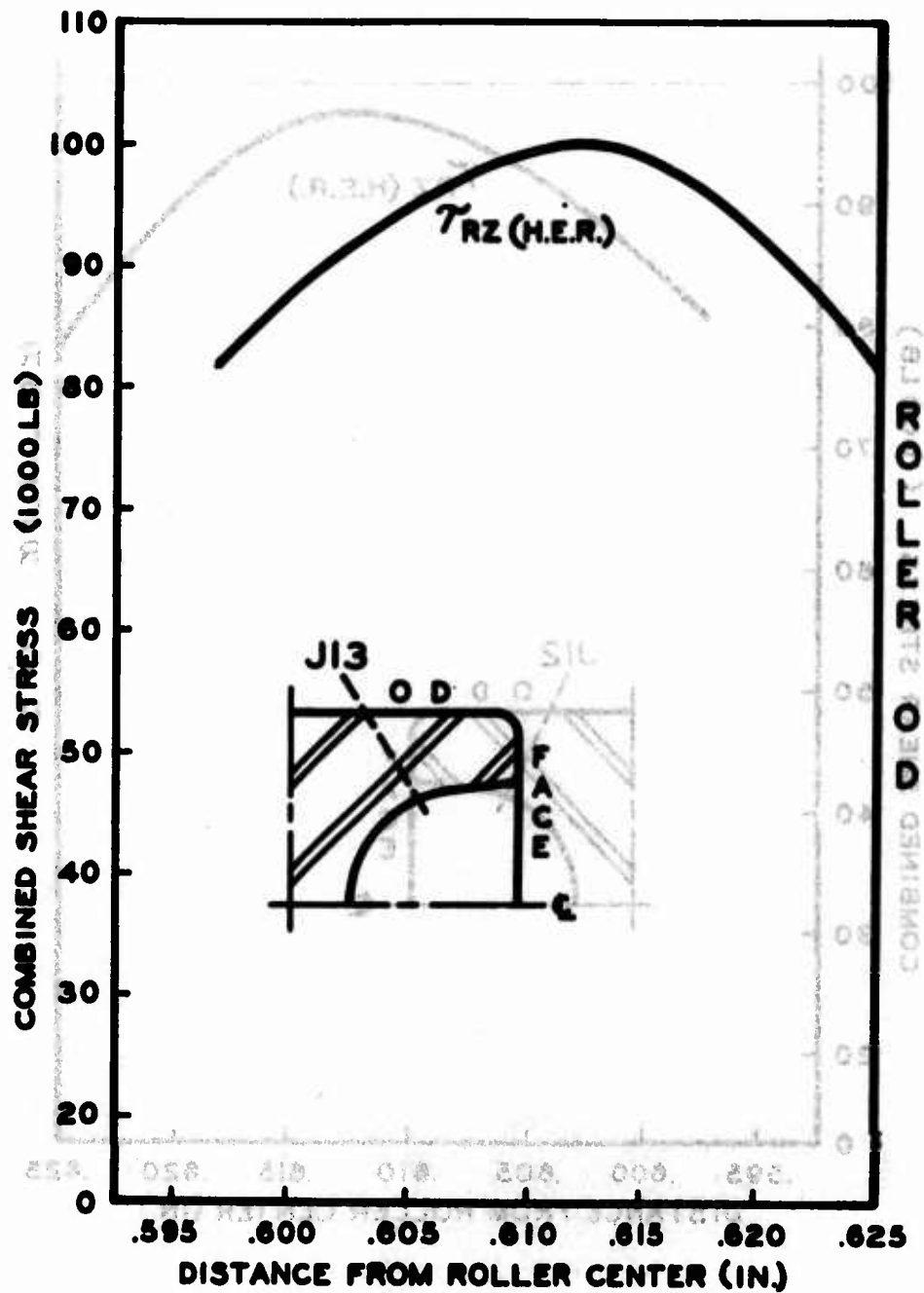


Figure 71. Significant Combined Shear Stress Distribution (σ_H Stress State) in Hollow-Ended Roller Along J13 Stress Plane in Plane of Load.

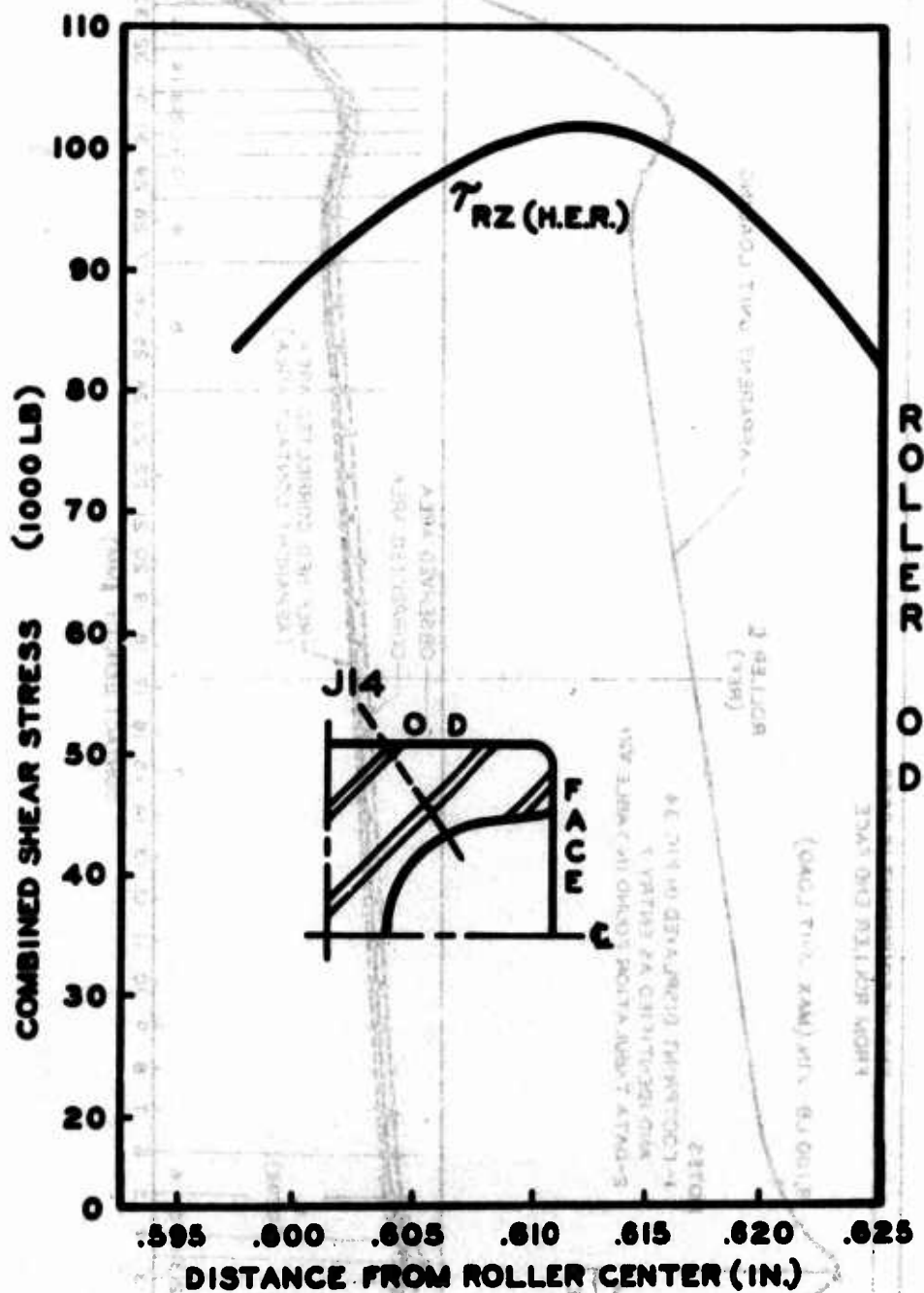


Figure 72. Significant Combined Shear Stress Distributions (σ_H Stress State) in Hollow-Ended Roller Along J14 Stress Plane in Plane of Load.

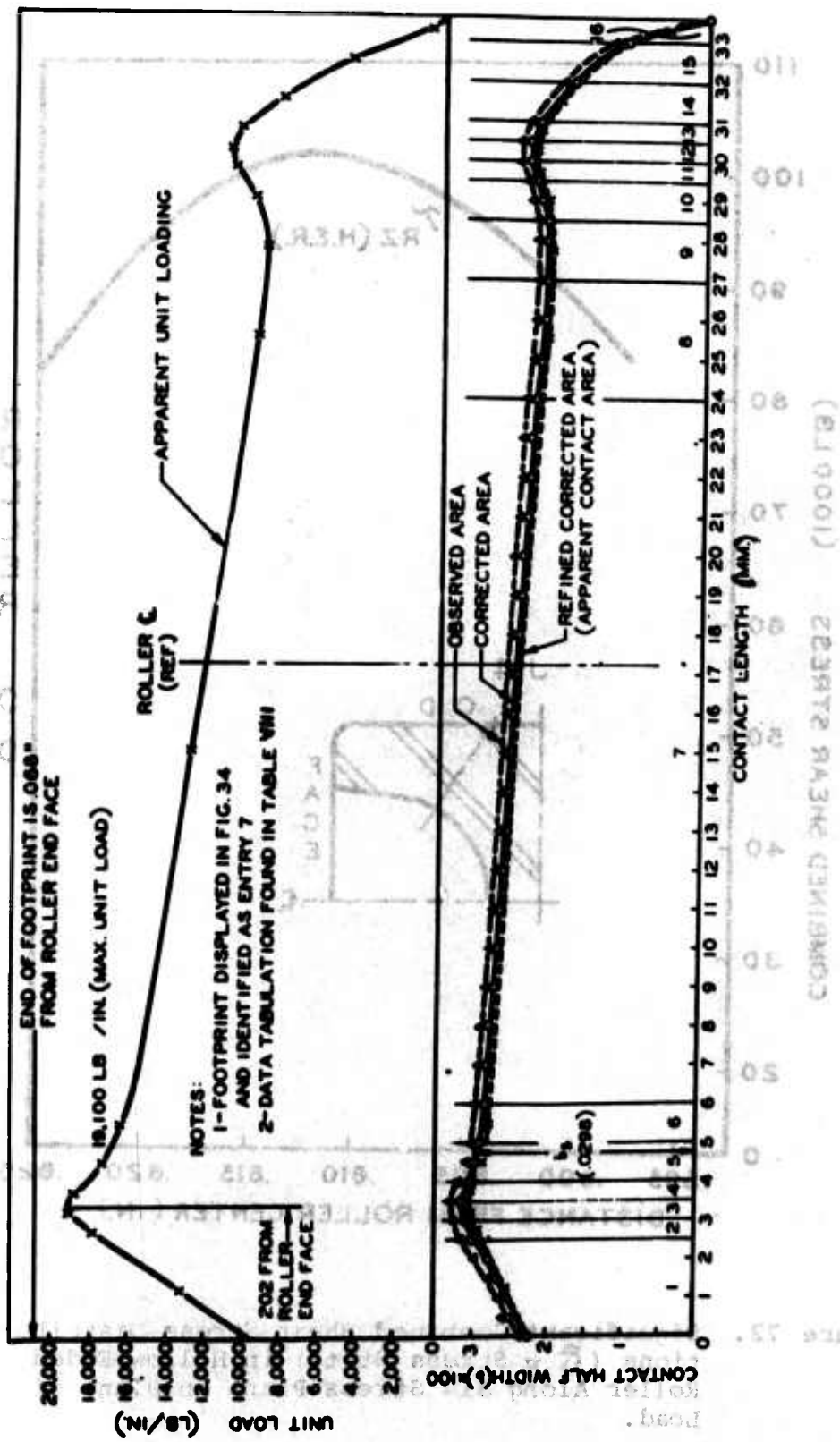


Figure 73. Respective Graphical Layout and Resultant Load Analysis for the Most Heavily Loaded Solid Roller Footprint (Major) in the Tandem Footprint Set.

NOTES:

1 - FOOTPRINT DISPLAYED IN FIGURE 34 AND IDENTIFIED AS ENTRY 7.

2 - DATA TABULATION FOUND IN TABLE VII

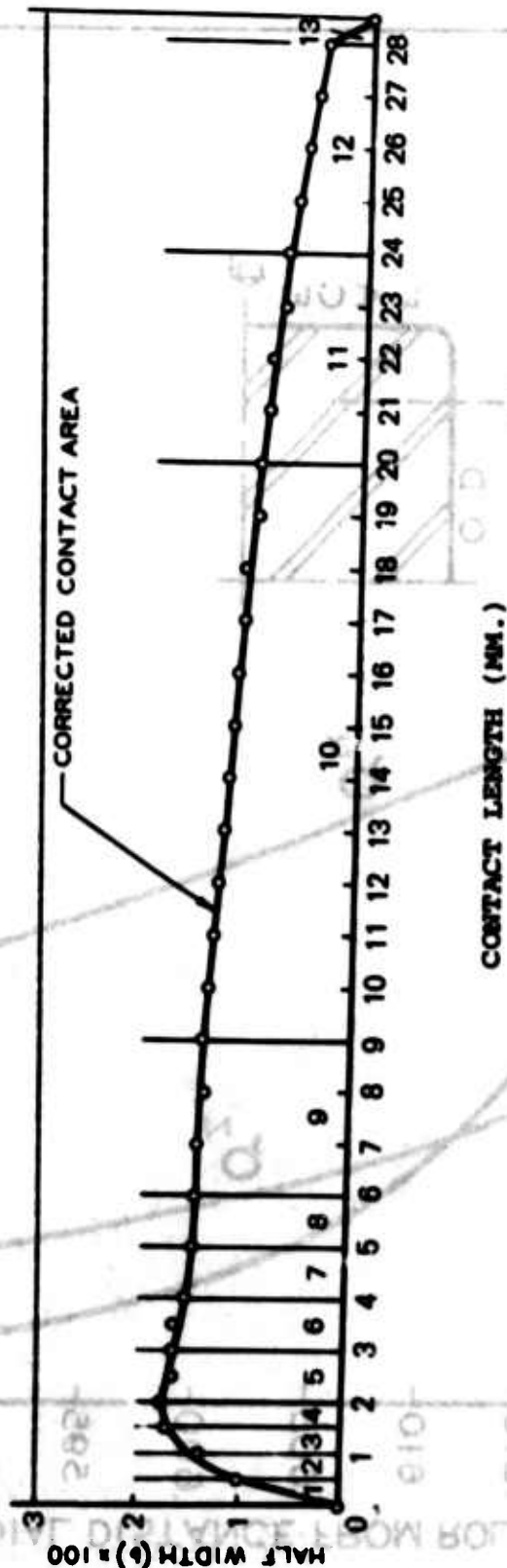


Figure 74. Respective Graphical Layout and Resultant Load Analysis for the Least Loaded Solid Roller Footprint (Minor) in the Tandem Roller Footprint Set.

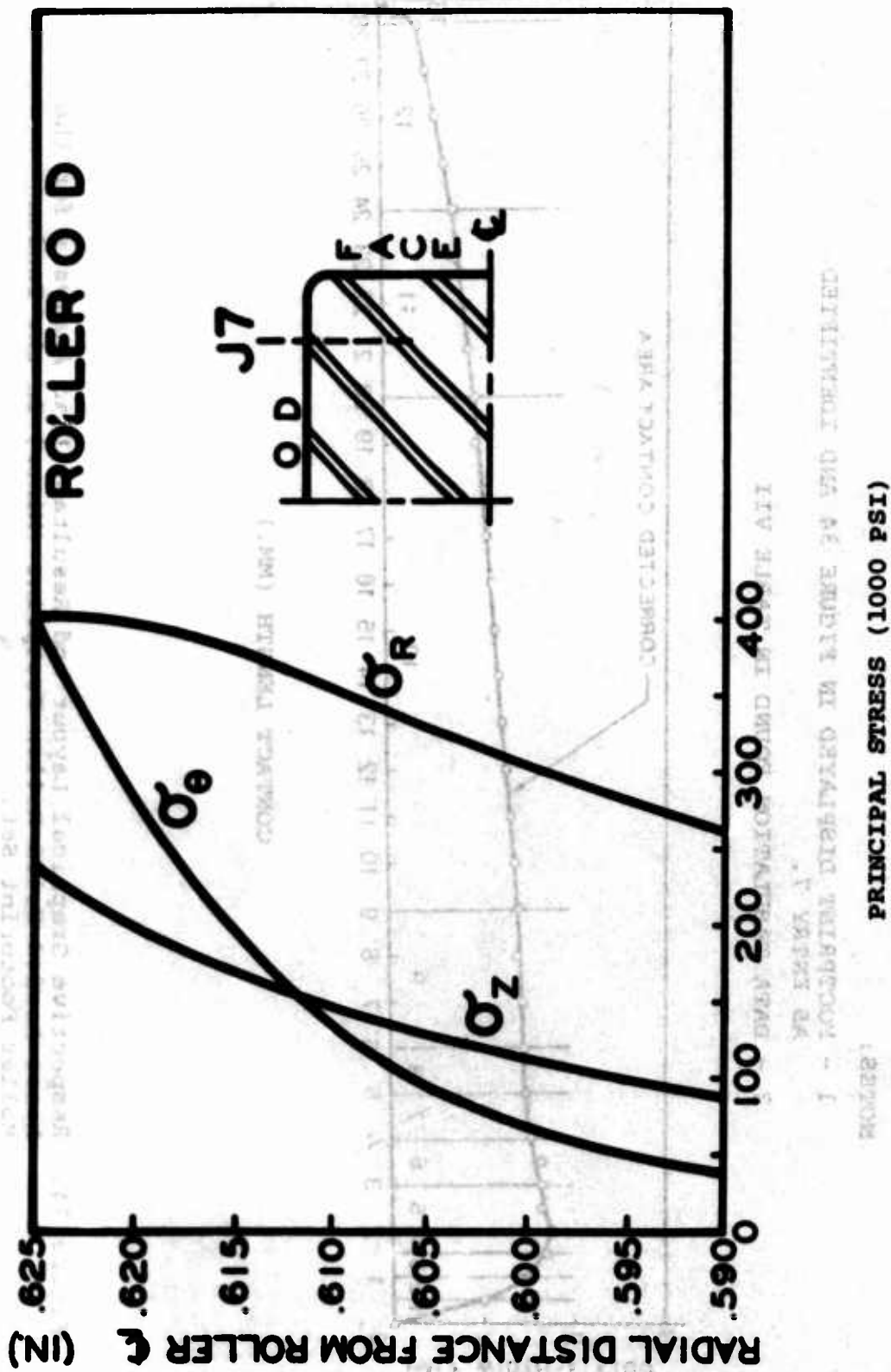


Figure 75. Hertzian Subsurface Principal Stress Distribution in Solid Roller Along J7 Stress Plane (Example) in Plane of Load.

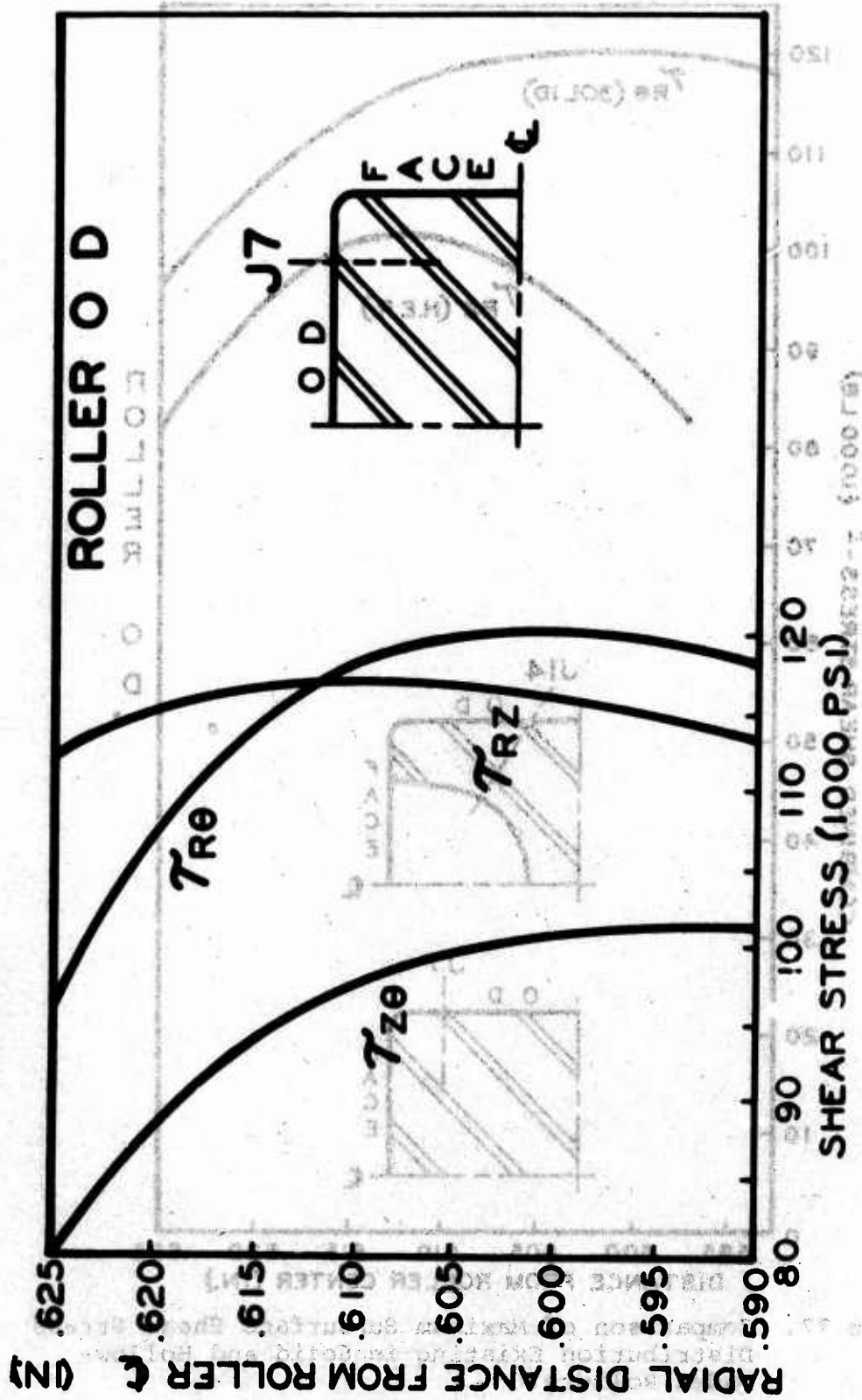


Figure 76. Hertzian Subsurface Shear Stress Distribution in Solid Roller Along J7 Stress Plane (Example) in Plane of Load.

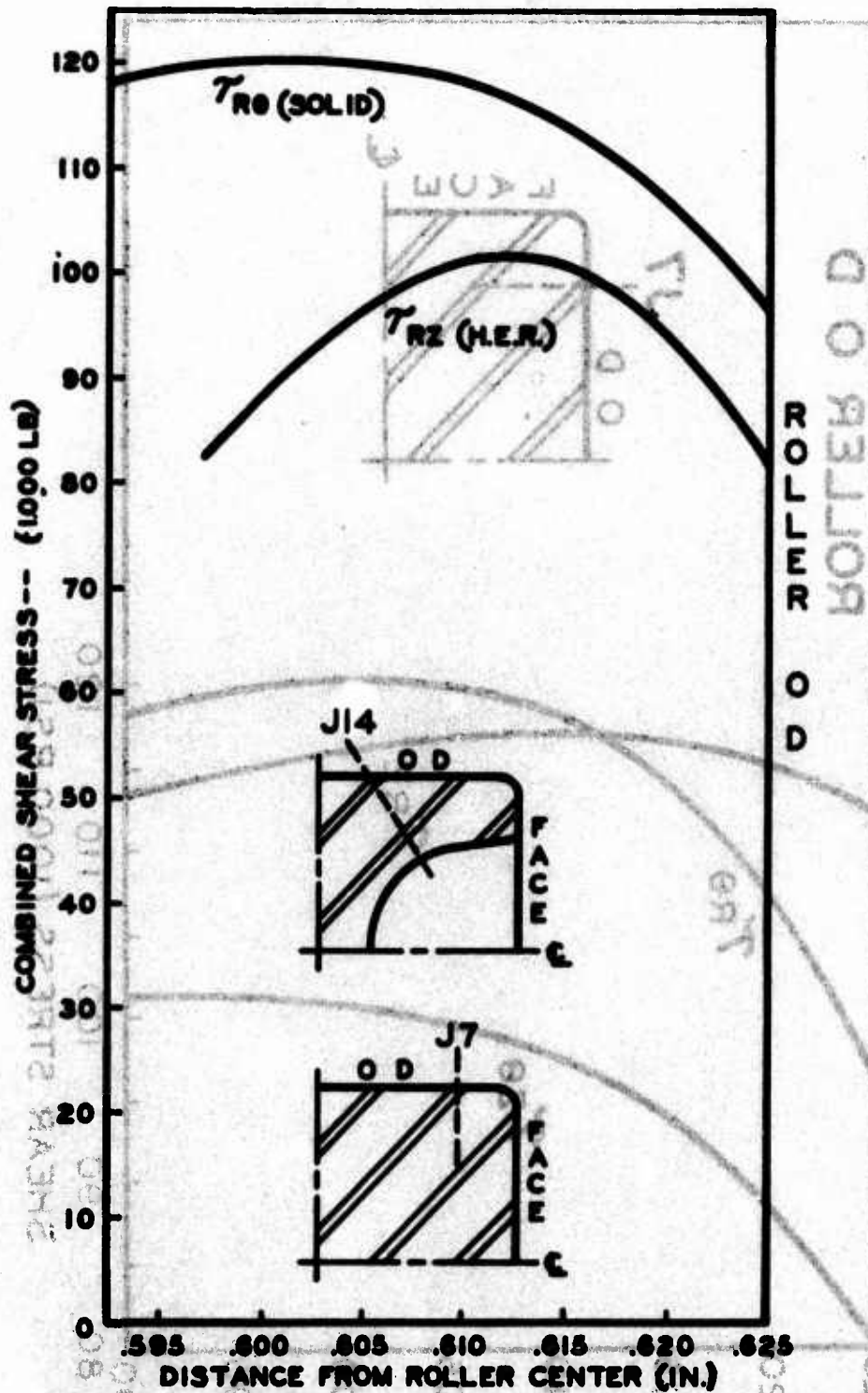


Figure 77. Comparison of Maximum Subsurface Shear Stress Distribution Existing in Solid and Hollow-Ended Rollers.

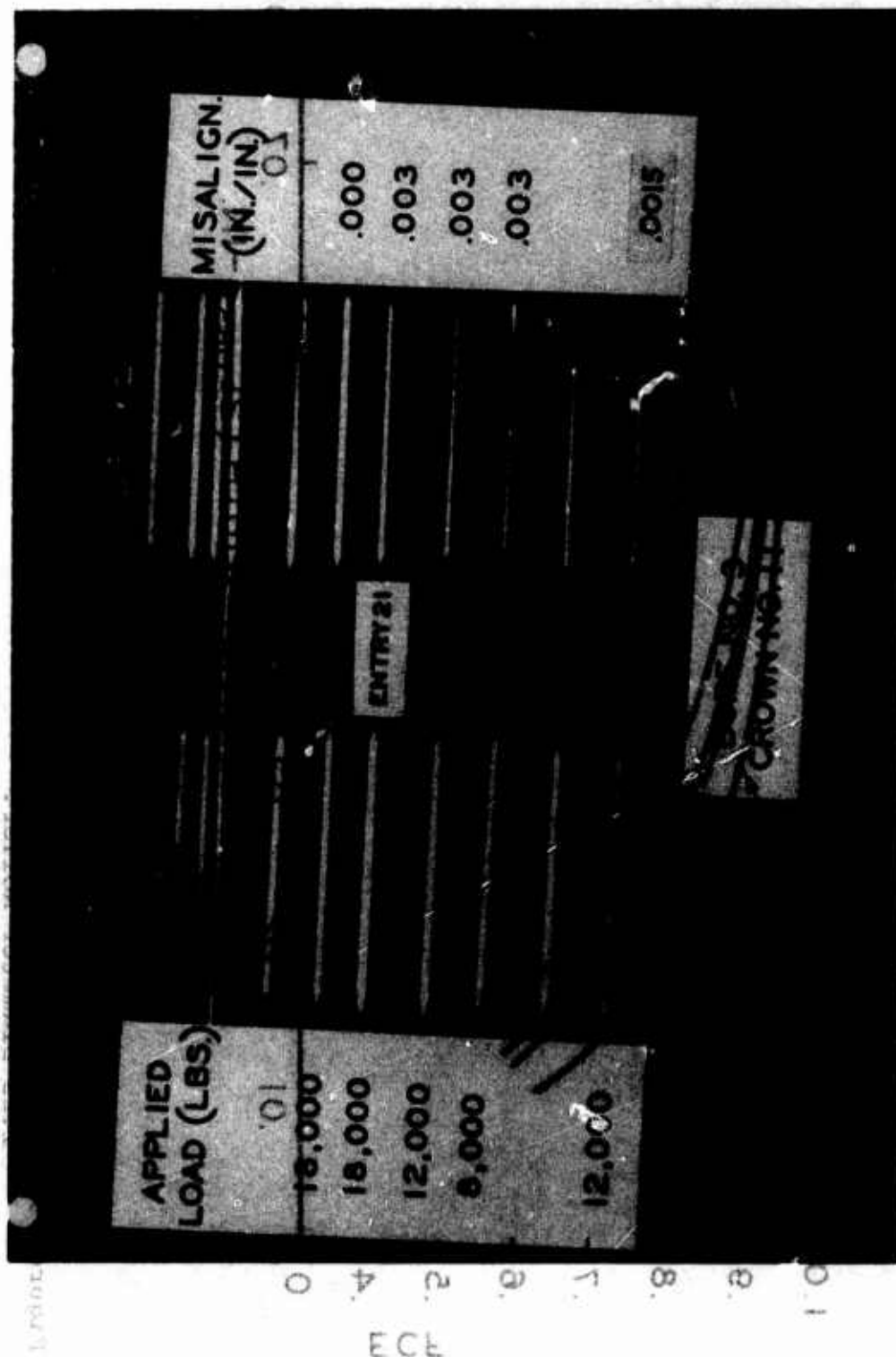


Figure 78. Footprint Shapes at Various Loads and Alignments
Confirming Final Hollow-Ended Roller Design.

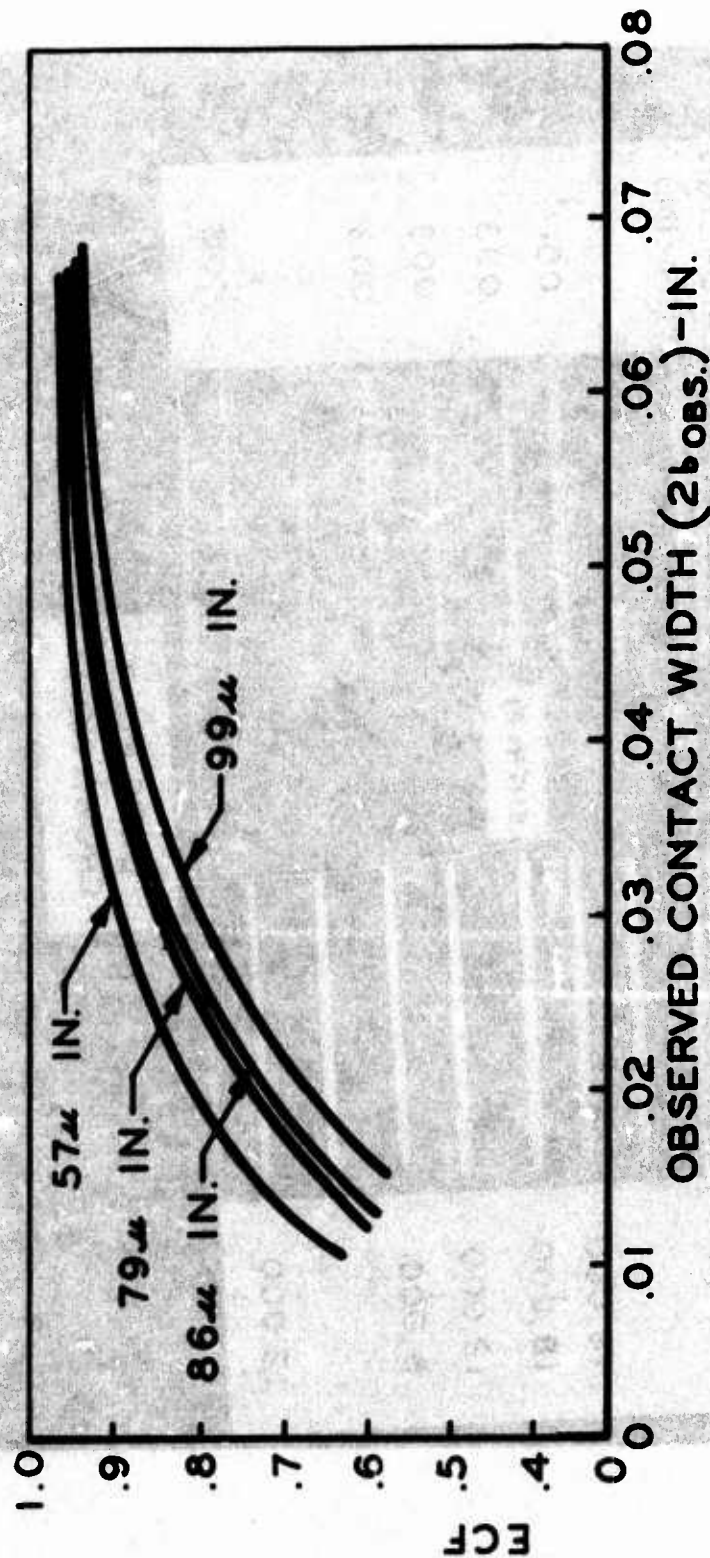


Figure 79. Etch Correction Factors for Various Film Thicknesses Using 1.25 Diameter Roller.

1. Bearing B-10 lives are based on cubic mean power of 7200 hp at 156 rotor rpm.
2. Bearing B-10 lives at .003 inch/inch misalignment were calculated based on test data of this report.

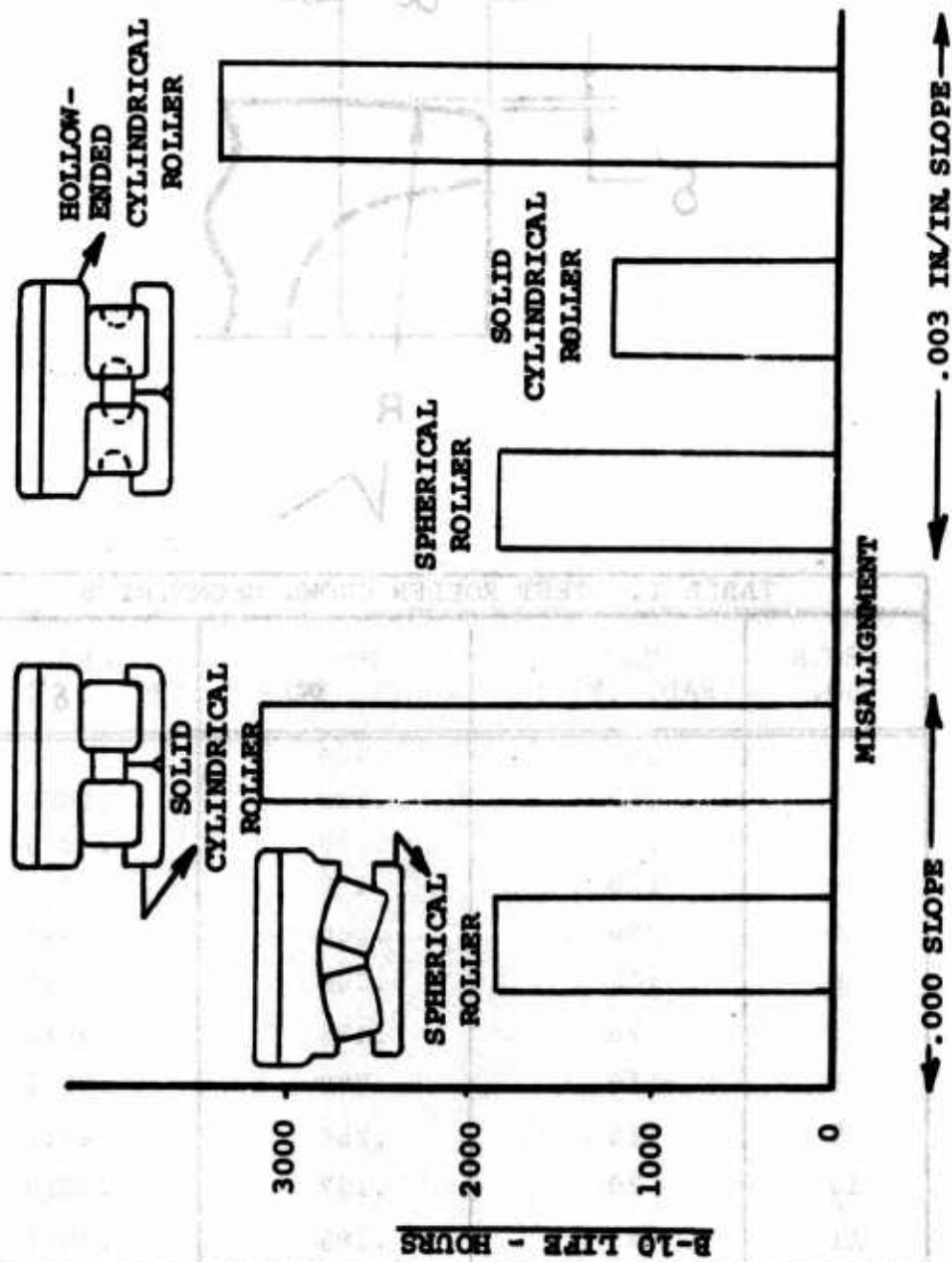


Figure 80. Life Comparison - HLH Planet Bearing Candidates.

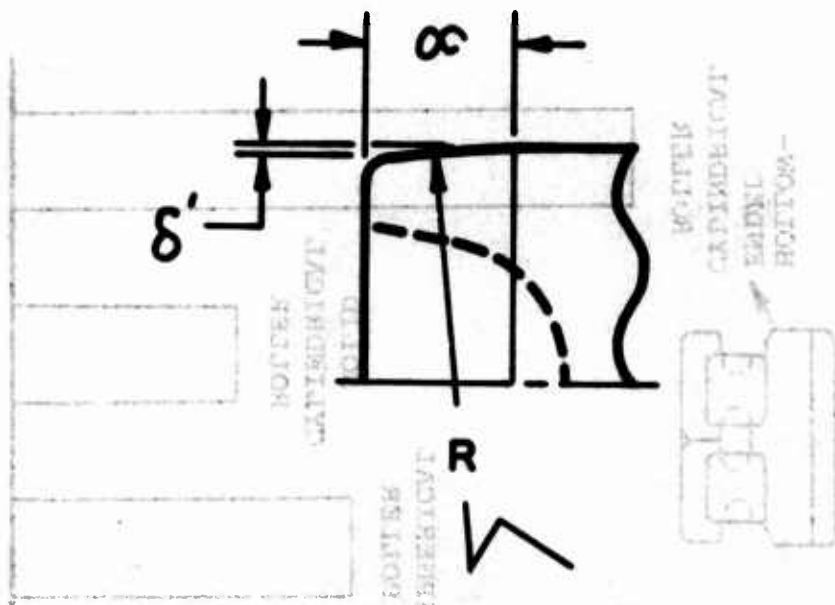


TABLE I. TEST ROLLER CROWN GEOMETRIES

CROWN NO.	CROWN RAD. (R) - IN.	CROWN LENGTH (L) - IN.	CROWN DROOP (δ') - IN.
1	200	.200	.0004
2	200	.280	.0006
3	150	.220	.0006
4	120	.170	.0006
5	260	.360	.0006
6	110	.204	.0008
7	70	.175	.0010
8	110	.740	.0021
9	110	.259	.0010
10	70	.197	.0010
11	53	.185	.0013

TABLE II. CHEMICAL COMPOSITION OF TEST PLATES AND ROLLERS		
PERCENT BY WEIGHT		
ELEMENT	8620 (ASTMA534)	CHROME #1 (ASTMA485)
CARBON	0.18 TO 0.23	0.90 TO 1.05
MANGANESE	0.70 TO 0.90	0.95 TO 1.25
SILICON	0.20 TO 0.35	0.45 TO 0.75
NICKEL	0.40 TO 0.70	0.25 MAX.
CHROMIUM	0.40 TO 0.60	0.90 TO 1.20
MOLYBDENUM	0.15 TO 0.25	0.06 MAX.
SULPHUR	0.025 MAX.	0.025 MAX.
PHOSPHOROUS	0.025 MAX.	0.025 MAX.
COPPER		0.35 MAX.

TABLE III. TEST ROLLER DATA

TYPE	ROLLER IDENTIFICATION	DRAWING No.	CROWN GROWTH No.	DROP (IN)	LENS-F (IN)	DIA. (IN)	CORNER BREAK (IN)	FINISH C D (IN IN.)	HARDNESS (RC)	FLAT LENGTH (IN)	CROWN LENGTH (IN)
SOLID	01X1A	2079-12500-	1	.0005	1.50	1.25	.072	2	63	.884	.308
SOLID	01X2A	15000-107-10	1	.0005	1.50	1.25	.066	2	63	.910	.295
SOLID	02X1A	2079-12500-	2	.0007	1.50	1.25	.067	2 1/2	63	.726	.387
SOLID	02X2A	15000-107-10	2	.0007	1.50	1.25	.072	2	63	.716	.392
SOLID	03X1A	2079-12500-	3	.0006	1.50	1.25	.067	2	62	.912	.294
SOLID	03X2A	15000-107-10	3	.0006	1.50	1.25	.071	1 1/2	62	.894	.303
SOLID	04X1A	2079-12500-	4	.0007	1.50	1.25	.070	1.5	63	1.058	.221
SOLID	04X2A	15000-107-10	4	.0007	1.50	1.25	.068	1.5	63	1.052	.224
SOLID	05X1A	2079-12500-	5	.0008	1.50	1.25	.068	2 1/2	63	.648	.426
SOLID	05X2A	15000-107-10	5	.0008	1.50	1.25	.078	3	63	.650	.425
SOLID	06X1A	2079-12500-	6	.0008	1.50	1.25	.067	1 1/2	63	.972	.264
SOLID	06X2A	15000-107-10	6	.0008	1.50	1.25	.067	1 1/2	62 1/2	.978	.261
SOLID	07X1A	2079-12500-	7	.0010	1.50	1.25	.067	2	62 1/2	1.002	.249
SOLID	07X2A	15000-107-10	7	.0010	1.50	1.25	.072	1 1/2	62	.994	.253
SOLID	08X1A	2079-12500-	8	.0020	1.50	1.25	.064	3	63	.322	.589
SOLID	08X2A	15000-107-10	8	.0020	1.50	1.25	.068	2	63	.334	.583
SOLID	09X1A	2079-12500-	9	.0011	1.50	1.25	.068	2	63	.822	.339
SOLID	09X2A	15000-107-10	9	.0011	1.50	1.25	.075	2	62 1/2	.822	.339
SOLID	010X1A	2079-12500-	10	.0011	1.50	1.25	.068	1 1/2	62	1.006	.247
SOLID	010X2A	15000-107-10	10	.0011	1.50	1.25	.064	1 1/2	62 1/2	1.018	.241
H.E.	011X1A	2579-12500-	10	.0011	1.50	1.25	.070-.040	1 1/2	61	.986	.257
H.E.	011X2A	15000-101-10	10	.0011	1.50	1.25	.074	2	61	.989	.255
H.E.	0210X1A	2579-12500-	10	.0011	1.50	1.25	.075	1 1/4	61	.984	.258
H.E.	0210X2A	15000-102-10	10	.0011	1.50	1.25	.076	1 1/4	62	.982	.259
H.E.	0310X1A	2579-12500-	10	.0011	1.50	1.25	.072	1 1/2	64	.979	.260
H.E.	0310X2A	15000-103-10	10	.0011	1.50	1.25	.072	1 1/2	64	.980	.260
H.E.	0410X1A	2579-12500-	10	.0011	1.50	1.25	.072	2	63	.984	.258
H.E.	0410X2A	15000-104-10	10	.0011	1.50	1.25	.074	1 1/2	64	.986	.257
H.E.	0510X1A	2579-12500-	10	.0011	1.50	1.25	.076	1 1/2	64	.982	.259
H.E.	0510X2A	15000-105-10	10	.0011	1.50	1.25	.073	1 1/2	64	.992	.254
H.E.	0610X1A	2579-12500-	10	.0011	1.50	1.25	.071	1 1/4	64	.990	.255
H.E.	0610X2A	15000-106-10	10	.0011	1.50	1.25	.070	1 1/2	64	.967	.266
H.E.	0311X1A	2579-12500-	11	.0013	1.50	1.25	.072	1 1/2	63	1.006	.247
H.E.	0311X2A	15000-103-10	11	.0013	1.50	1.25	.072	1 1/2	63	1.020	.240

TABLE IV. FOOTPRINT TEST DATA												
ENTRY NO.	FOOTPRINT NUMBER	PLATE NO.	ETCH THICKNESS (IN.)	25(MAX) ECF 25(MIN) (IN.)	NO CORR.	25(MAX) ECF 25(MIN) (IN.)	NO CORR.	25(MAX) ECF 25(MIN) (IN.)	NO CORR.	25(MAX) ECF 25(MIN) (IN.)	NO CORR.	PLATE THICKNESS (IN.)
1	0110X1A103	25	51-55	.059	.0566	.0205(.005)	.0165	1.32	18,000	.003	A,B	57
2	0210X1A103	25	51-59	.0605	.0581	.028(.073)	.0244	1.31	18,000	.003	B,C	57
3	0310X1A103	25	59-55	.0585	.0561	.024(.043)	.0202	1.31	18,000	.003	C,D	57
4	0410X1A103	25	55-56	.061	.0586	.030(.085)	.0265	1.32	18,000	.003	D,E	57
5	0510X1A103	25	56-59	.061	.0586	.035(.91)	.0318	1.30	18,000	.003	E,F	57
6	0610X1A103	25	59-45	.0605	.0581	.027(.067)	.0234	1.31	18,000	.003	F,G	57
7	010X1A103	25	45-73	.066	.0635	.047(.947)	.0445	1.33	18,000	.003	G,H	57
8	0110X1A103	26	71-106	.0615	.0572	.030(.80)	.024	1.31	18,000	.003	A,B	99
9	0110X1A103-1	26	106	.062	.0578	.032(.815)	.0261	1.30	18,000	.003	B,C	99
10	0210X1A103	26	90-106	.062	.0578	.032(.815)	.0261	1.30	18,000	.003	C,D	99
11	0310X1A103	26	90-91	.0602	.0559	.020(.67)	.0134	1.31	18,000	.003	D,E	99
12	0310X1A103-1	26	91-103	.061	.0567	.031(.805)	.0249	1.305	18,000	.003	E,F	99
13	0410X1A103	26	78-103	.0625	.0583	.037(.85)	.0314	1.30	18,000	.003	F,G	99
14	0510X1A103	26	78-111	.063	.0588	.038(.855)	.0324	1.295	18,000	.003	G,H	99
15	0510X1A103-1	26	111-116	.065	.0608	.038(.885)	.0324	1.305	18,000	.003	H,J	99
16	0610X1A103	26	112-116	.062	.0578	.032(.815)	.0261	1.31	18,000	.003	J,K	99
17	010X1A103	26	110-112	.068	.0639	.048(.90)	.0432	1.33	18,000	.003	K,L	99
18	0610X1A103	27	89-92	.061	.0573	.031(.84)	.0260	1.31	18,000	.003	A,B	86
19	0410X1A103	27	62-72-92	.063	.0593	.032(.85)	.0272	1.305	18,000	.003	B,C	86
20	0610X1A103	27	62-72-102	.064	.0603	.037(.88)	.0326	1.30	18,000	.003	C,D	86
21	0311X1A103	28	66-95	.058	.0551	0	0	1.31	18,000	.003	W,X,Y,Z	79

TABLE V. CRITICAL FOOTPRINT DIMENSIONS DATA AVERAGING (SEE TABLE IV FOR REFERENCE)								
ENTRY No.	FOOTPRINT No.	BORE No.	25(MAX)-IN. CORR.	25(END)-IN. CORR.	LENGTH IN.	25(MAX)-IN. AVERAGE	25(END)-IN. AVERAGE	LENGTH-IN AVERAGE
1	0110X1A183	1	.0566	.0165	1.32	.0572	.0222	1.31
8	0110X1A183		.0572	.0240	1.31			
9	0110X1A183-1		.0578	.0261	1.30			
2	0210X1A183	2	.0581	.0244	1.31	.0580	.0253	1.305
10	0210X1A183		.0578	.0261	1.30			
3	0310X1A183	3	.0561	.0202	1.31	.0562	.0195	1.308
11	0310X1A183		.0559	.0134	1.31			
12	0310X1A183-1		.0567	.0249	1.305			
4	0410X1A183		.0586	.0265	1.320			
13	0410X1A183	4	.0583	.0314	1.300	.0587	.0284	1.308
19	0410X1A183		.0593	.0272	1.305			
5	0510X1A183	5	.0586	.0318	1.30	.0596	.0323	1.30
14	0510X1A183		.0588	.0324	1.295			
15	0510X1A183-1		.0608	.0324	1.305			
20	0510X1A183		.0603	.0326	1.30			
6	0610X1A183		.0581	.0234	1.31			
16	0610X1A183	6	.0578	.0261	1.31	.0577	.0252	1.31
18	0610X1A183		.0573	.0260	1.31			
7	010X1A183	SOLID	.0635	.0445	1.33	.0637	.0439	1.33
17	010X1A183		.0639	.0432	1.33			
21	0311X1A183		.055	ROUND	1.31			

TABLE VI. OBSERVED FOOTPRINT MEASUREMENT AND CORRECTIONS						
MICROSCOPE SCALE READING	LENGTH (MM)	2b (IN.)	ECF	2b (CORR.) (IN.)	b (IN.)	bx100 (IN.)
73.5	0	.0240	.845	.0203	.0102	1.02
74	.5	.0310	.890	.0276	.0138	1.38
74.5	1	.0380	.923	.0352	.0176	1.76
75	1.5	.0405	.930	.0377	.0189	1.89
75.5	2	.0465	.945	.0440	.0220	2.20
76	2.5	.0505	.953	.0482	.0241	2.41
76.5	3	.0540	.958	.0518	.0259	2.59
77	3.5	.0585	.960	.0561	.0281	2.81
77.5	4	.0585	.960	.0561	.0281	2.81
78	4.5	.0565	.960	.0543	.0272	2.72
78.5	5	.0565	.960	.0543	.0272	2.72
79	5.5	.0560	.960	.0538	.0269	2.69
79.5	6	.0560	.960	.0538	.0269	2.69
80	6.5	.0560	.960	.0538	.0269	2.69
81	7.5	.0550	.958	.0528	.0264	2.64
82	8.5	.0560	.960	.0538	.0269	2.69
83	9.5	.0565	.960	.0543	.0272	2.72
84	10.5	.0560	.960	.0538	.0269	2.69
85	11.5	.0560	.960	.0538	.0269	2.69
86	12.5	.0560	.960	.0538	.0269	2.69
87	13.5	.0555	.960	.0533	.0267	2.67
88	14.5	.0560	.960	.0538	.0269	2.69
89	15.5	.0560	.960	.0538	.0269	2.69
90	16.5	.0555	.960	.0533	.0267	2.67
91	17.5	.0555	.960	.0533	.0267	2.67
92	18.5	.0550	.958	.0528	.0264	2.64
93	19.5	.0545	.957	.0522	.0261	2.61
94	20.5	.0530	.955	.0507	.0254	2.54
95	21.5	.0520	.955	.0498	.0249	2.49
96	22.5	.0525	.955	.0502	.0251	2.51
97	23.5	.0510	.953	.0487	.0244	2.44
98	24.5	.0500	.952	.0478	.0239	2.39
99	25.5	.0490	.950	.0466	.0233	2.33
100	26.5	.0480	.950	.0457	.0229	2.29
RELOCATED TEST PLATE/FOOTPRINT IN RESPECT TO MICROSCOPE STAGE						
93	27.5	.0475	.948	.0452	.0226	2.26
94	28.5	.0470	.947	.0446	.0223	2.23
95	29.5	.0470	.947	.0446	.0223	2.23
96	30.5	.0485	.950	.0462	.0231	2.31
96.5	31	.0430	.938	.0404	.0202	2.02
97	31.5	.0380	.923	.0352	.0176	1.76
98	32.5	.0220	.823	.0182	.0091	.91
98.5	33	0	0	0	0	0
NOTE: FOOTPRINT IS DISPLAYED IN FIGURE 34 - ENTRY 3						

TABLE VII. HOLLOW-ENDED ROLLER FOOTPRINT LOAD ANALYSIS

MAJOR FOOTPRINT									
SECTION NUMBER	INCREMENTAL HALF-WIDTH $(b_n) - IN.$	INCREMENTAL LENGTH (l_n) IN.	INCREMENTAL IN.	INCREMENTAL LB.	ADJUSTED INCREMENTAL LB. $(.925p_n)$	ADJUSTED INCREMENTAL LB.	ADJUSTED INCREMENTAL HALF-WIDTH $(b_n) - IN.$	ADJUSTED INCREMENTAL UNIT LOAD $(\frac{p_n}{l_n}) LB./IN.$	
1	.0136	.0394		146	136		.0131	3440	
2	.0195	.0394		307	286		.0188	7250	
3	.0240	.0394		465	433		.0231	11,000	
4	.0267	.0197		288	269		.0258	13,650	
5	.0279	.0197		315	294		.0270	14,950	
6	.0276	.0197		307	286		.0266	14,550	
7	.0270	.0197		294	274		.02605	13,900	
8	.0270	.0788		1176	1098		.02605	13,900	
9	.02695	.0394		586	546		.0260	13,850	
10	.0269	.0394		584	544		.0259	13,800	
11	.0269	.1576		2336	2180		.0259	13,830	
12	.02685	.0394		582	542		.0259	13,750	
13	.0268	.0394		580	540		.02585	13,720	
14	.0267	.0788		1148	1072		.02575	13,570	
15	.0265	.0394		566	527		.0255	13,400	
16	.0263	.0394		559	520		.0254	13,200	
17	.02425	.3546		4275	3980		.0234	11,230	
18	.0223	.0197		201	188		.0216	9550	
19	.0222	.0197		199	186		.0215	9440	
20	.02225	.0197		200	187		.0215	9500	
21	.0227	.0394		416	388		.0219	9850	
22	.02175	.0197		191	178		.0210	9030	
23	.0175	.0394		248	231		.0169	5850	
24	.0082	.0394		57	53		.0079	1345	
				$p_n = 16,026$		14,938			

TABLE VII - Continued						
MINOR FOOTPRINT						
SECTION NUMBER	INCREMENTAL EQUIVALENT HALF-WIDTH (b_n) - IN.	INCREMENTAL LENGTH (l_n) IN.	INCREMENTAL LOAD (P_n) LB.	ADJUSTED INCREMENTAL LOAD (P_n adj) LB. ($.925P_n$)	ADJUSTED INCREMENTAL HALF-WIDTH (b_n adj) - IN.	INCREMENTAL UNIT LOAD (P_n adj) ($\frac{P_n}{l_n}$) LB./IN.
1	.005	.0197	12	11		
2	.01275	.0197	65	61		
33	.01585	.0197	101	93		
4	.0172	.0197	170	112		
5	.0169	.0394	230	215		
6	.0158	.0394	202	189		
7	.0152	.0394	185	173		
8	.0149	.0394	178	166		
9	.0147	.1182	519	483		
10	.01225	.4334	1309	1220		
11	.009	.1576	268	250		
12	.006	.1576	132	123		
13	.0022	.0197	3	3		
		$P_n =$	3324	3099		
APPLIED LOAD VERIFICATION			19,350	18,037		
% DEVIATION			7.5%	0.206%		

TABLE VIII. SOLID ROLLER FOOTPRINT LOAD ANALYSIS

SECTION NUMBER	INCREMENTAL LENGTH (l_n) IN.		MAJOR FOOTPRINT INCREMENTAL LENGTH (l_n) LB.		ADJUSTED LOAD (P_n adj), (.945 P_n)		ADJUSTED INCREMENTAL LOAD (P_n adj), (b_n adj) -IN.		INCREMENTAL UNIT LOAD ($\frac{P_n}{l_n}$) LB./IN.
	INCREMENTAL LENGTH (l_n) -IN.	IN.	INCREMENTAL LENGTH (l_n)	LB.	INCREMENTAL LOAD (P_n)	ADJUSTED LOAD (.945 P_n)	INCREMENTAL LOAD (b_n adj) -IN.	ADJUSTED LOAD (b_n adj) -IN.	
1	.0261	.0985	1382		1310		.0255		13,250
2	.0303	.0197	371		352		.0295		17,900
3	.0314	.0197	397		376		.0305		19,100
4	.0311	.0197	390		370		.0303		18,800
5	.0298	.0394	719		682		.0290		17,300
6	.0290	.0394	680		645		.0282		16,400
7	.0257	.7092	9612		9112		.0250		12,900
8	.0221	.1182	1185		1123		.0215		9,500
9	.0215	.0591	561		532		.0210		9,000
10	.0223	.0394	402		381		.0217		9,670
11	.0234	.0197	222		210		.0228		10,670
12	.0237	.0197	227		215		.0231		10,930
13	.0231	.0197	216		205		.0225		10,400
14	.0205	.0394	340		322		.0200		8,180
15	.0153	.0394	188		178		.0149		4,520
16	.0055	.0236	17		16		.0054		680
		$P_n =$	16,909		16,029				

TABLE VIII - Continued

MINOR FOOTPRINT						
SECTION NUMBER	INCREMENTAL EQUIVALENT HALF-WIDTH (b _n) - IN.	INCREMENTAL LENGTH (l _n) IN.	INCREMENTAL LOAD (P _n) LB.	ADJUSTED INCREMENTAL LOAD (P _n adj) (.945 P _n)	ADJUSTED INCREMENTAL HALF-WIDTH (b _n adj) - IN.	INCREMENTAL UNIT LOAD ($\frac{P_n}{l_n}$) LB./IN.
1	.0075	.0394	49	46		
2	.0140	.0197	78	74		
3	.0158	.0197	101	96		
4	.0162	.0197	105	100		
5	.0153	.0197	94	89		
6	.0125	.03743	1178	1116		
7	.0080	.2758	385	365		
8	.0041	.1970	85	81		
9	.0012	.0394	2	2		
			P _n =	1969		
APPLIED LOAD VERIFICATION			18,986	17,998		
% DEVIATION			5.48%	0.00%		